DAMAGE DETECTION IN COMPOSITE STRUCTURES USING A DIELECTRIC SIGNATURE VARIATION APPROACH

DAMAGE DETECTION IN COMPOSITE STRUCTURES USING A DIELECTRIC SIGNATURE VARIATION APPROACH

By

AMR A. NASSR, B.Sc.

A Thesis

Submitted to the School of Graduate Studies

in Partial Fulfillment of the Requirements

for the Degree

Master of Applied Science

McMaster University

Master's of Applied Science (2008) McMaster University

(Civil Engineering) Hamilton, Ontario

TITLE: Damage detection in composite structures using a dielectric signature variation approach

AUTHOR: Amr A. Nassr, B.Sc. (Assiut University)

SUPERVISORS: Dr. Wael El-Dakhakhni

NUMBER OF PAGES: xv, 139

Abstract

Composite materials, constructed from a combination of fibre and resin, have rapidly emerged as a high performance alternative to conventional materials for new constructions as well as strengthening and repair of existing structures. However, the use of such materials may be accompanied by various types of damages and failure modes, including delamination, debonding, fibre rupture, and matrix cracking. This thesis presents a new nondestructive evaluation (NDE) technique for damage detection in composite structures. The concept, based on detecting local dielectric permittivity variations, was employed to design capacitance sensors with high sensitivity to detect such damages. An analytical and *2D* finite element models were used to assess the influence of the sensor geometrical parameters on the output signals and to optimize the sensor design. Concrete and wood specimens wrapped with glass-fibre composites containing pre-induced defects with different types and sizes were constructed and inspected. The sensors were also used to detect the delaminations and water intrusion defects in pultruded composite members. The principles behind the sensor operation were also applied to detect other damages in other structures; the capacitance sensors were designed and used to locate ungrouted cells in a concrete masonry wall. The proposed sensors, coupled with a commercially available portable capacitance meter, facilitate employing this technique in the field for rapid inspection of composite structures without the need for sophisticated data analyses that are usually required by other more expensive and time consuming NDE techniques.

Acknowledgements

I wish to express my deepest gratitude to my supervisor, Dr. Wael El-Dakhakhni for his encouragement and endless support throughout the research steps. This research would not have been successfully completed in this form without his advice and support. I appreciate the opportunity to work in such a professional environment. He gave me the opportunity to grow as a researcher and treated me more like a research partner rather than his student.

I am also indebted to Dr. Wael Ahmed for his valuable guidance and remarks.

This study forms a part of an ongoing research program in McMaster University, Centre for Effective Design of structures (CEDS), funded through the Ontario Research and Development Challenge (ORDC) Fund. This research falls under CEDS Focus Area III: Structural Rehabilitation and CEDC Focus Area IV: Enhanced Use of New and Under-Utilized materials. The author would like to gratefully acknowledge the assistance of Mr. Edward Fyfe and Ms. Sarah Witt, Fyfe Co. LLC, California, for providing the composite materials.

I gratefully acknowledge the financial support from McMaster University, The Centre for Effective Design of Structures, and the Department of Civil Engineering at McMaster University.

Finally, I want to express my love and deepest gratitude to my family. To them I dedicate this thesis.

Table of Contents

List of Figures

List of Tables

Chapter 1: Introduction

1.1 Background

Fibre-reinforced composites are constructed from two main materials, fibres and matrix. The fibre is typically glass, carbon, aramid, or polyethylene. The matrix is usually a thermoset polymer such as epoxy resin or polyimide. Composite materials offer many advantages over conventional construction materials including high strength, light weight and excellent corrosion resistance. Composites are being used increasingly in many engineering applications in a variety of components and systems for automotive and marine industries. The applications of composites in military and aerospace applications have been steadily increasing due to the low cost of composite materials and the development of related design and manufacturing technologies. Composite materials have been also used for new constructions, repair and rehabilitation of existing structures. Externally bonded composite laminates have been successfully applied to various structural members such as reinforced concrete (Kurtz et al. 2008), masonry (El-Dakhakhni et al. 2004), steel (Zhao and Zhang 2007), and timber (Dempsey and Scott 2006). Moreover, the use of composites as pultruded sections (Alampalli 2006), has been proved to be very successful in industrial and civil applications.

However, the mechanical properties of composite materials or pultruded sections may severely degrade in the presence of damages. Common damages of composite

materials are delamination, debonding, fibre rupture, and matrix cracking. Delamination, which is the separation between two adjacent laminates, appears to be the most common failure mode, usually caused by manufacturing imperfections, cracks in matrix materials, impacts by foreign objects or other harsh service environments. Delaminations substantially reduce the stiffness and load capacity of structural members and may influence the structure's overall performance.

The ability to detect such damages at an early stage is essential to ensure required safety levels, and to assess the structural integrity and long-term performance of composite structures. Various nondestructive evaluation (NDE) techniques have been studied to detect debonding, delamination, and other potential defects in composites. Currently available NDE techniques include methods based on ultrasonic signatures, radiography, eddy-current or thermal field variations.

Review of the available NDE methods indicated many difficulties associated with their field application due to their requirements for couplants, heat or wave sources, and sophisticated data analyzers. This is addition to limitations related to coverage area and effective detection depth along with the difficulties associated with interpretations of the results.

With the increasing use of composite materials in various engineering applications, it is a growing concern to develop a reliable and cost-effective NDE technique to monitor and assess related serviceability and safety level. In this regard, identifying the location and extent of defects/damages in composite components is key for continuously functioning composite system and sustainable related industries.

1.2 Research Objectives and Scope

The objective of this study is to develop a rapid cost-effective technique for the detection of defects that may occur in composite materials. The proposed technique is based on detecting the local dielectric permittivity variations in composite materials using specially designed Coplanar Capacitance Sensors (CCS) and Interdigital Capacitance Sensors (IDCS). CCS and IDCS have the benefit of the sensors' electrodes being in the same plane and, thus, can be applied to the composite material under test from one side, instead of having to sandwich the material between the electrodes. This technique utilizes the information from the measured capacitances to locate defects/damages in composite materials. The dependencies between damage parameters in composites and capacitance measurements will be determined theoretically and verified experimentally. The choice of the sensing system and the sensor optimization are key components for accurate and meaningful data. The theoretical background and the analytical models used in developing the proposed capacitance technique will be presented. A two dimensional (*2D*) Finite Element Modelling (FEM) technique to identify sensor design parameters and related optimization procedures will be discussed. The proposed capacitance sensor capabilities will be demonstrated by constructing and testing composite specimens with pre-induced defects with different sizes, locations, and types. Towards the end of this research program, it was felt that the principles behind the sensor operation can be applied to detect other damages in other structures. The capacitance sensors will be designed and used to locate poorly grouted zones in a concrete masonry wall.

1.3 Organization of the Thesis

Damage detection in composites using the capacitance sensing technique will be presented in this thesis. Chapter 1 provides an introduction and the objectives of this research. Chapter 2 reviews the most common damages and failure modes of composite materials, including the effects of such defects on the overall structural performance and integrity. This chapter also includes a literature survey of the existing NDE techniques used for the inspection and damage detection in composites. Some current applications employing the capacitance sensing techniques will also be highlighted in this chapter. Chapter 3 gives an overview and background of the capacitance sensor theory, and detailed analytical model and FEM of the proposed sensors. Chapter 4 discusses various aspects for the sensor design and optimization including the influence of defect size, location and type on the sensor responses. Chapter 5 presents experimental verifications to detect defects for different types of composite members demonstrating the proposed sensor capabilities to locate these defects. Finally, Chapter 6 highlights the key findings and contributions of the research, and provides recommendations for future work in this area.

Chapter 2: Literature Review

2.1 Introduction

The literature review in this study will be divided into three parts. The first part shows the different damages and failure modes in composite materials. Whereas delamination, matrix cracks and fibre rupture are considered the most common damages in composites. The second part goes through NDE techniques for damage detection in composites. Techniques, based on various physical principles including ultrasonic, radiography, thermography, vibration signatures, and eddy currents, will be highlighted. The third part of the review will attempt to cover the different applications of the capacitance sensors along with the different configurations used for these sensors. Applications range from void fraction measurements and flow pattern identifications to material properties measurements.

2.2 Type of Damages in Composite Materials

Composites may be subjected to different defects and damages that can significantly affect the strength and overall performance of the structures. The following sections discuss the potential defects and failure modes that may occur in these structures.

2.2.1 Delamination

Delamination is one of the most important failure modes in composite materials, as it refers to situations in which the failure occurs on a plane between adjacent layers within a laminate. This type of failure is dominated by the properties of the composites since their heterogeneity, anisotropy and toughness tend to be high (Zak et al. 2001). Such defects might occur under service loads, poor process control during manufacturing or other harsh environmental degradations. The delamination substantially reduces the stiffness (Toyama et al. 2002), and the buckling load capacity (Parlapalli and Shu 2004), which, in turn, influences the structure's stability characteristics. Small areas of delaminations are capable for reducing the compression strength of composite materials by over *50 %* (Cantwell and Morton 1992). Figure 2.1 shows the optical micrograph of a delamination in carbon fibre-reinforced polymers (CFRP) panel obtained by Gower and Sims (2004).

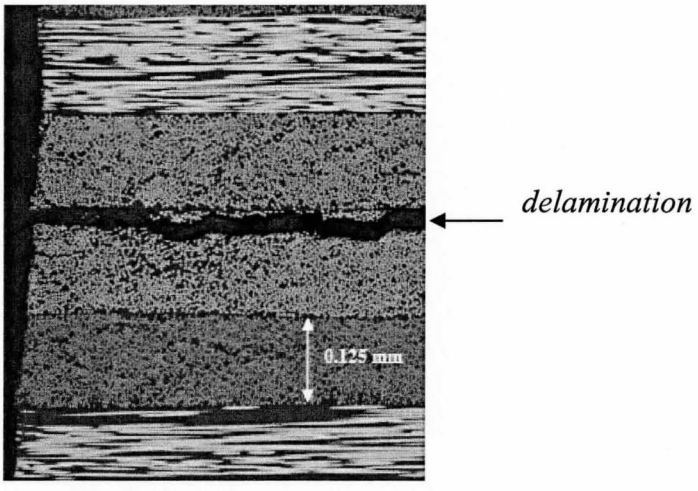

Figure 2.1: Micrograph for a delamination in CFRP panel (Gower and Sims 2004)

2.2.2 Fibre Rupture

The rupture of fibres can be critical and have severe influence on the stiffness and strength of the composites because these composite materials are typically designed to be fibre dominant, which means that the fibres represent the principal load-bearing constituent of a fibre reinforced composite. Fibre rupture usually occur due to transverse impact loading, or excessive compression fatigue cycling (Cantwell and Morton 1992). Figure 2.2 shows the fibre rupture in multidirectional CFRP laminate obtained by (Gower and Sims 2004).

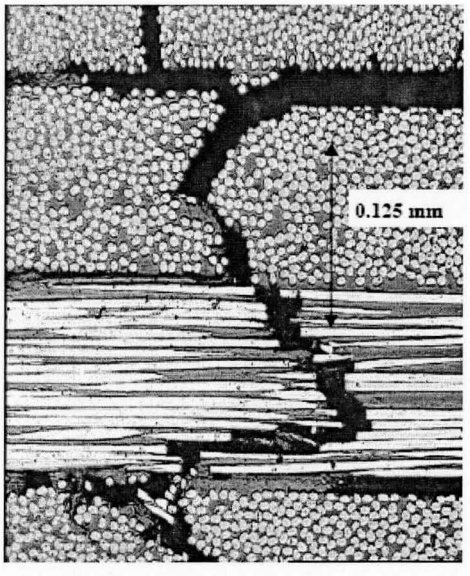

Figure 2.2: Micrograph for the fibre rupture in CFRP panel (Gower and Sims 2004)

2.2.3 Matrix Cracking

Matrix cracking is a very common failure mode in polymer matrix composites. These imperfections can occur in either parallel to the fibres or in matrix-fibre interfaces. Matrix cracking is usually localized and slightly reduce some of mechanical properties of

the material (Cantwell and Morton 1992). However, it can propagate through the laminate forming planes of weaknesses during service and certain conditions of fatigue and impact loading (Cantwell and Morton 1992). Figure 2.3 shows the matrix cracks in CFRP laminates of [0°/90°/0°] type.

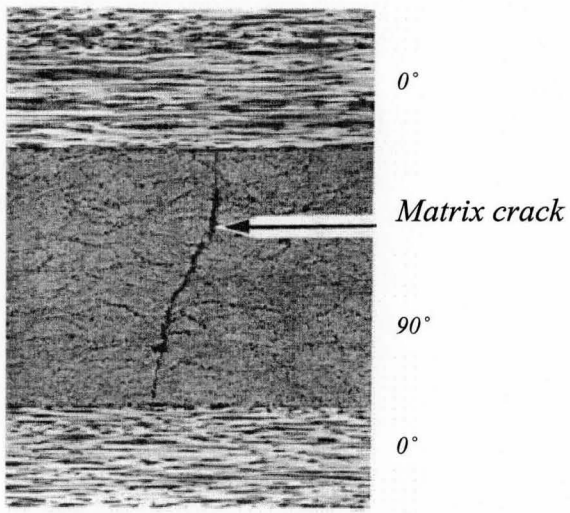

Figure 2.3: Matrix cracking in composites (Cantwell and Morton 1992)

2.2.4 Marcel Defects (Fibre Waviness)

Marcel defects are the out of plane undulation of an otherwise perfectly straight ply and usually occur in thick section composites during the manufacture process such as thermal expansion mismatch, instabilities encountered during forming operations and cure cycle (Caiazzo et al. 1999). Fibre waviness can lead to a reduction up to *60%* in stiffness and *65%* in compressive strength of the composite structural component (Bogetti et al. 1992) . Figure 2.4 shows a marcel defect in CFRP composites (Caiazzo et al. 1999).

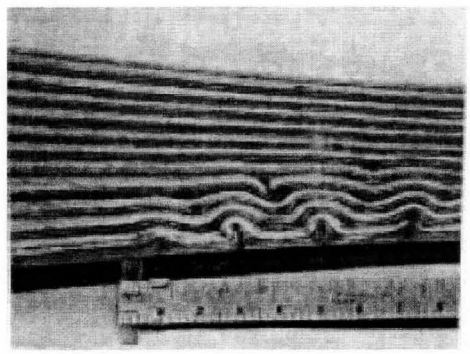

Figure 2.4: Marcel shape in CFRP composites (Caiazzo et al. 1999)

2.3 Nondestructive Evaluation Techniques

Currently, there are many NDE techniques that could be used for evaluating damages and assessing the integrity of composites. Their operation principals, shape, and size can be significantly different from each other depending on the applications. Most of these methods, such as ultrasonic, eddy current, thermography, and radiography, rely on evaluating acoustic, electrical or mechanical properties of composite structures. The available NDE techniques to date to evaluate the damages in composites are discussed in the following section.

2.3.1 Ultrasonic

Ultrasonic methods have gained a wide acceptance as a NDE technique for flaws detection and the quality control of structures. Ultrasonic techniques depend on the propagation and reflection of sound waves within the material, and the defects are estimated by analyzing the reflected signals. The propagation waves are generated by transducers, which transmit pulses of sound waves. If flaws or discontinuities are present

in the wave path, some or all of the energy is reflected back from the flaw surface to the search unit, as shown in Figure 2.5.

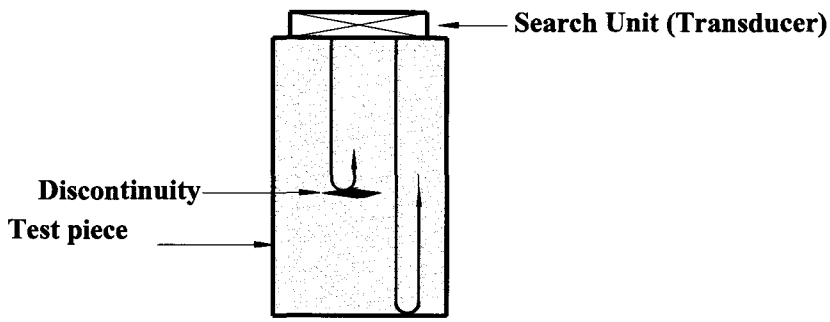

Figure 2.5: Pulse-echo ultrasonic testing

The reflected wave is transformed into an electrical signal which is recoded and displayed in four different ways (Khan 1999): (1) *A*-scan is a basic component of 'pulse echo' system and refers to a single point measurement as it displays the discontinuity depth and the signal amplitude of the inspected point, (2) *B*-scan refers to the measurement along single line as the discontinuity depth and its distribution are displayed in a cross sectional view, (3) *C*-scan is a collection of *B*-scans and displays the discontinuity distribution in a flat view forming a surface contour plot, and (4) *Digital Readout* displays the information of ultrasonic flight time and sound velocity readings in digital formats.

In most of ultrasonic applications, the transducer has to be in contact with the tested object with a couplant inbetween. Cauplants are used to reduce the impedance mismatch between the air and the material being inspected. Several techniques, however,

are available in these days introducing air-coupled ultrasonic for non contact NDE testing by using high sound pressures, or high sensitivity receiving transducers (Hillger et al. 2004; Imielinska et al. 2004).

Ultrasonic techniques for damage detection in composites have been studied by several authors. Mouritz et al. (2000) studied the low-frequency pulse-echo ultrasonics to detect the fatigue damage in thick glass fibre-reinforced polymers (GFRP) used in large ships. The study included monitoring the initiation and growth of fatigue-induced damage during cyclic flexural loading. A four-point flexural test was used to induce fatigue fracture in the composite specimens. The *A*-scan records were transferred from the ultrasonic unit to a computer. The results indicated that the damages (delaminations, debonding and matrix cracks) induced by a high stress fatigue loading above *50 %* of the static failure stress were easily detected, Figure 2.6 shows the high stress fatigue damage where the arrows indicate the directions of ultrasonic transmission waves, while the cracks occurred by low stress fatigue were difficult to detect because they grew parallel to the direction of the transmitted ultrasonic waves, as shown in Figure 2.7.

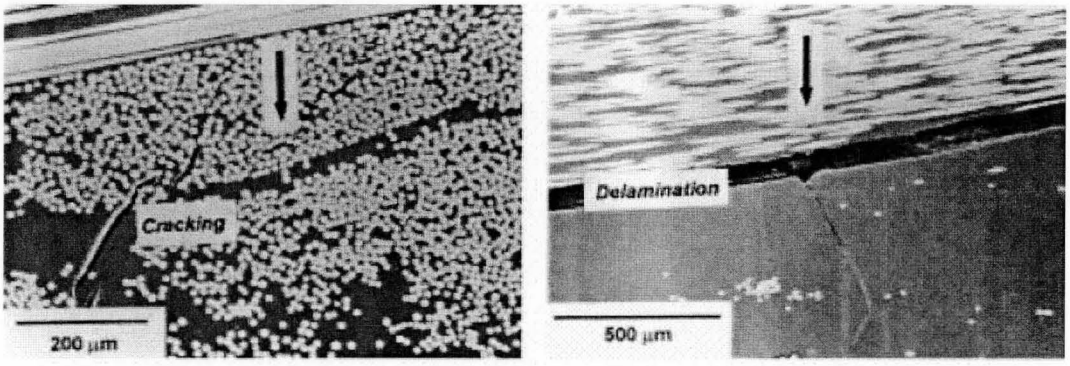

Figure 2.6: The damage caused by high fatigue stress (Mouritz et al. 2000)

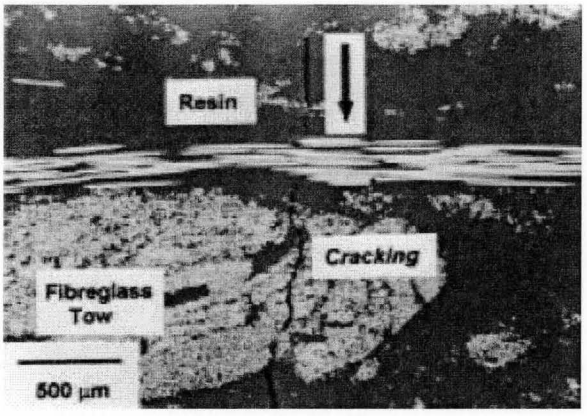

Figure 2.7: The cracks caused by low fatigue stress (Mouritz et al. 2000)

Aymerich and Meili (2000) introduced a combination of normal and oblique incidence pulse-echo ultrasonic that can produce a highly detailed volumetric image of matrix cracks and delaminations caused by low energy impacts on composite laminates. The specimens were $90 \times 90\ mm^2$ composite square plates with ply thickness of *0.12 mm* and a total thickness of *2.2 mm*. Drop weight impact test was performed with different falling masses and drop heights to produce different impact energy ranging from *3.6* to *5.0 J*. This study showed that the delamination could be detected by orienting the probe at a normal incidence while the matrix cracks were easily resolved by oblique incidence technique. Figure 2.8 shows ply-by-ply *C*-scans of delamination and matrix cracks in a *5.0 J* impacted plate.

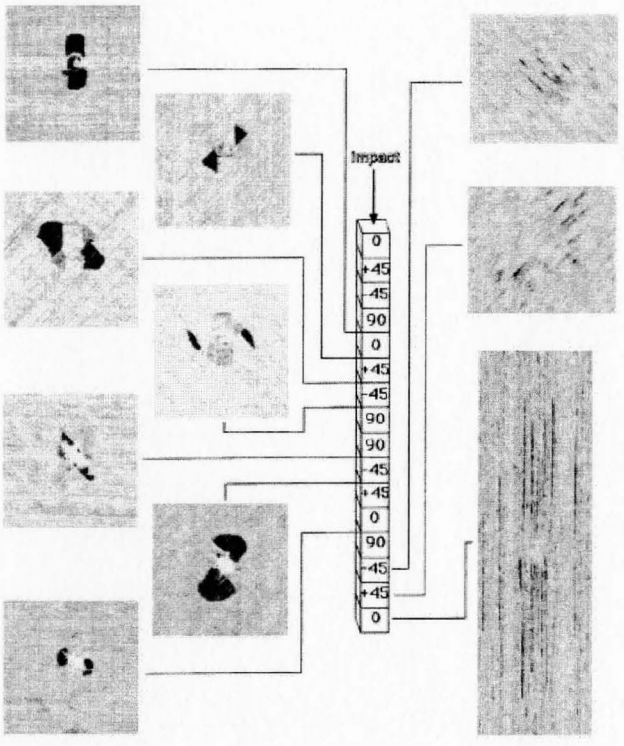

Figure 2.8: *C*-scans of a *5.0 J* impacted plate (Aymerich and Meili 2000)

Later, Hillger et al. (2004) implemented air coupled ultrasonic imaging techniques for testing a sandwich composite material. The sandwich test specimen was made of three layers: the outer layers were of CFRP skins (*1.25 mm* thickness each) and the core was of foam material. The specimen dimensions were of $487 \times 171 \times 35.7$ *mm* containing several artificially inserted flaws: delaminations of width *10 mm* between the upper and the lower skin, bore holes of diameters *8* and *10 mm*, as shown in Figure 2.9. For ultrasonic testing, a pair of transducers with a nominal frequency of *200 kHz* was used. Figure 2.10 shows a *C*-scan of the sandwich specimen, which gives an indication of all defects.

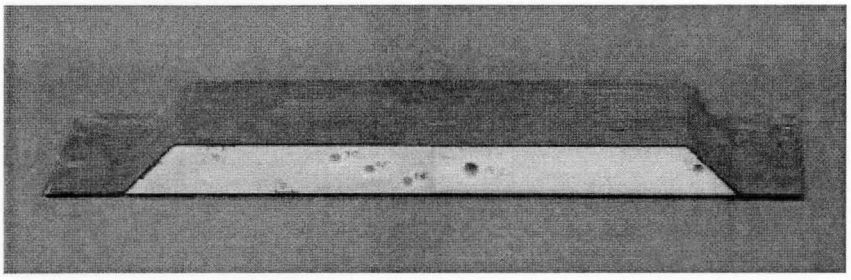

Figure 2.9: CFRP sandwich specimen with inserted defects (Hillger et al. 2004)

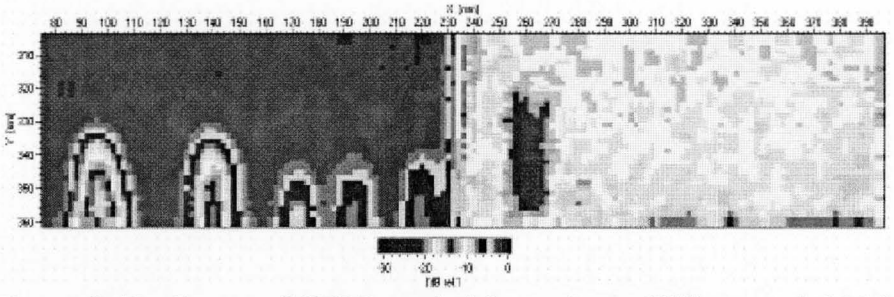

Figure 2.10: *C*-scan of CFRP sandwich specimen (Hillger et al. 2004)

Recently, Kang et al. (2006) used ultrasonic *C*-scan technique for the inspection of delamination and impact damages in honeycomb composite plates. The honeycomb composite had cores made of aluminum and skins made of CFRP. Two artificial damages were induced in two honeycomb specimens: Specimen *A* contained a Teflon film of diameter *30 mm* and Specimen *B* had a square impact damage. Figure 2.11 shows the inspection results of the artificial delamination and impact damage.

Generally, ultrasonic testing is completely nondestructive and is a well established test for damage detection in composites. Ultrasonic methods cause no environmental or health risks. However, the technique has several shortcomings and limitations. Inspection by ultrasonic requires highly experienced operators to properly

acquire and interpret the data. Other difficulties include requiring a coupling medium and the problems associated with detecting the localized surface flow and transverse cracks, (Mix 1987).

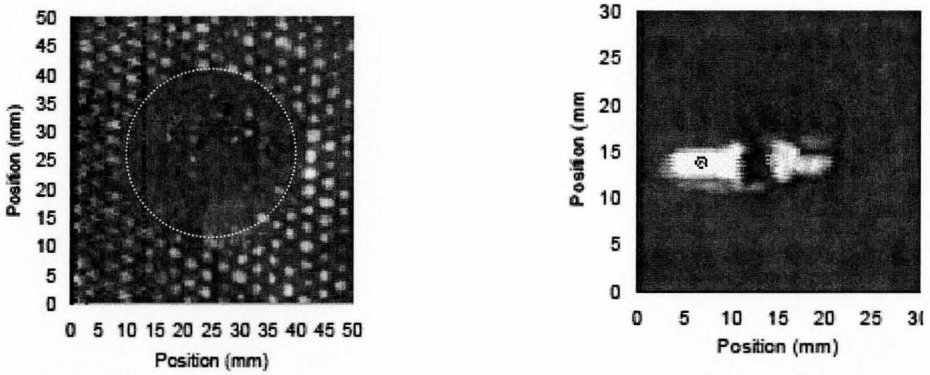

(a) C-scan image of specimen A *(b) C-scan image of specimen B*

Figure 2.11: Inspection results for delamination and impact damages (Kang et al. 2006)

2.3.2 Vibrations-Based Techniques

Vibrations-based NDE techniques rely on estimating damage events by comparing dynamic responses between damaged and undamaged members. Structures can be excited by an external shaker, ambient energy, or embedded actuators and the dynamic responses are then recorded. The presence of damage is predicted when changes in the structural frequency, the modal stiffness, damping, or the structural mode shape occur. The research focus is on the numerical analysis or experimental technique to obtain the dynamic responses of composite structures containing predetermined damage parameters.

Several authors have studied the possibility of detecting damages in composites by analyzing the changes in natural frequencies of the object be inspected (Cawley and Adams 1979; Tracy and Pardoen 1989; Kessler et al. 2002). The basis of these methods is that damage changes structural properties such as stiffness, which, in turn, changes the natural frequencies, and the damage location can be detected from the degree of change in the natural frequency, that depends on the position of the damage for a particular mode of vibration.

Paolozzi and Peroni (1990) used finite element models to calculate the frequency shifts resulting from debonding in composite structures. The structure was a panel with CFRP faces and honeycomb core. The results showed that the maximum frequency shifts occurred in the modes where the wavelength was approximately the same as the size of the debonding area. Another study was conducted by Shen and Grady (1991) who developed a mathematical model to determine the natural frequencies and corresponding mode shapes based on the Timoshenko beam theory for a composite beam with one dimension delamination. Both natural frequencies and mode shapes were very sensitive to the presence of delamination. Later, Tenek et al. (1993) studied the effects of delamination on the natural frequencies of composite plates based on the three-dimensional theory of linear elasticity. The results exhibited that large delamination sizes had no significant effect on the lower natural frequencies, while a reduction was observed in natural frequencies proportional to the delamination size and number for higher frequencies.

Using damping as one of dynamic parameters can also be a good indictor for damages in composites. Although damping is a complex factor to be considered, it can be more sensitive in damages than frequency shifts especially in small and medium cracks (Zou et al. 2000). Adams et al. (1975) found that damages in GFRP composites could be detected by a reduction in the dynamic stiffness and increase in damping factor, whether this damage was localized, or distributed through the specimen. Later, Lee et al. (1987) studied the variation of the damping coefficient versus the location and damage severity in cantilever beams. Cantilever beams were excited with a forcing hammer. A non-contact motion transducer was used to measure the displacement at the free end of the beam. The results showed that the damping factor was sensitive to delamination especially for higher modes since a good correlation between the delaminated area and the increase in damping coefficient was established. However, no measurable changes in damping were detected as a result of the matrix cracks. In addition, notches, less than *5%* of the cross-sectional area, were difficult to detect.

Composite defects can be determined by monitoring changes in mode shapes of members. Mode shapes can be defined as the spatial description of the amplitude at each resonance frequency. Delaminations cause irregularity of mode shape curves depending on the size and location of the delaminations. However, small delaminations (less than 10% of beam span) may not be detectable by monitoring mode shapes of the beam (Zou et al. 2000).

Vibration-based techniques provide global information about the investigated structure by identifying and analyzing specific dynamic response. However, global

parameters do not change significantly when small local damage takes place. Another challenge is the extraction of signals for on-line damage detection, which rely on the ability to distinguish between changes in vibration signature due to damages and changes due to normal usage such as environmental vibrations or changes in the boundary conditions of the structure. Laboratory experiments are often conducted under controlled conditions to ensure that the changes are only due to the damage under investigation (Zou et al. 2000). Therefore, to develop practical and capable on-line damage detection methods based on evaluating the vibration signatures, significant research efforts remain to be performed.

2.3.3 Radiography

Damage detection in composites using radiography is one of the oldest and most widely used NDE techniques. Radiography is a photographic record produced by the penetration of electromagnetic radiation such as X-rays or Gamma rays through the inspected object onto a film or other media, as shown in Figure 2.12. A radioactive isotope or X-ray machine is used as a source of radiation. The degree of blackening of various portions of the X-ray film after processing is determined by the absorbed radiation dose, which, in turn, depends on the density, thickness, and homogeneity of the object (Mix 1987).

Radiography technique was found to be efficient in detecting the composite material defects. Chang et al. (1975) used X-ray technique to monitor the damage propagation at increasing load levels in composite specimens with different laminate configurations. A *110 kV* portable X-ray unit was used as a radiography energy source.

All specimens were loaded with a load rate *40 Ib/min.* An X-ray exposure was made at each *50-100 Ib* interval. The results showed that, in low-stress region, a slow damage growth rate was observed, while an accelerated growth rate in high-stress region was occurred. It was also found that the existence of short damage lines prior to load application did not affect the history of damage growth.

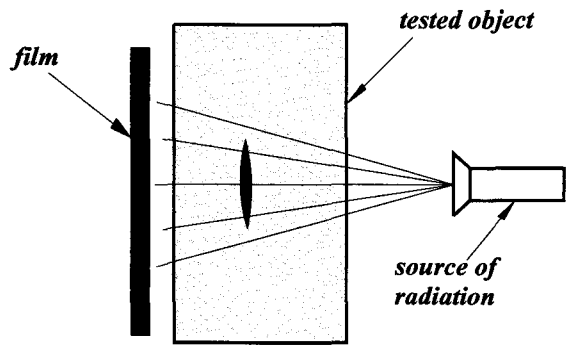

Figure 2.12: Radiography testing technique

Jama et al. (1998) assessed the integrity of bonded composite joints by using Gamma-ray radiography making use of the fact that the amount of photon scattering is proportional to the electron density of the material. In this technique, a narrow beam of monochromatic photons was directed towards the joint and scattered photons were recorded, using a detector located on the same side as the source, as shown in Figure 2.13. The energy of the scattered radiation was measured and related to the angle of scattering. The debonding areas were detected by corresponding energy changes in its location.

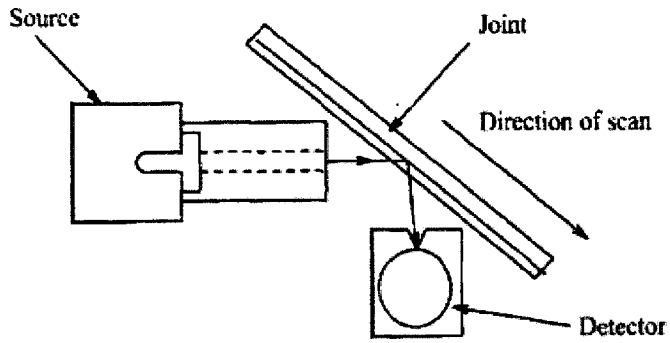

Figure 2.13: Schematic representation of the Gamma-ray technique (Jama et al. 1998)

Later, Dunn and Yacout (2000) utilized a limited-scan X-ray backscatter technique to detect damages under aircraft skins. Both simulation and laboratory experiments on a portion of aircraft surface were conducted, the results indicated that as little as *5%* material loss at depths up to *0.20 in.* and *10%* material loss at depth up to *0.25 in.* beneath aircraft skin could be detected.

Radiography techniques are relatively inexpensive and simple to implement and interpret. However, they require large and costly equipments and extensive production against radiation hazards. The greatest challenge in using X-ray radiography is its requirement to access both sides of the surface of the composite structures in order to emit and collect the X-ray radiation, which is often not practical.

2.3.4 Infrared Thermography

In recent years, the use of Infrared Thermography (IRT) becomes increasingly attractive for damage detection in composite materials. IRT is a non-contact NDE technique currently used successfully to locate subsurface flaws in FRP laminates and

other damaged composite materials. The technique is based on changes of the heat flow through the material by the presence of defects and/or debonded areas. In locations where the composite layers are not in contact, the heat transfer will be slower than in those where there is intimate contact. These changes in heat flow cause localized temperature differences in the material which can be detectable by infra-red (IR) cameras and appear as hot spots, Figure 2.14 shows the illustration of IRT inspection process, (Levar and Hamilton 2003).

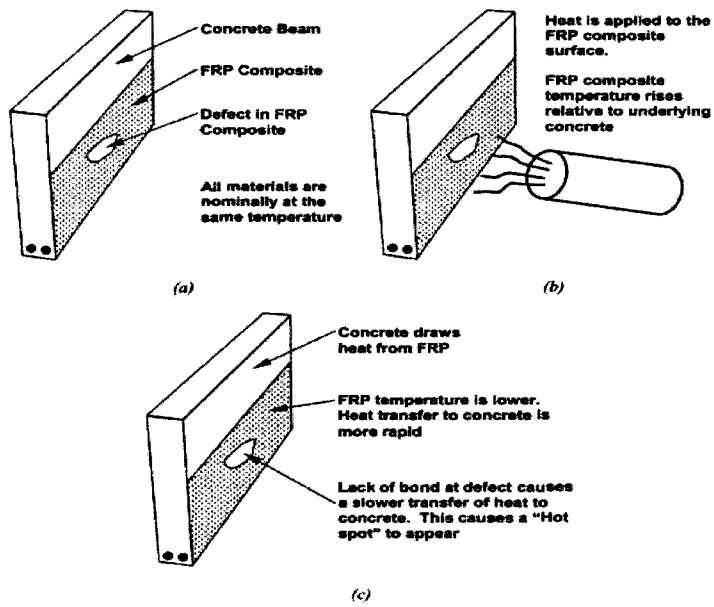

Figure 2.14: IRT inspection for FRP/concrete (Levar and Hamilton 2003)

Several studies were conducted to investigate the capabilities of using thermography for composite structures inspection. Dattoma et al. (2001) used thermographic technique to detect defects in wind-turbine blade. The blade-shell was

made of three layers sandwich composite, the outer layers were of GFRP laminates and the core was made of a *10 mm* thick foam, as shown in Figure 2.15. In order to identify the thermal response of the potential defects, an experiment was carried out on a small sandwich composite specimen with artificial defects. The specimen was made of three layers sandwich composite and had the same structure as the shell of the turbine blade.

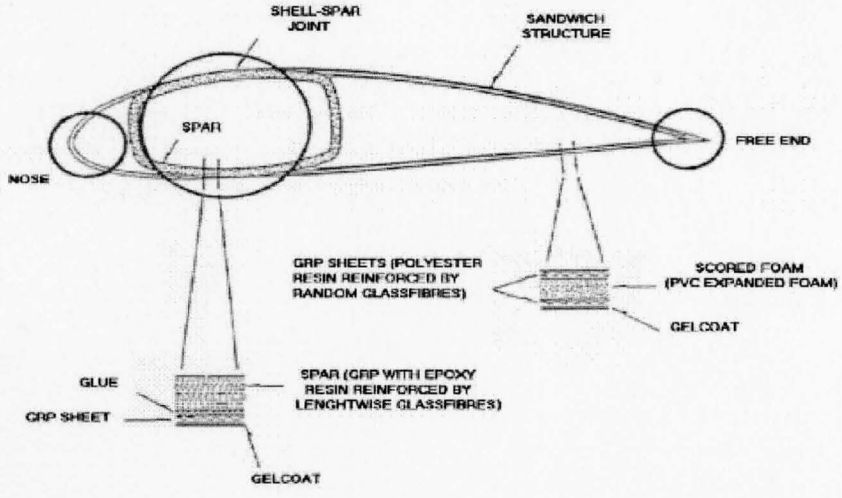

Figure 2.15: Schematic of the blade turbine section (Dattoma et al. 2001)

Three types of artificial defects were inserted to the specimen: glue infiltration, disbond and water ingress. The experiments were carried out by using a hot air blower to heat the specimen. The heat source was kept *50 - 70 mm* from the specimen and the camera was held *700 mm* from the sample. Each thermal response, related to a corresponding defect, was listed and used as a reference for the inspected turbine blade. A *2.0 m* section of *17.0 m* long blade was considered for the inspection. Figure 2.16 shows the thermal image for the tested blade. By comparing the images for the blade experiment and those obtained from the sample, disbonded areas between the skin face

and the core were found. In addition, the presence of glue infiltration areas in the foam was also identified.

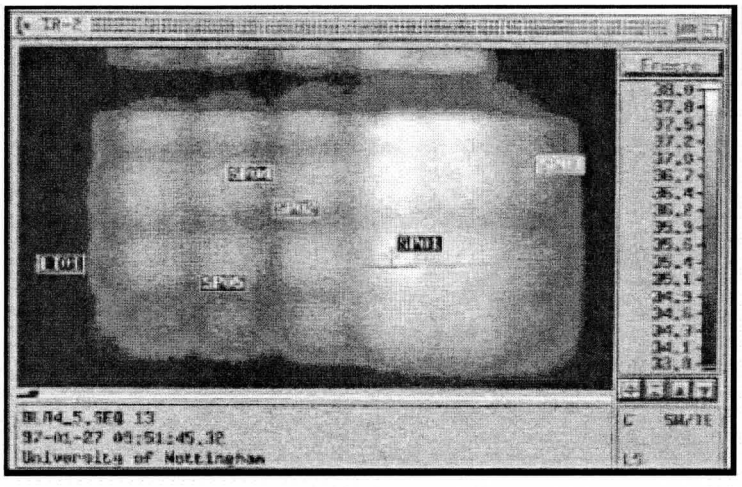

Figure 2.16: Temperature map for the blade indicating disbond and glue infiltration defects (Dattoma et al. 2001)

Another study was conducted by Halabe et al. (2002) who used IRT to detect delaminations in two types of GFRP composite members. The first type was of *50 × 100 mm* hollow box sections of different specimens containing delaminations of different sizes inserted in these box sections during the pultrusion process. The second type consisted of bridge deck modules with subsurface delaminations. Figure 2.17 shows the box specimen having a *3" × 3"* delamination and the gray scale IR image of the specimen. As can be seen in the image, the delamination is indicated as a bright spot. Figure 2.18 shows the delaminated deck bridge and its gray scale IR image. Infrared thermography was very successful in predicting the locations as well as the shapes and relative sizes of the subsurface delaminations.

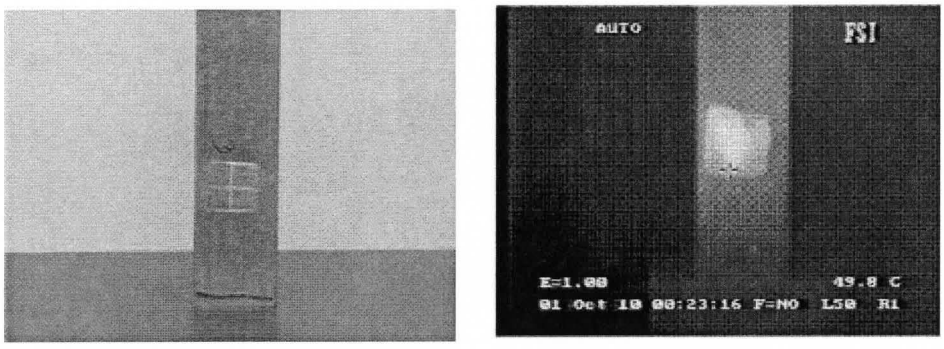

Figure 2.17: The delaminated box specimen and IR image (Halabe et al. 2002)

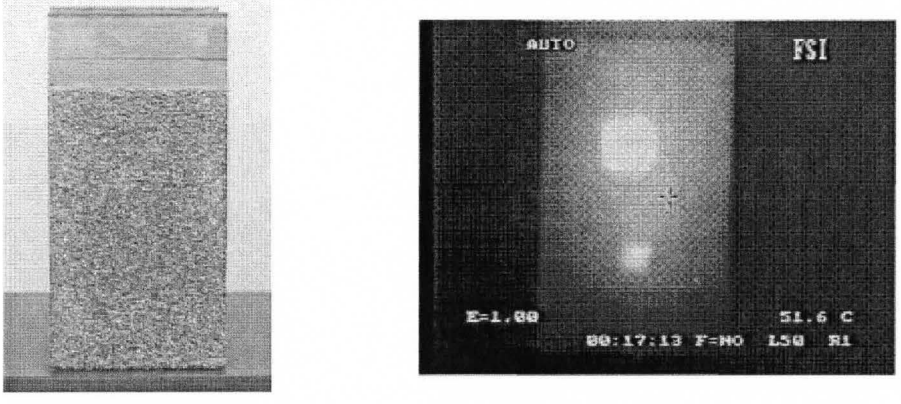

Figure 2.18: The delaminated GFRP bridge deck and the IR image (Halabe et al. 2002)

Later, Levar and Hamilton (2003) utilized IRT technique to evaluate the bond between CFRP composites and concrete. This study involved the structural load testing of small-scale RC beams that were strengthened with CFRP and forced for either shear or flexural failure mode. A heating source of a *500 W* halogen lamp was used to heat the CFRP surface and an IR camera was used to monitor the surface temperature profile during cooling. The loss of bond was consistently evaluated with load increasing and

patterns of debonding were monitored as all tested beams were loaded to failure. The results showed that IRT can be used effectively for identifying debonded areas between concrete and CFRP. The total debonded area increased as the load was increased up to failure.

Starnes et al. (2003) involved both experimental investigations and *2D* finite element simulations of IRT of FRP laminates applied to concrete structures. A controlled-flaw specimen was used to study the response of simulated flaws at the interface of FRP laminate and concrete substrate. The specimen was of $610 \times 250 \times 45$ *mm* of precast concrete slab as the substrate with two bonded layers of CFRP. Eight flaws of 25×25 *mm* were created by placing different materials at the interface between the concrete substrate and the CFRP laminate. The result showed that all simulated flaws were detectable. The most visible flaws were those with low thermal conductivity such as fabric, air, and ceramic paper, while flaws of masking tape and parafilm materials gave the smallest thermal signals. Figure 2.19 shows the thermogram for the tested specimen. Good agreement was found between experimental thermal response parameters and those obtained from finite element simulations.

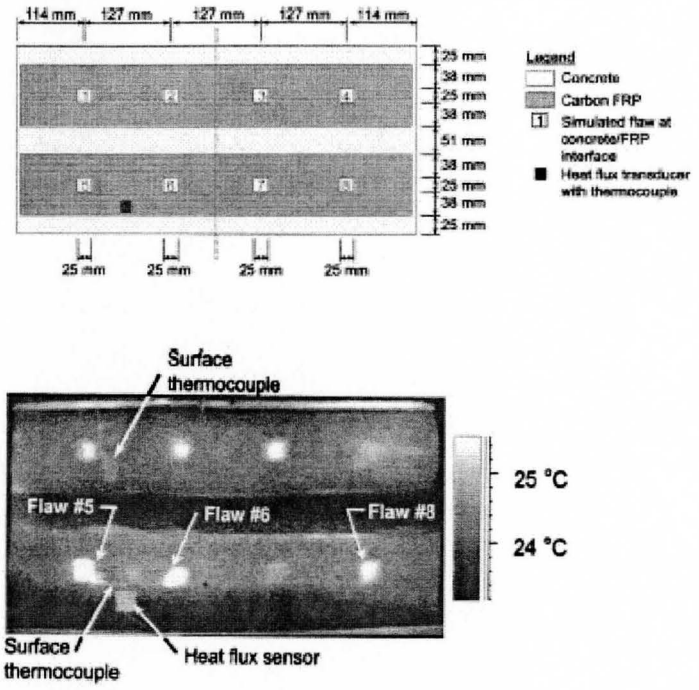

Figure 2.19: Controlled flaw specimen and its thermal image (Starnes et al. 2003)

Recently, Kang et al. (2006) used IRT for inspecting honeycomb composite plate. The honeycomb composite material was made of aluminum core and the skins were made of CFRP. A Teflon film of diameter of *30 mm* was induced as an artificial delamination in one of the specimen and the other specimen was subjected to impact damage. Figure 2.20 shows the thermal image of an artificially delaminated plate, the delamination is identified by the circular spot. The delamination size was estimated from the thermal image as *31.4 mm*. Figure 2.21 shows the thermographic result at the impacted side of honeycomb composite. The defect was identified by a black spot.

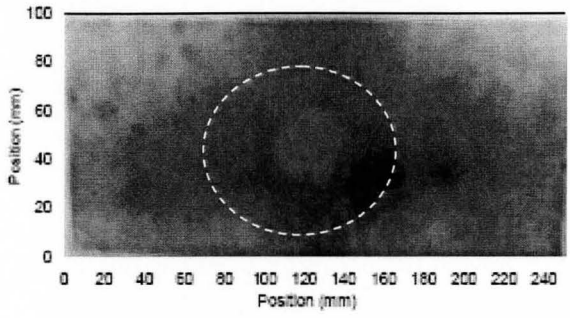

Figure 2.20: Thermal image of the artificial delamination (Kang et al. 2006)

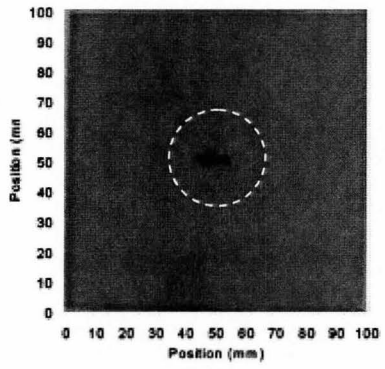

Figure 2.21: Thermal image of the impacted plate (Kang et al. 2006)

Thermography can offer a relatively broad area inspection and presents a useful inspection tool for thin flat structural components, however, the application of IRT for complex geometries is not widely accepted and the majority of the analytical and numerical studies are restricted to simple planar geometries. Moreover, the principal disadvantage associated with it is its inspection penetration depth, as thermography is effective only for detecting near surface discontinuities such as delaminations, debondings, voids and moisture zones (Krishnapillai et al. 2005).

2.3.5 Eddy Current

The eddy current method was pioneered by Friedrich Forster in 1940. Eddy current tests are based on a process called electromagnetic induction and can be used for all electrically conductive materials. When an alternating current is applied to the conductor, such as copper coil, an alternating magnetic field is produced in and around the coil. If this coil is brought near another electrically conductive material, the material being inspected, the alternating magnetic field penetrates the material and generates circular eddy currents. The induced eddy currents will generate their own secondary magnetic field, which will oppose the coil's primary magnetic field. As a result, changes take place in the components of the coil's impedance. Flaws and cracks in the inspected material obstruct the eddy current flow which reduces the secondary magnetic field and increases the impedance, (Mix 1987). Figure 2.22 illustrates the eddy current procedure, (Sadler and Ahn 2001).

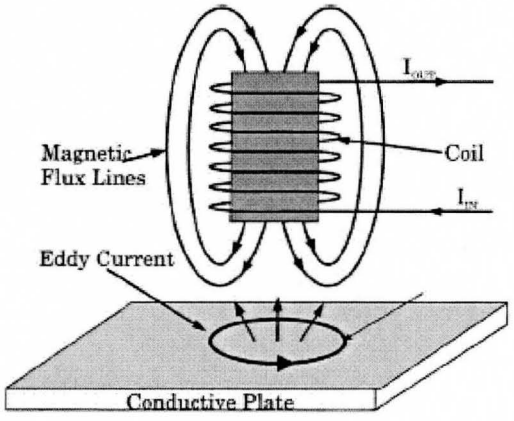

Figure 2.22: Eddy current technique procedure (Sadler and Ahn 2001)

Lane et al. (1991) evaluated the feasibility of the eddy current NDE technique for inspecting graphite/epoxy composite materials. Three type of defects were induced in graphite/epoxy specimens: simulated delaminations that were created by inserting pieces of plastic film, which did not bond to the graphite/epoxy during the lay up process, broken fibres caused by tensile testing of the sample to failure (*300 MPa*) and impact damage induced by subjecting the sample to different impact energies from *7.5* to *19.9 J*. The results exhibited that there were good correlations between the location of the broken fibres and impact damages and eddy current responses, while eddy currents were not sensitive to delamination locations. However, eddy current might be used to discriminate delaminations with broken fibres from those without broken fibres.

Eddy currents sensors together with a mechanical scanner were used by Mook et al. (2001) to characterize and evaluate both the structure and flaws of CFRP composites. The eddy currents inside the CFRP were induced using a transmitter coil and the magnetic field was measured close to the surface of the specimen using a small receiver coil, as shown in Figure 2.23. This study indicated that eddy current sensors were capable of detecting the CFRP fibre orientation, local imperfection, material ageing, and impact damage. In addition, the ability to detect delaminations was demonstrated by using the inter-fibre and inter-laminar currents produced by the resistive and capacitive couplings between the fibres of a ply and between different plies.

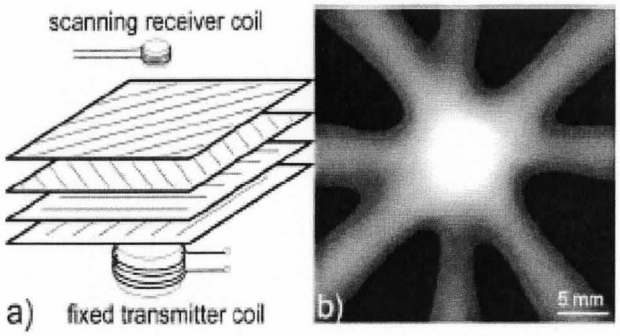

Figure 2.23: a) experimental setup for CFRP eddy current inspection b) gray scale representation of the magnetic field for the scanned area (Mook et al. 2001)

The advantage of eddy current testing over some other methods is that there is no need for physical contact with the surface of the object being tested. Moreover, it is simple, cost effective and has a relative rapid inspection speed. However, the technique has some disadvantages with respect to requiring high degree of operator skill to properly use test equipments, large amounts of power and complicated data interpretation. Eddy current is not suitable for inspecting of non-conductive materials and may not be sufficient method to detect delaminations and other planar defects.

2.4 Capacitance Sensor Applications

Capacitance sensors are widely used in the industry and laboratory experiments to measure various parameters. The material physical property of interest is evaluated by measuring the capacitance across the sensor. The resulting capacitance depends on the dielectric properties of the material compositions, which considered as characteristic signatures of the materials, and the sensor's geometrical parameters. The use of these sensors requires a calibration process in order to establish a quantitative relationship between the material property and the resulting capacitance measurements.

Capacitance sensor can provide a non-intrusive way to measure the void fraction in multi-phase flow. In addition, the time-varying output signal can be used for flow pattern identification, (Elkow and Rezkallah 1996). Several sensor configurations including concave, helical, and multiple helical type have been investigated by (Strizzolo and Converti (1993), and Lowe and Rezkallah (1999). Recently, Ahmed (2006) compared the performance of two capacitance void fraction sensors: one with two ring electrodes (Ring type), and the other consisted of two concave parallel electrodes mounted on opposite sides of the tube (Concave type), as shown in Figure 2.24. This study involved conducting several void fraction measurements in air-oil two-phase flow. It was found that the ring type sensor proved to be a great improvement over the concave sensor, since the results showed that, for the same spatial resolution, the ring type sensors are more sensitive to the void-fraction signal than the concave sensors and it is capable of identifying between different flow patterns.

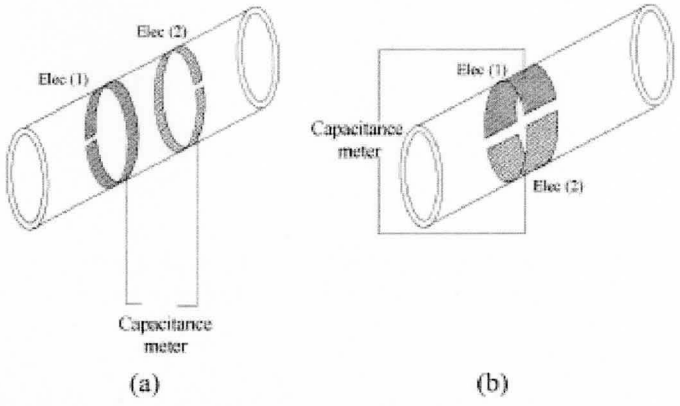

Figure 2.24: Void fraction capacitance sensors, (a) Ring type and (b) Concave type, (Ahmed 2006)

Li et al. (2005) used a capacitance sensor for measuring suspended sediment concentration. Two sensors, in the form of plates and cylinders, were investigated. The results showed that the outputs of capacitance sensor were linearly correlated with suspended sediment concentrations. In addition, both the sensor configurations gave a similar sensitivity. Later, Thong-un et al. (2006) introduced a capacitance sensor for chemical concentrate measurements. The sensor consisted of two-parallel plate that were coated by Nylons and mounted together by resin that limited the gap of the two plates in the specific distance, as shown in Figure 2.25. Two sensor- ratios (gap to width) were used to test Ethyl Alcohol solution within a concentration ranging from *5.0 %* to *95 %*. The results showed that the sensor with a gap *10 %* greater than electrode width could provide the results with a high linearity as well as high resolution of capacity change, which was *2.0 pF* per *1.0 %* of concentration.

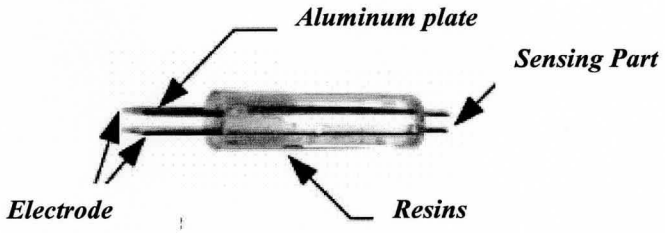

Figure 2.25: Capacitance sensor for concentration measurements (Thong-un et al. 2006)

A rain capacitance sensor was introduced by Bord et al. (2006). The sensor consisted of protected three coplanar electrodes. This study showed that the sensor was capable of detecting water films as less thickness as $50\ \mu m$ and water droplets as small as $5\ \mu m$.

Other applications of the capacitance sensors include measuring liquid-film thicknesses (Ozgu et al. 1973), detecting the interface in oil and gas extraction plant [(Jaworski et al. 1999); (Meng et al. 2006)] and monitoring water content of manufactured product in a production line (Tsamis and Avaritsiotis 2005).

Another capacitance sensor configuration, which has gained a lot of acceptance in last few years, is the Interdigital Capacitance Sensor (IDCS). IDCS is composed of two comb-like electrodes that are alternately arranged, as shown in Figure 2.26, The most important advantages of the IDCS over the different other configurations are that it provides the feasibility to control the strength of output signals by changing the number of fingers and the spacing between them, (Mamishev et al. 2004). The use of IDCS have been studied for applications such as monitoring the ultrathin polymeric film growth

(Zhou et al. 1988), and the estimating the moisture content in cookie dough (Li et al. 2003), and in paper pulp (Sundara-Rajan et al. 2004).

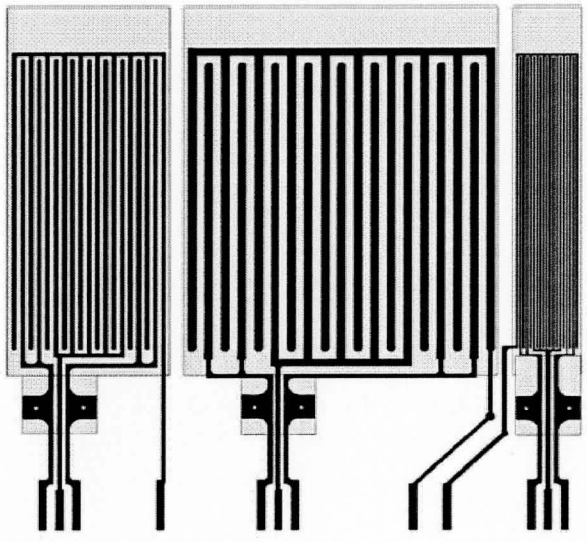

Figure 2.26: Interdigital Capacitance Sensor (IDCS) (Mamishev et al. 2004)

2.5 Conclusions

In this chapter, the various damages and failure modes that may occur in composites were discussed. Delaminations, fibre rupture, matrix cracks and marcel defects are considered most common defects in composite materials. Delaminations and fibre rupture have great influences on the structural overall performance and integrity as they affect the stiffness and strength of the composite members. Matrix cracks can propagate through composite laminates producing a weakness and delaminations planes.

Several nondestructive techniques for evaluating these defects have been reviewed and discussed. These techniques include ultrasonic, thermography, radiography, vibration based technique and eddy currents. They have many advantages and at the same time, each technique has its own disadvantages. Each method presents some limitations in terms of its ability to detect and characterize defects. Ultrasonic methods proved to be promising for their application; however, they have several shortcomings regarding the cauplant medium requirement and highly experienced operators. Although thermography technique facilitate inspection of large areas, it is not effective for complex structures. Radiography techniques require access both sides of the composite structures and extensive production against radiation. Vibration based techniques provide only global information for the structure about investigated structures. Eddy current methods are not suitable for detecting delaminations and non-conductive material inspection. Capacitance sensing techniques have several applications in the area of nondestructive tests and material properties evaluations. Measuring the void fraction in multi-phase flow, film thickness, water content in industrial products and the components concentration in chemical solutions along with determining the separation surface of the oil and gas extraction plant are the most important applications of capacitance sensing method.

Chapter 3: Capacitance Sensor Modelling

3.1 Introduction

This chapter will highlight the needed background of electrostatic in order to facilitate understanding the modelling and operation of the capacitance sensors. The theory of the capacitance technique will be highlighted using the simple parallel plate capacitor. The effect of dielectric material properties on the resulting capacitance and the electric field generated between the capacitor plates will be discussed. In addition, the chapter will also present analytical models for the proposed Coplanar Capacitance Sensor (CCS) and Interdigital Capacitance Sensor (IDCS) based on conformal mapping technique. Two-dimensional (2D) Finite Element Model (FEM) for the proposed sensors using commercial FEM software will be presented. FEM is a powerful tool to estimate the capacitance and represent the electric field distribution across the capacitance sensor electrodes. The analytical models and FEM will be employed in the following chapter to examine the sensor geometrical parameters on the sensor outputs and to optimize the sensor designs.

3.2 Electrostatics Background

This section provides an overview of the basic framework of electrostatics in order to facilitate understanding the governing parameters that may affect the design of capacitance sensors (Hayt and Buck 2001) and (Ulaby 2005).

3.2.1 Coulomb's Law

Coulomb's law states that the force, F, in Newtons, between two small charged conductors in a vacuum with charges q_1 and q_2 Coulombs and separated by a distance, r, meters is:

$$F = \frac{q_1 q_2}{4\pi\varepsilon_0 r^2} \tag{3.1}$$

where ε_0 is the permittivity of the vacuum and has a value equals to $8.8541 \times 10^{-12}\ F/m$. Coulomb's law shows that the force is proportional to the product of the magnitudes of the two charges and inversely proportional to the square of the distance between them.

3.2.2 The Electric Field and Electric Flux Density

The concept of the electric field, E, is used to help visualize how a charge, or a collection of charges, may affect the region around it. The electric field intensity at a point in space due to an array of fixed charges may be defined as the electric force, F, per unit positive charge, $+q$, placed at the specified point; in other words:

$$E = \frac{F}{+q} \tag{3.2}$$

The electric field, E, has dimensions of force per unit charge, and units of Newton per Coulomb (N/C).

A field line is defined as a line drawn tangent to the electric field vector at each point in space starting from the positive charge and ending by negative charge. The density of the lines in a given region is proportional to the magnitude of the field at this region.

In addition to the electric field intensity, E, it is convenient to also use a related quantity called the Electric Flux Density, D, in Coulomb per square meter (C/m^2) and given by:

$$D = \varepsilon_o E \tag{3.3}$$

3.2.3 Gauss's Law

Gauss's law describes the relationship between electric charge and electric field. It states that the surface integral of the normal component of the flux of electric force, over any closed surface with an area, a, in space, is directly related to the quantity of electric charges, q, contained in the space, bounded by that surface, divided by permittivity of free space, ε_0. This can be expressed as follows:

$$\iint_s \vec{E} . \vec{da} = \frac{q}{\varepsilon_o} \tag{3.4}$$

3.2.4 Capacitance and Capacitors

When two parallel plates of metal are connected to the two terminals of voltage difference, ΔV, charges move from the battery to the metal, as shown in Figure 3.1. The amount of charge, Q, stored in a capacitor is linearly proportional to the absolute electric potential difference, ΔV, between the capacitor plates, or:

$$Q = C|\Delta V| \tag{3.5}$$

where C is the proportionality constant which is referred to as *Capacitance*. Physically, the capacitance is ability to storing electric charge for a given potential difference ΔV.

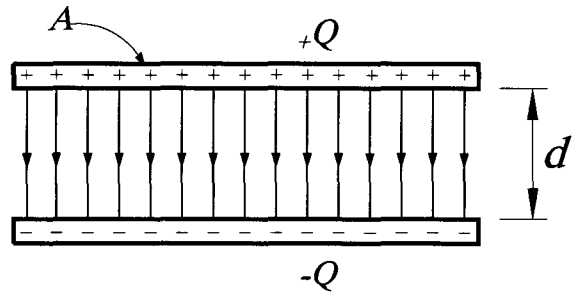

Figure 3.1: Parallel-plate capacitor

Graphically, the electric field lines are perpendicular to the surfaces of the plates and have equal magnitude, as shown in Figure 3.1. The equipotential lines (constant voltage) are parallel to the plates and occur at equal spacing. The potential difference between the plates is:

$$\Delta V = V_{-} - V_{+} = -\int_{+}^{-} E.ds \tag{3.6}$$

Therefore,

$$|\Delta V| = Ed \tag{3.7}$$

where d is the distance between the plates. The electric field, E, between the plates using (3.4) can be written as:

$$E = \frac{\sigma}{\varepsilon_0} \tag{3.8}$$

where σ is the surface charge density. By substituting for E , (3.7) can be written as:

$$|\Delta V| = \frac{\sigma d}{\varepsilon_0} \tag{3.9}$$

The total charge, Q, on the plate of the capacitor is σ multiplied by the area, A, of the plate. Therefore, the capacitance, C, of an idealized parallel plate capacitor can be expressed as:

$$C = \frac{\varepsilon_o A}{d} \tag{3.10}$$

The capacitance, C, is directly proportional to the surface area, A, of each plate and the permittivity of free space, ε_0, and inversely proportional to the distance, d, between the plates. This formulation neglects fringe effects since it assumes that the electric field is uniform across the gap between the plates and is zero elsewhere. In the *SI* unit system, the resulting capacitance values calculated with Eq. (3.10) are in units of *Farad* (F). In practice, *Farad* is a rather large quantity, and typical capacitance values are in *microFarads* or *picoFarads*, ($1\ F = 10^6\ \mu F = 10^{12}\ pF$).

3.2.5 Dielectric Materials

A dielectric material is a non-conductive material containing no free electrons in any noticeable numbers, and so no current flows through it. Such materials can be used to maintain a physical separation of plates. The capacitance value increases when the space between the conductors is filled with dielectrics rather than air.

To show the effect of dielectrics on the capacitance, a simple parallel plate capacitor with a dielectric material completely filling the space between the plates will be studied. The dielectrics contain charged molecules, which generally exist in random orientations, as shown in Figure 3.2-(a). When an external electric field, E, is applied, the dielectric is polarized, and a torque is set up that causes molecules to align, as shown in

Figure 3.2-(b). The aligned molecules then generate an electric field that is opposite to the applied field but smaller in magnitude.

Therefore, the polarization charge of density, P, appears on the two surfaces. Thus, the uniform field between the plates can be expressed as:

$$E = \frac{(\sigma - P)}{\varepsilon_o} \tag{3.11}$$

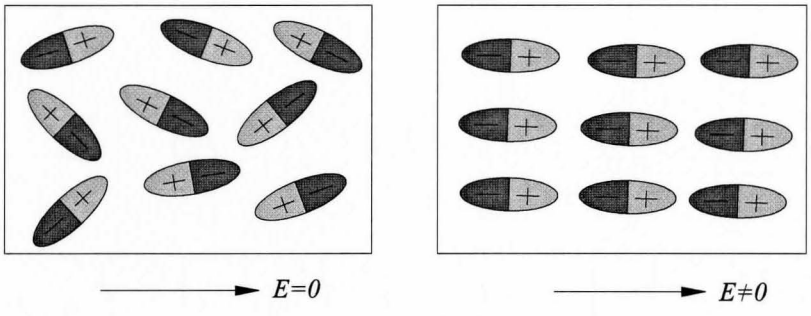

(a) random molecules (b) aligned molecules

Figure 3.2: Effect of dielectric materials on the parallel-plate capacitor

The polarization field, produced by the electric field, E, depends on the material properties. For homogeneous isotropic materials, the polarization field is directly proportional to E and is expressed by the following relationship:

$$P = \varepsilon_o \chi_e E \tag{3.12}$$

where χ_e is called the electric susceptibility of the material. By combining Eq. (3.11) and Eq. (3.12) and substituting in Eq. (3.7), the capacitance between the parallel plate capacitor can be written as:

$$C = \frac{\varepsilon_o (1+\chi_e) A}{d} \tag{3.13}$$

or

$$C = \frac{\varepsilon_o \varepsilon_r A}{d} \tag{3.14}$$

where $\varepsilon_r = (1+\chi_e)$ is the relative permittivity (the dielectric permittivity) of a material. By comparing Eq. (3.14) with Eq. (3.10) for the capacitance of a parallel plate capacitor in vacuum, it can be found that the capacitance increases by a factor ε_r which is greater than *1.0* since ($\chi_e > 0$). Values of ε_r are listed in Table 3.1 for some common materials at room temperature (*20 °C*).

Table 3.1: Dielectric permittivities for some common materials at *20 °C*, (Ulaby, 2005)

Material	Dielectric Permittivity (ε_r)
Vacuum	1.0
Air (at sea level)	1.0006
Teflon	2.1
Wood (dry)	1.5 – 4.0
paper	2.0 - 4.0
Rubber	2.2- 4.1
Mica	5.4- 6.0
Glass	4.5- 10.0
Quartz	3.8- 5.0
Distilled water	81.0
Dry soil	2.5-3.5

3.3 Capacitance Sensors

In general, to sense is to respond to a stimulus. A capacitor can function as a sensor if a stimulus changes, for example, the capacitor's geometry, usually the spacing between its conductive elements, or the dielectric properties of the insulating material situated between them. There are many applications for the capacitance sensors including a proximity sensing for personal detection when machine operator is too close, a light switch which can be built into a light switch for residential use, or vehicle detection for traffic lights uses. The idea of the capacitance sensor can be simply illustrated by the fluid gauge, Figure 3.3, (Ulaby, 2005).

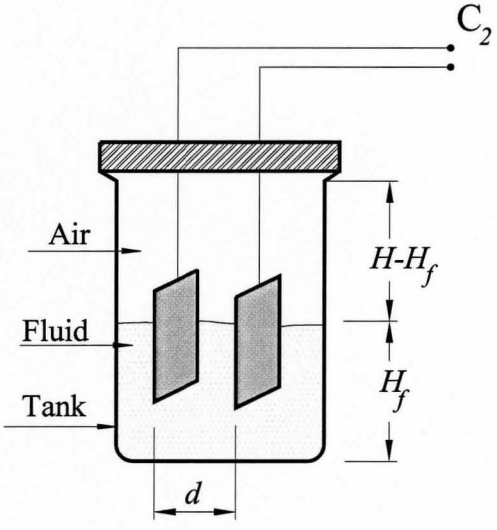

Figure 3.3: Capacitance sensor to measure the fluid level

The fluid gauge is a capacitor that consists of two parallel plates located inside a tank to determine the fluid height. The capacitance between the plates is directly

proportional to the permittivity of the materials between them. Hence, the capacitance, C, is given by:

$$C_2 = C_f + Ca = \varepsilon_f \frac{sH_f}{d} + \varepsilon_a \frac{(H - H_f)}{d} \tag{3.15}$$

where s is the electrode plate width, d is the spacing between electrodes, and ε_f and ε_a are the dielectric permittivities of the fluid and air, respectively. The above equation might be written as:

$$C_2 = kH_f + C_o \tag{3.16}$$

where the constant $k = (\varepsilon_f - \varepsilon_a)s / d$ and C_o is the capacitance of the tank when totally empty. Therefore, the fluid height, H_f, can be determined by measuring C_2 using the above linear equation, Eq. (3.16).

3.4 Analytical Modelling of Coplanar Capacitance Sensor (CCS)

In order to optimize the sensor design, it is important to obtain a theoretical formulation, which represents the output capacitance as a function of the sensor geometrical parameters and the material properties. In this section, an analytical model for the CCS on layered dielectric substrates will be presented.

3.4.1 CCS Over a Single Substrate Layer

The proposed CCS can be modeled as two adjacent electrodes of width, s, with spacing, $2g$, over a single layer of a material of dielectric permittivity, ε_1, and thickness,

h_1, as shown in Figure 3.4. Since the length of electrodes l is longer than its width, s, it can be assumed that there is no variation in the electric field distribution in the third dimension of the electrode length. Therefore, the three-dimensional field can be simplified to a two-dimensional field.

Considerable research efforts focused on developing an analytical framework to predict the capacitance per unit length between nearby conductors. Conformal mapping technique, [(Schinzinger and Laura 1991), (Vendik et al. 1999), (Gevorgian and Berg 2001)], provides a good approximation to calculate the capacitance between two strips of infinitely long conductors as it allows transforming the field for the planar structure to a parallel-plate capacitor field.

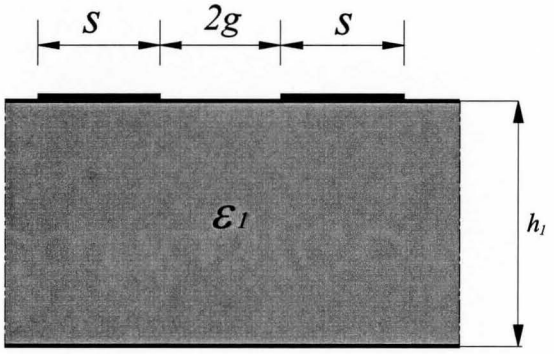

Figure 3.4: CCS over a single substrate layer

Figure 3.5 illustrates the sequence of the conformal mapping transformation. The transformation is carried out in two steps. In the first step, the semi-infinite right hand side of the dielectric material, as shown in Figure 3.5-(a), is mapped onto a lower part of

T-plane, as shown in Figure. 3.5-(b), using the following transformation proposed by (Gevorgian and Berg 2001):

$$T(z) = \cosh^2(\pi z / 2h) \tag{3.17}$$

In the *T-plane*, the mapping results are as following: $t_1=1, t_2 = \cosh^2(\pi g / 2h)$; $t_3 = \cosh^2(\pi(s+g)/2h)$; $t_4 = t_5 = \infty$; $t_6 = 0$.

In the second step, the lower part of the *T-plane* is mapped onto a rectangle in the *W-plane*, as shown in Figure 3.5-(c) using the Schwartz-Chistoffel transformation, (Gevorgian and Berg 2001) as follows:

$$W(t) = \int_{t_3}^{t} \frac{dt}{\sqrt{(t-t_1)(t-t_2)(t-t_3)(t-t_6)}} \tag{3.18}$$

For $t_1 > t_3 > t_2 > t_6$, the solution for Eq. (3.18) is:

$$W(t) = K(k) + jK(k') \tag{3.19}$$

where $K(k)$ and $K(k')$ are the complete elliptic integral of first kind functions which given by:

$$K(k) = \int_{0}^{1} \frac{dt}{\sqrt{(1-t^2)(1-k^2t^2)}} \tag{3.20}$$

with k and k' moduli given as:

$$k = \frac{\tanh(\frac{\pi g}{2h})}{\tanh(\frac{\pi(s+g)}{2h})} \tag{3.21}$$

$$k' = \sqrt{1-k^2} \tag{3.22}$$

In the *W-plane*, the mapping results are as following: $w_1 = K(k) + jK(k')$, $w_2 = jK(k')$, $w_3 = 0$, and $w_6 = K(k)$. Therefore, the total partial capacitance between the two strips considering identical series-connected capacitor due to the left-hand side in Figure 3.5-(a) is:

$$C_s = \varepsilon_o(\varepsilon_1 - 1)\frac{1}{2}\frac{K(k')}{K(k)} \tag{3.23}$$

The partial capacitance, C_a, due to air from (3.23) for $h = \infty$ considering air above and below the adjacent electrodes is given as:

$$C_a = \varepsilon_o \frac{K(k_o')}{K(k_o)} \tag{3.24}$$

where the elliptic integral moduli are given as: $k_o = \frac{g}{s+g}$, and $k_o' = \sqrt{1-k_o^2}$.

The total capacitance, C, for a single layer substrate of dielectric permittivity, ε_1, is $C = C_s + C_a$, and can be written as:

$$C = \varepsilon_o \varepsilon_{eff_1} \frac{K(k_o')}{K(k_o)} \tag{3.25}$$

where ε_{eff_1} is the effective dielectric permittivity for a single substrate layer and is defined as:

$$\varepsilon_{eff\,1} = 1 + (\varepsilon_1 - 1)\, q_1 \tag{3.26}$$

where q_1 is the *filling factor* for a single layer and may be written as:

$$q_1 = \frac{1}{2}\frac{K(k')K(k_o)}{K(k)K(k_o')} \tag{3.27}$$

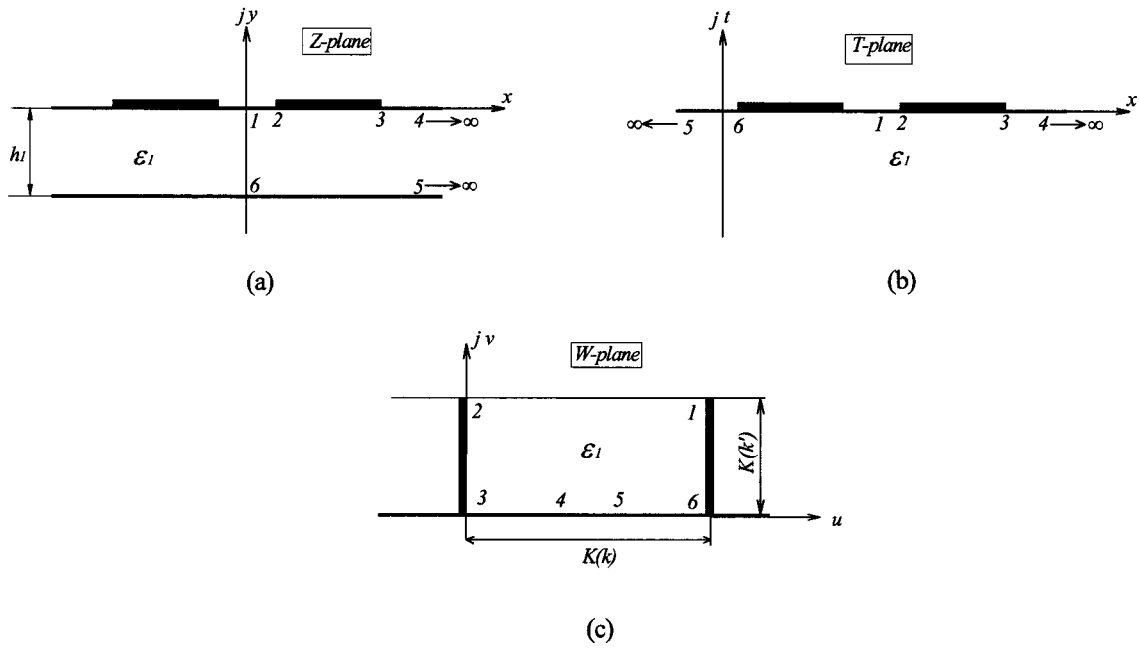

Figure 3.5: The sequence of the conformal mapping transformations, (a) the original *Z-plane*, (b) the transformed *T-plane*, and (c) The final transformed *W-plane*

3.4.2 CCS Over Two Substrate Layers

The pervious analysis of modelling the CCS over a single dielectric layer can be expanded to model the CCS over a two substrate layers with depths from the upper surface of h_1 and h_2, and dielectric permittivities ε_1 and ε_2 respectively, as shown in Figure 3.6-(a). Figure 3.6-(b) shows the equivalent circuit for the CCS in which the total capacitance is computed based on the *partial capacitance technique*, (Carlsson and Gevorgian 1999), as the sum of three capacitors, each of a single dielectric layer connected together in parallel where the total capacitance is expressed as:

$$C = C_0 + C_1 + C_2 \tag{3.28}$$

The equivalent dielectric permittivities of the single layer in each capacitor are 1.0, $\varepsilon_1 - 1$, and $\varepsilon_2 - \varepsilon_1$ as shown in Figure 3.6-(c).

The total capacitance per unit length for the two layers substrate can be easily computed as:

$$C = \varepsilon_o \varepsilon_{eff\,2} \frac{K(k_o')}{K(k_o)} \tag{3.29}$$

and the filling factor is written as:

$$\varepsilon_{eff\,2} = 1 + (\varepsilon_1 - 1)q_1 + (\varepsilon_2 - \varepsilon_1)q_2 \tag{3.30}$$

where

$$q_i = \frac{1}{2} \frac{K(k_i')K(k_o)}{K(k_i)K(k_o')};\ i=1,\ 2 \tag{3.31}$$

It can be noticed that the final form of the capacitance for CCS is analogue to the equation of the parallel-plate capacitor, Eq. (3.14). The capacitance is proportional to the relative permittivity of the material, electrode area of the transformed parallel-plate capacitor, and the reverse of the separation distance of the transformed parallel-plate capacitor. The above analysis may be used to estimate the capacitance of such a capacitor by substituting the permittivity of the free space and the dielectric permittivities of the two layers as well as the dimensions of geometrical sensor parameters.

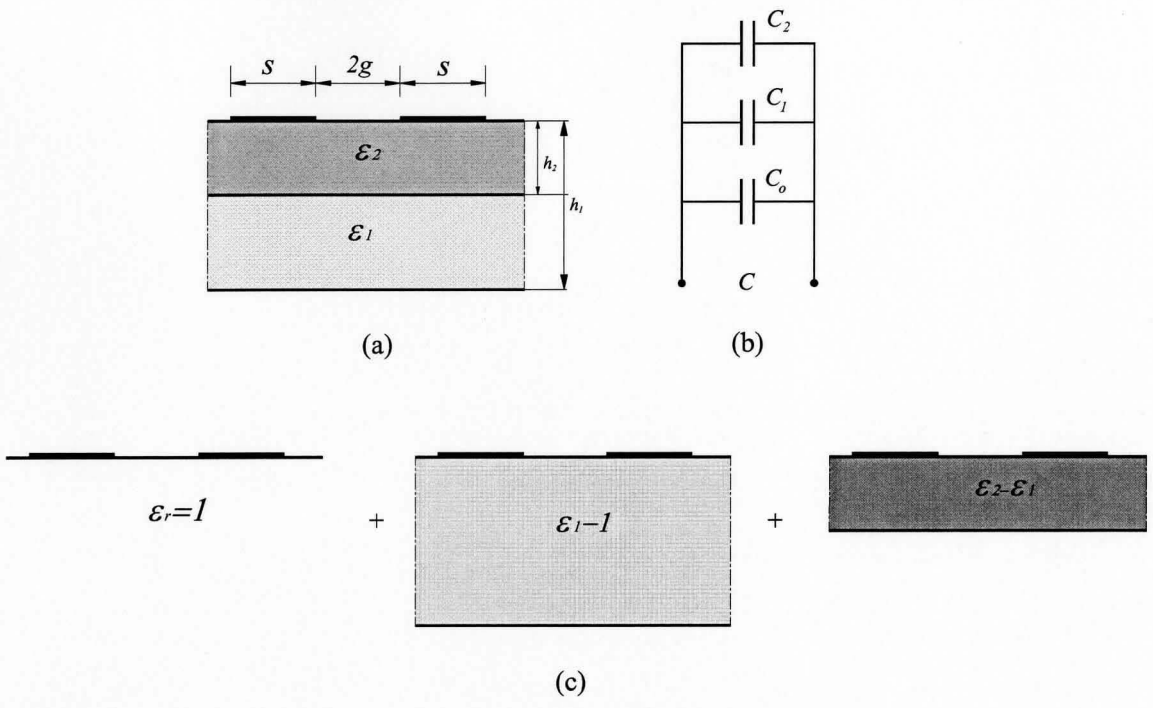

Figure 3.6: CCS model, (a) a CCS over a layered media substrate, (b) equivalent circuit of the CCS, and (c) the partial capacitance technique

3.4.3 Interdigital Capacitance Sensors (IDCS)

Interdigital Capacitance Sensors (IDCS) or Multi-electrode capacitance sensors are composed of two comb-like finger electrodes that are alternately arranged and connected to two main terminals, as shown in Figure 3.7. The IDCS provides the feasibility to control the strength of output signals by changing the number of fingers, *N*, width of the finger plates, *s*, and the finger spacing, *2g*, (Mamishev et al. 2004). The wave length, λ, of the IDCS is defined as the distance between two electrodes of the same kind.

Assuming no capacitance contributions from nonadjacent finger plates, the capacitance per unit length of the interdigital capacitor is the sum of the capacitances of *unit* capacitors (a pair of two adjacent electrodes), (Wang et al. 2003), in other word:

$$C_T = \sum_{i=1}^{N-1} C_i \tag{3.32}$$

where C_T is the total capacitance of the interdigital capacitor, C_i is the capacitance between a pair of electrodes per unit length, and N is the number of fingers.

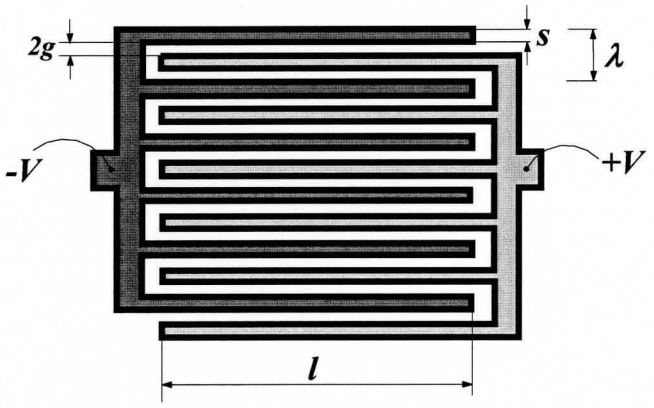

Figure 3.7: Interdigital capacitance sensor (IDCS)

3.5 Finite Element Modelling (FEM) of CCS and IDCS

In addition to their applications for mechanical and structural problems, such as stress/strain calculations and dynamic analysis, Finite Element Modelling (FEM) can also be applied to solve electric or magnetic field problems. This section discusses modelling of CCS and IDCS using commercially available FEM code.

3.5.1 FEM Formulation

Due to the general uniformity of the electric field along one direction compared with the other dimensions of the proposed coplanar sensor, and in order to be consistent with the analytical model explained above, where ($l > s$), a *2D* finite element simulation

was selected for modelling the sensing system. Unlike *3D* modelling, the *2D* simulation neglects the fringe-field effects at the outer edges of the electrodes. However, these effects resulted in minor differences between the predicted and measured capacitance results as will be shown later.

The *2D* models considered in this study were constructed using a commercially available finite element modelling (FEM) package, (*Maxwell 2D* 2003). The problem space was divided into triangular elements. In the region of ideal dielectrics and space charges, the electrostatic potential, $\phi(x,y)$ is determined by Poission's equation:

$$\nabla \cdot (\varepsilon_r \varepsilon_o \nabla \phi(x,y)) = -\rho \tag{3.33}$$

where ρ is the charge density.

All the elements of the region have the same value of ε_r and ρ. The FEM analysis yields values of the electrostatic potential, $\phi(x,y)$, at the nodes of the solution space. Then, the electric field, *E(x, y)*, and the electric flux density, *D(x, y)*, are computed, respectively, from the following equations:

$$E = -\nabla \phi \tag{3.34}$$

and

$$D = \varepsilon_r \varepsilon_o E \tag{3.35}$$

The electric field energy, *U*, can be expressed in a volume integral form and calculated using:

$$U = \frac{1}{2}\int_V D \cdot E dv \tag{3.36}$$

Because the capacitance, C, represents the amount of energy stored in the electric field, C can be computed using:

$$C = \frac{2U}{V^2} \tag{3.37}$$

where V is the voltage across the dielectric.

3.5.2 Electrostatic Analyses using *Ansoft Maxwell 2D* Code

Ansoft Maxwell 2D FEM code is a useful tool for solving field problems in electric, magnetic and electromechanical systems. In this study, *Maxwell 2D* was used to model the capacitance sensors and to simulate the electric field throughout the material layers. In addition, FEM will be used to verify the analytical results and optimize the sensor design. As many other FEM codes, several steps need to be followed for proper modelling using *Maxwell 2D* code; these steps can be summarized as:

1 - Choosing the field solver

FEM code allows choosing different solvers to simulate the electric, magnetic, and thermal fields. In this study, the electrostatic field solver will be used to compute electric fields arising from a potential difference and charge distribution across the CCS and IDCS electrodes. The solution will also be used to model field-stored energy, capacitance, potential distribution and electric flux linkage. In addition, other quantities derived from the basic electric field solutions can be analyzed. The electrostatic field solver only computes the electric field from static charge distributions and, therefore, the solver assumes no current flowing in the materials.

2 - Drawing the model

In this step, a solid model of the geometry is constructed. *Maxwell 2D modeler* is used to create the geometric models by drawing different model objects. Closed paths represent a solid material and refer to them as *objects*. Objects are assigned different names when created. FEM code has the option of object grouping; this may be useful to model IDCS, where the terminations of one conductor are drawn in the cross section as separate objects, they can be grouped to represent one physical conductor. Figures 3.8 and 3.9 show the geometric model for CCS and IDCS over two layers media.

3 - Assigning material properties

The next step in constructing the model is to define the materials. The code has a material database consisting of pre-defined materials that may be assigned to individual objects in the model. New material characteristics, however, can be added by defining the dielectric parameters for such materials. The electrodes are assigned as perfect conductors. The model layers are assigned different dielectric properties. The space surrounding the model (background) is assigned the vacuum properties.

4 - Setting up potential values

In the step, the sources of voltage and boundary conditions are defined, which allow modelling the behavior of the electric field inside surfaces or edges of the problem space. The background is treated as *balloon boundary*, which effectively isolates the model from other voltage or charge sources. One electrode is set as a driving electrode

with a certain voltage value, and the other electrode is set as a sensing electrode with a zero voltage, so that the potential difference between the electrodes is capable of generating an electric field throughout the material layers, and capacitance can be computed between the electrodes.

5 - Declaring executive parameters

This step is to define the objects of the problem between which the capacitance or any other quantities will be computed during the solution. Both the driving and sensing electrodes are selected to be included in the solution to obtain the capacitance matrix.

6 - Setting up the solution

After specifying the solver type, material attributes, boundaries, and potential sources, the solution options and finite element mesh must be assigned. The code divides the problem region into triangular elements and represents the field in each element with a separate polynomial. FEM code only computes the potential and electric field value at the nodes of elements. To obtain the values at other points inside the elements, the field is interpolated from the nodal values. Therefore, the placement and number of elements of the finite element mesh need to be optimized. If the mesh elements are too large, the field inside the elements cannot be interpolated accurately from the nodal values. In general, the optimal mesh is one that contains enough number of elements to accurately represent a field solution but not too many that the available computing resources are overwhelmed.

The code automatically performs the initial mesh generation and refinements through adaptive refinement analysis to optimize the number of elements as well as the placement of new elements. Generally, the initial generated mesh is a relatively coarse and is rarely the optimal mesh. Adaptive analysis is a cycle of "*solving - error analysis – refinements*" that helps the finite element mesh to be iteratively refined in areas with the highest error. The FEM code stops the adaptive cycle as soon as one of the specified maximum number of refinements or acceptable error percentage of field energy is satisfied. Optionally, mesh can be manually assigned in areas of interest by specifying the desired total number of elements of the problem region or the number of elements per objects. Figure 3.10 shows the mesh generated by the code for the CCS model with a maximum number of adaptive passes set as *25* and a maximum percent error of solution as *0.01 %*. The adaptive analysis stopped after *18* passes with a number of elements of *8,841*. It can be see in Figure 3.10 that the increased of elements was in the area of high field intensity, especially at the corner of the sensor electrodes. Figure 3.11 shows the mesh generated by the FEM code for the IDCS model with a number of elements of *15,767* and the analysis stopped after *15* passes.

7 – Solving

During this process, the solution can be monitored to verify its convergence. FEM code, in this step, displays the adaptive passes and other computation processes such as energy stored and capacitance calculations.

8 – Post processing

After obtaining the solutions for the problem, the post processor becomes active. The post processor allows for plotting and analyzing field and potential solutions. Figures 3.12 and 3.13 show a sample output of the FEM for the CCS and IDCS displaying the electric field distribution and the equipotential lines. As shown in Figures 3.12 and 3.13, the electric field is represented by a set of curves, *field lines*, aligned along the local field direction with spacing inversely proportional to the field strength.

The pervious steps of FEM are summarized in the flow chart, Figure 3.14, *Maxwell 2D Manual*

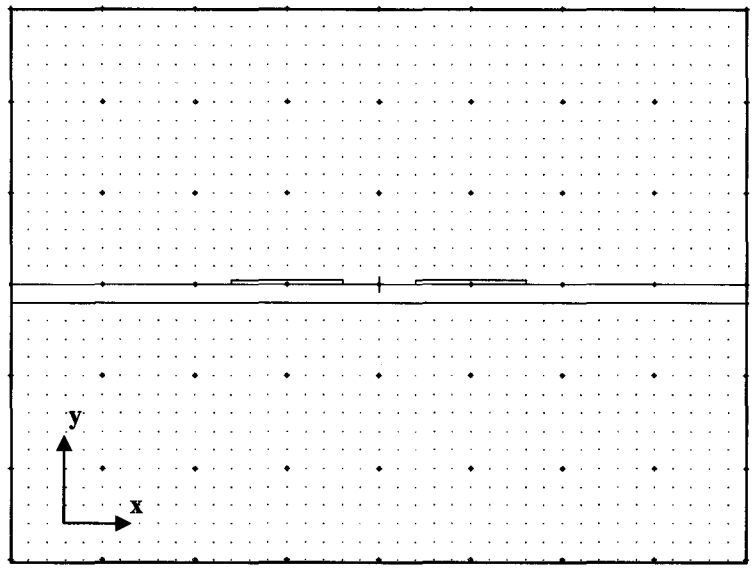

Figure 3.8: The geometric model for CCS

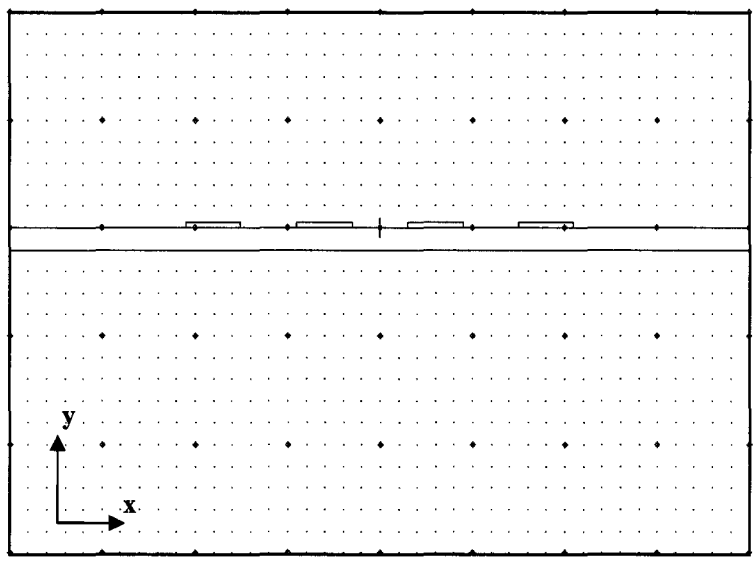

Figure 3.9: The geometric model for IDCS

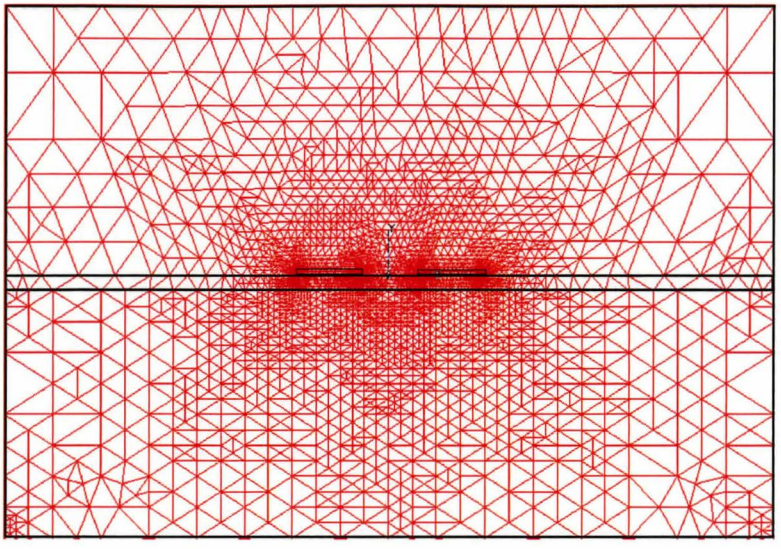

Figure 3.10: The mesh generated by FEM code for CCS

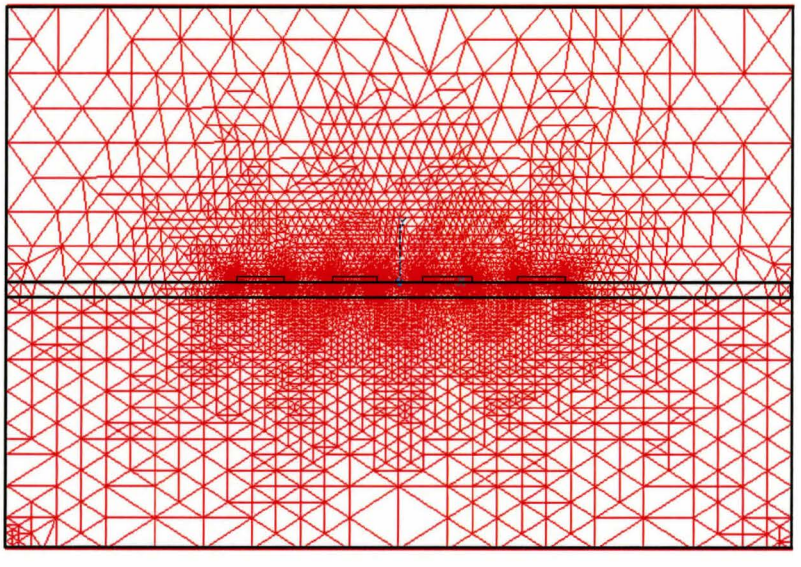

Figure 3.11: The mesh generated by FEM code for IDCS

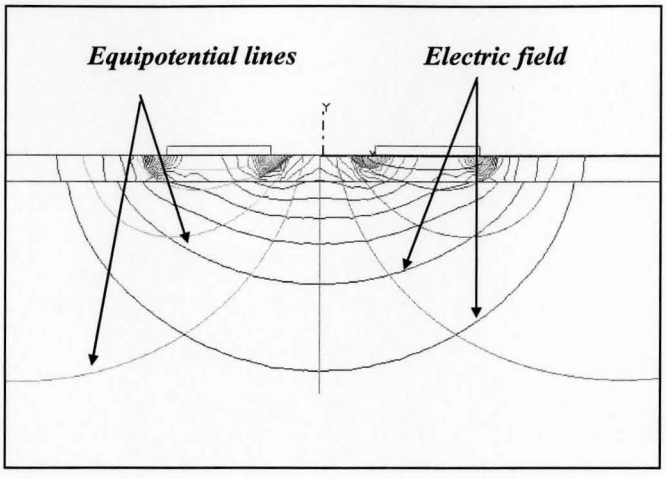

Figure 3.12: The electric field distribution and equipotnetial lines for CCS

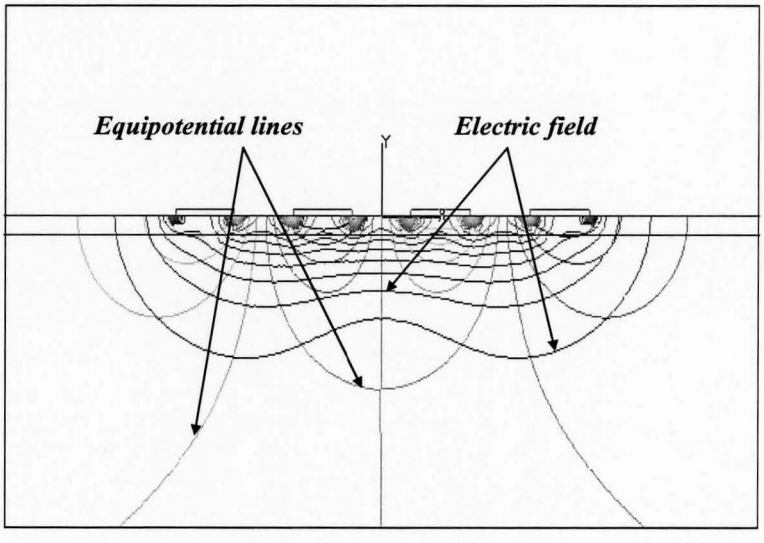

Figure 3.13: The electric field distribution and equipotnetial lines for IDCS

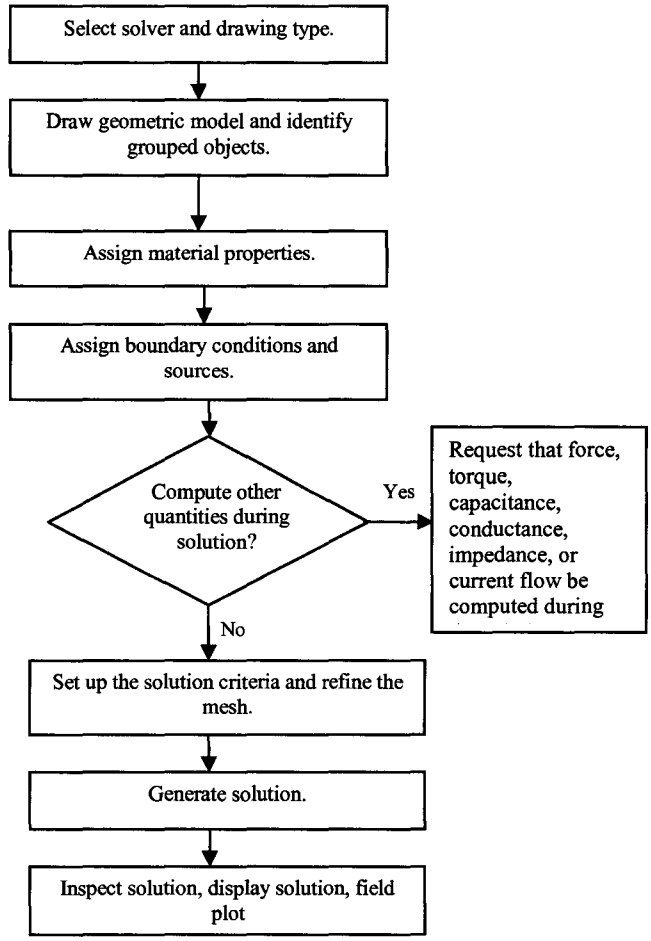

Figure 3.14: The flow-chart for the FEM, *Maxwell 2D Manual*

3.6 Conclusions

This chapter presented the theoretical background and electrostatic principles behind the developing the capacitance technique. The simple parallel-plate capacitor was used to study the effect of the dielectric material on the electric field distribution, potential, and the resulting capacitance. The analytical model for the CCS and IDCS based on conformal mapping technique was presented. Using the analytical model, the capacitance signals can be estimated for specific sensor geometrical parameters and the dielectric properties of the substrate layers. A *2D* FEM for the proposed CCS and IDCS was also presented using *Ansoft Maxwell 2D* code. FEM code estimates the expected response of the capacitance sensor given all information about the material under test and the sensor parameters. In addition, FEM code was used to plot the electric field distribution throughout the material under test. Proper modelling using *Maxwell 2D* included several steps of building the geometrical model, assigning the materials, defining the boundary conditions, choosing the model mesh, and solving the FEM. Modelling the capacitance sensors is an important step towards capacitance sensor design and optimization as will be discussed in the next chapter.

Chapter 4: Capacitance Sensor Design and Optimization

4.1 Introduction

This chapter will discuss the design and optimization of the proposed capacitance sensors. The signal strength and penetration depth of the electric field through the material layers are considered the most important factors governing the sensor design. The analysis will be performed for all geometrical parameters, which may have considerable influences on the sensor outputs. In addition, design charts will be developed to facilitate the selection of capacitance sensor configurations for different applications. This chapter will also present the effect of the defect depth, height, and type on the output signal responses. Towards the end of the chapter, the determination of the defect location using the capacitance sensors will be demonstrated. With proper sensor design, differences in dielectric signatures of materials between defected and sound zones should result in a significant change of the sensor output signals.

4.2 Sensor Geometrical Parameters

For an accurate detection of damages in composites, the capacitance sensor geometrical parameters must be optimized. This section focuses on evaluating different sensor geometrical parameters on signal strength and penetration depth of the electric field through the material layers. This will form the base of capacitance sensor design and optimization for deferent levels and types of damage detection.

4.2.1 Signal Strength

The signal strength is an important aspect to be considered in any sensor designs; as high signal strength leads to a high Signal-to-Noise Ratio (SNR) which, in turn, leads to more stable and robust results. The sensor geometry has the largest influence on the signal strength of the capacitance sensors.

The *s/g* ratio is an important parameter in the sensor design, since that the resulting capacitance depends on the ratio *s/g* rather than on the absolute values of *s* and *g*. Figure 4.1 shows the change of the predicted capacitance using Eq. (3.29) and the FEM simulations for different *s/g* values. It is convenient to express the capacitance, *C*, in terms of a dimensionless parameter, *C** as:

$$C^* = C / \varepsilon_{eff} \varepsilon_o l \tag{4.1}$$

where *C* is the actual capacitance in *(F)*, *l* is the length of the electrode in *(m)*, ε_{eff} is the effective dielectric permittivity for the substrate layers, and ε_o is the permittivity of free space in *(F/m)*. From Figure 4.1, it can be seen that the capacitance increases in proportion to the *s/g* ratio. It can also be inferred that there is a good agreement between the analytical model and FEM predicted results.

Figure 4.2-(a) shows the effect of electrode spacing, *g*, and electrode width, *s*, on the predicted sensor capacitance. The electrode spacing has a strong influence on the capacitance signals, as the sensor with a narrow gap spacing yields higher signals than the sensor with a wider gap spacing. The capacitance increases proportionally with the electrode width, *s*. The data points can be fitted into a power function relationship

$[C\alpha(g)^{\beta}]$, where β is found to be equal to *-0.275*, as shown in Figure 4.2-(b) for specific values of *s*.

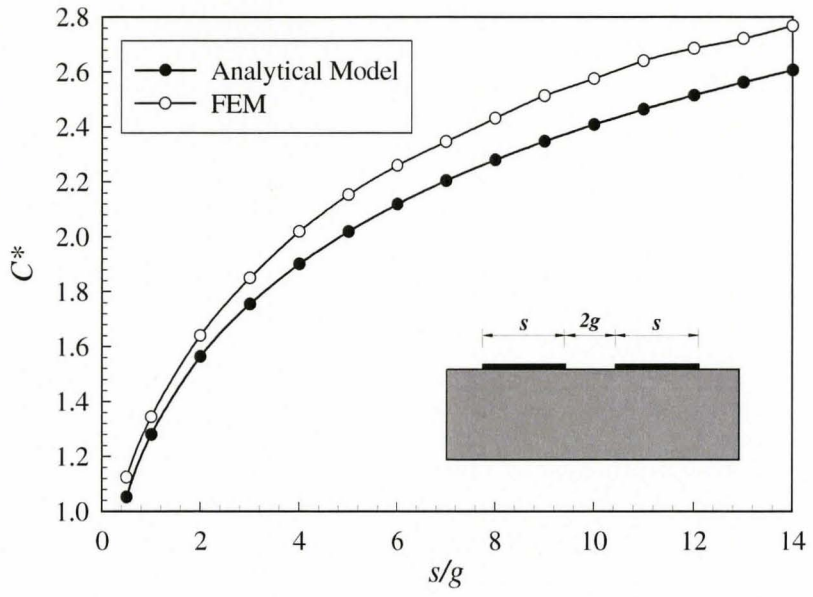

Figure 4.1: Normalized capacitance versus (*s/g*) ratio

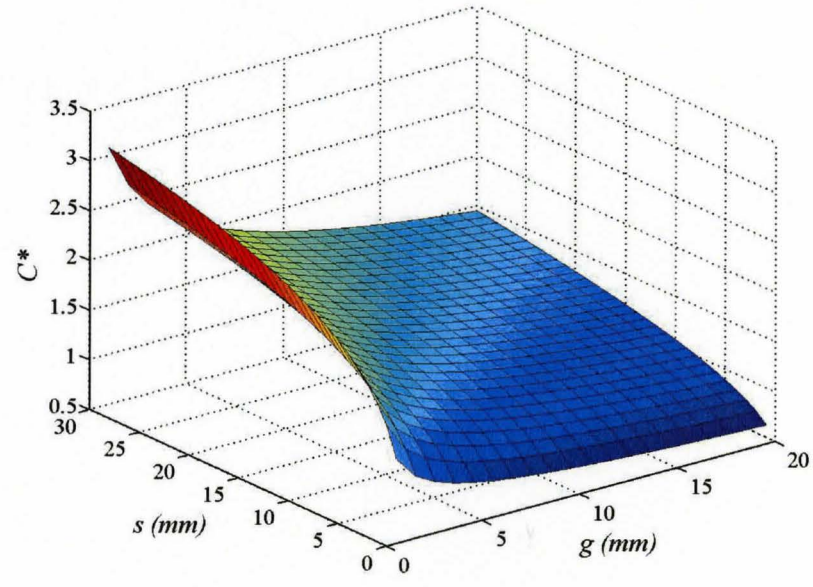

(a) in the *s-g* space

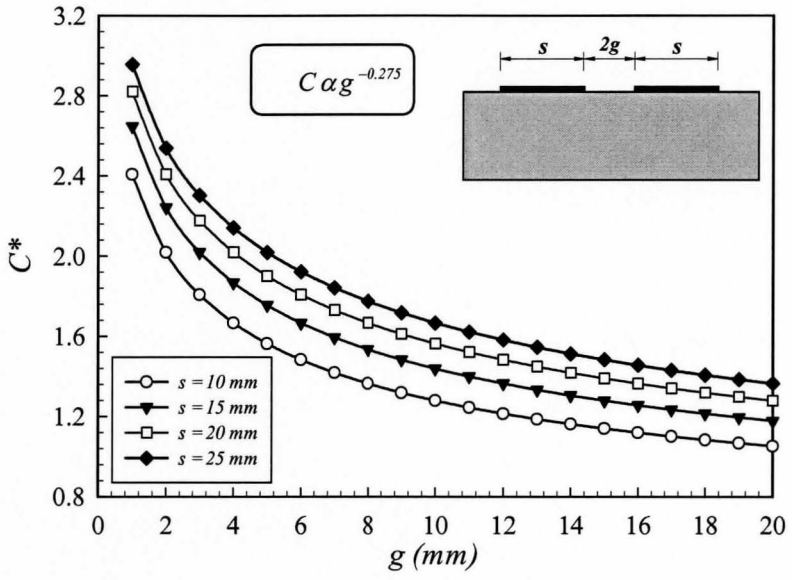

(b) for constant s values

Figure 4.2: The normalized capacitance versus s and g

4.2.2 Sensor Penetration Depth

Another important factor in sensor design is the sensor penetration depth, T, which indicates how deep the electric field penetrates into a test specimen or the material thickness, as shown Figure 4.3. It should be noted that the electric field strength decays exponentially along the material thickness. Therefore, the dielectric permittivities of materials nearest to the electrodes have greater influence on the sensor signals compared to dielectric permittivities of materials deep in the test specimen. It was expected that, similar to fringing electric field sensors (Li et al. 2004), the penetration depth, T, of the developed capacitance sensor would depend on the sensor geometry and be proportional

to the distance between the centrelines of the two coplanar electrodes. Several FEM simulations were performed for different electrode widths, *s*, and electrode spacing, *g*, to estimate the penetration depth, *T*, of the capacitance sensors, as shown in Figure 4.4-(a).

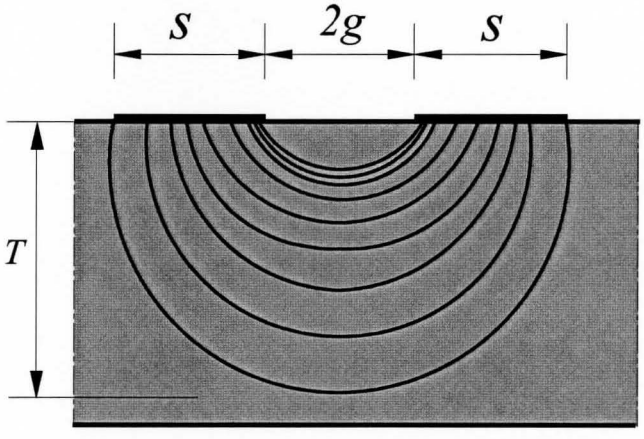

Figure 4.3: The penetration depth of the electric field through the material layer

The FEM data can be fitted into a linear relationship, Figure 4.4-(a), between the penetration depth, *T*, and sensor geometrical parameters, *s* and *g*, with average correlation factors equals to *0.98*. This relationship can be expressed as:

$$T = ng + T_o \tag{4.2}$$

where T is the penetration depth in *mm*, g is the electrode spacing in *mm*, n is the line slope, and T_o is the offset constant. The slope n is found to be equal to *1.35*, and T_o to be equal to *0.65s*, where s is the electrode width in *mm*. Therefore, the Eq. (4.2) can be rewritten as:

$$T=1.35g+0.65s \tag{4.3}$$

Figure 4.4 presents that sensors with wide electrodes and widely spaced are capable of penetrating deeper in the materials further away from their surfaces than the sensor with narrow electrodes and closely spaced.

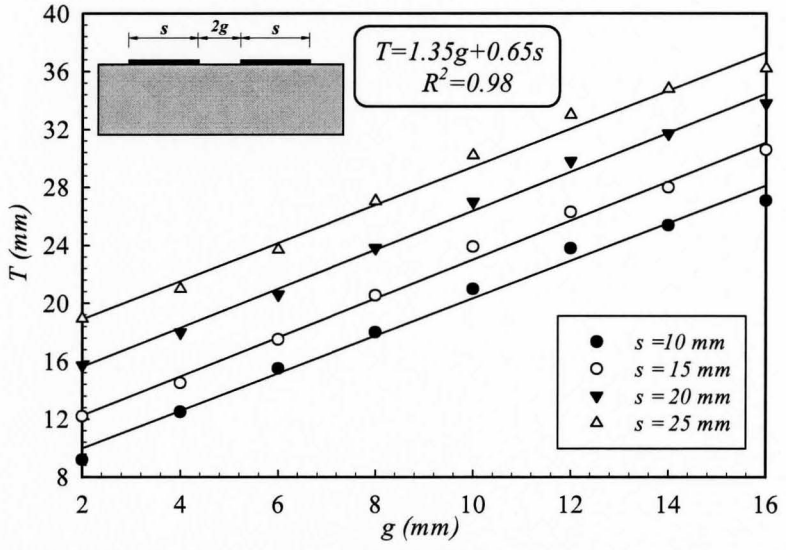

(a) constant *s* values

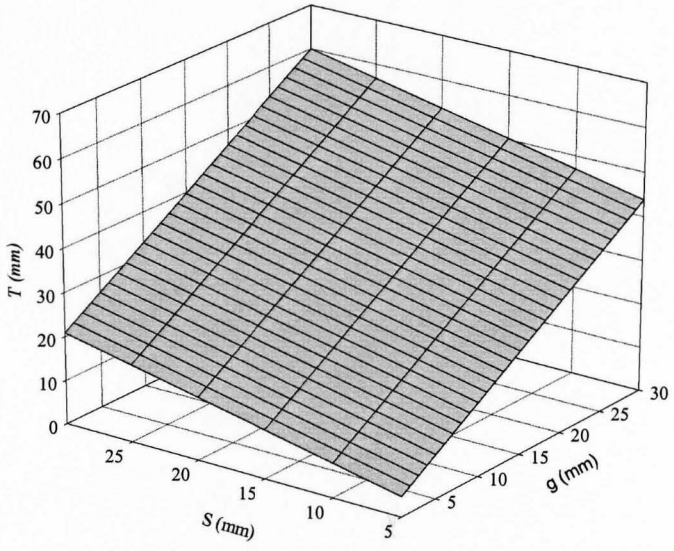

(b) in the *s*-*g* space

Figure 4.4: The penetration depth as a function of the sensor geometry

4.3 Sensor Design Charts and Optimization

This section introduces design charts for capacitance sensors, which assist the selection of the sensor optimal configuration, Figures 4.5-(a), and 4.5-(b). These charts provide the normalized capacitance, C^* and the penetration depth, T, for any couple of electrode spacing, g, and electrode width, s, forming a CCS. These curves can also be used for IDCS, as the design of IDCS will be based on the design and optimization of the unit coplanar capacitor.

Sensor design is an optimization process, where several factors have to be considered simultaneously. The major goals of sensor design are to achieve high signal strength, and sufficient penetration depth. For example, if it is desired to detect the defect as deep as *20 mm*, there are several configurations that can achieve that depth of penetration; this can be obtained, from Figure 4.5-(a), by the following designs of $(s \times g)$ as: (5×12), (10×10), (15×8) and (20×6). (20×6) appears to be the optimal design for the penetration depth, $T=20$ *mm*, since it gives the highest signal strength over the other sensor configurations.

The optimal design of the coplanar capacitance sensors is achieved by the proper selection of the sensor geometrical dimensions in order to get a sufficient field penetration depth, T, with the highest signal strength. This, in turn, depends on the specific application and desired detection depth.

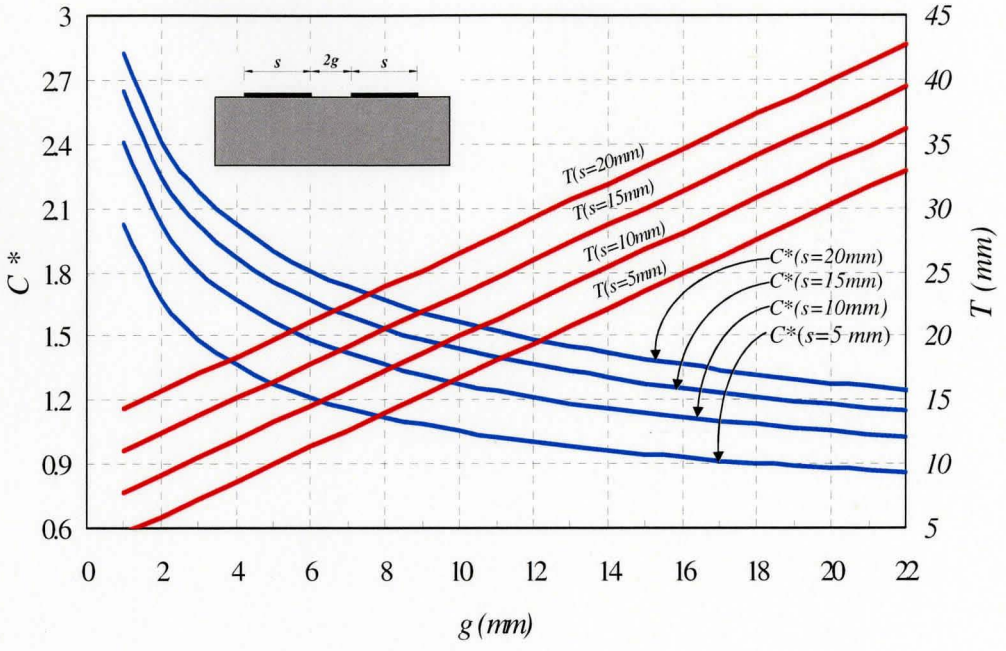

(a)

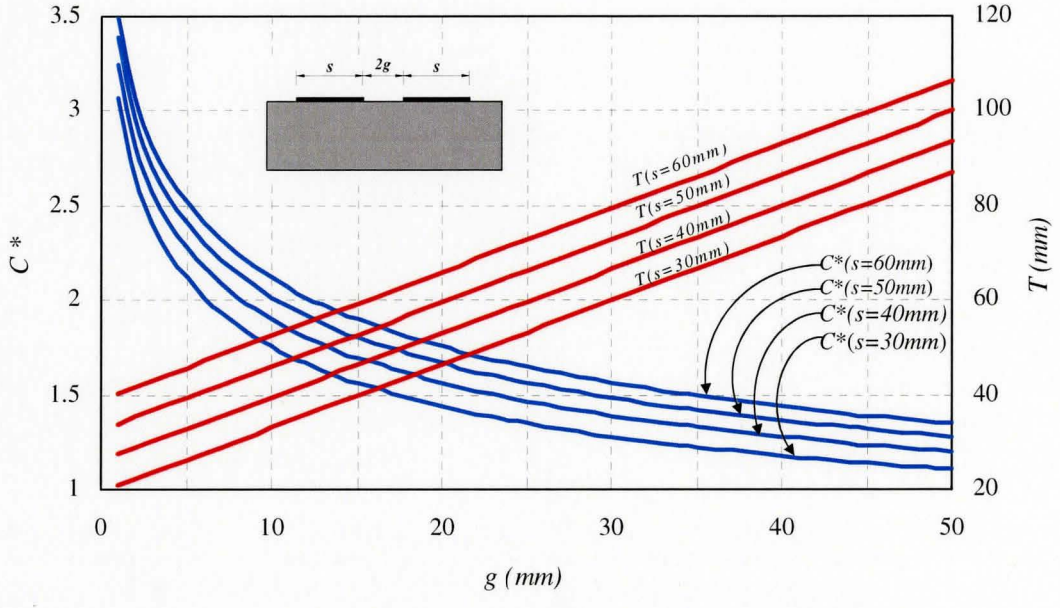

(b)

Figure 4.5: Design charts for capacitance sensors

4.4 Effect of Defect Geometry

In order to obtain on complete defect identifications, it is important to understand the effect of the defect variables on the capacitance signals. The variables that will be studied include the defect depth, height, and type.

4.4.1 Effect of Defect Depth

To show the effect of the defect depth on the capacitance signals, a pair of electrodes of width, $s = 20\ mm$ and spacing, $g = 10\ mm$, on an infinite height substrate of dielectric permittivity, $\varepsilon_s = 4.8$, is considered, as shown in Figure 4.6. The defect is at depth, z, from the upper surface of the substrate to its centre and height of $2\ mm$. Both air-filled defect of $\varepsilon_a = 1.0$ and water-filled defect of, $\varepsilon_w = 81$, are considered in this study. Figures 4.7 and 4.8 indicate the changes in the capacitance signals as a result of changes in air-filled and water-filled defect depth respectively. The normalized plots are created by normalizing each value of C (pF/m) by the minimum value of C as:

$$C_{\%increase} = \frac{C - C_{\min}}{C_{\min}} \times 100\% \tag{4.4}$$

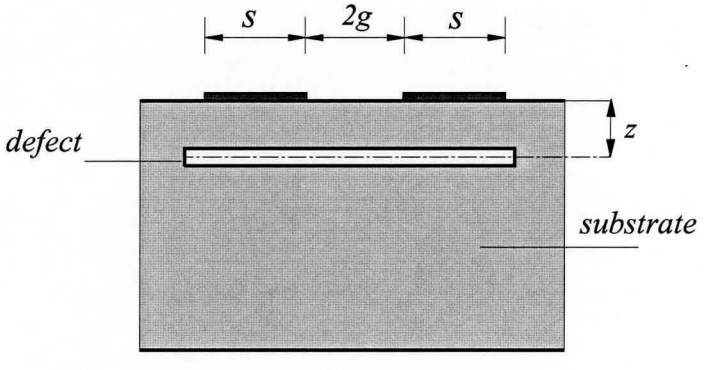

Figure 4.6: The effect of defect depth, z

Figure 4.7 shows that the changes in air-filled defect depth, *z*, has a significant effect on the normalized capacitance, as it increases with the increase of depth, *z*. The increase of the capacitance is because of the low value of the dielectric permittivity of air, $\varepsilon_a = 1.0$, compared to that of the substrate, $\varepsilon_s = 4.8$. The penetration depth of the above sensor configuration from Eq. (4.3) is *26.5 mm*. As expected, the sensor is most sensitive (steep slope) to changes in the air-filled location between *2* and *26 mm* and least sensitive to changes in the location more than *26 mm*. Therefore, the capacitance has a constant value for the depth, *z*, more than *26.5 mm*.

A water-filled defect is another type of defect that may contribute of structure degradation during its service life. Unlike the air-filled defect case, Figure 4.8 shows that capacitance decreases as the depth, *z*, increases. This is because that the dielectric permittivity of water, $\varepsilon_w = 81$, is higher than that of substrate, $\varepsilon_s = 4.8$. Another observation that may be taken for this case is the high sensitivity of the sensor to the water-filled depth defect as the capacitance decreases by *92%* when *z* changes from *2 mm* to *27 mm*. While in air-filled case, the capacitance increases by just *29%*, and this is also due to that the dielectric permittivity of water, $\varepsilon_w = 81$, is much higher than that of air, $\varepsilon_a = 1.0$.

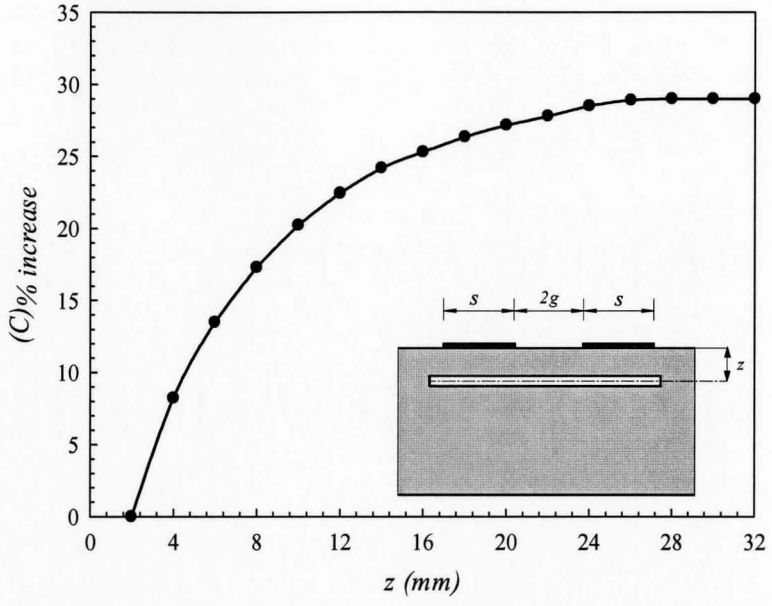

Figure 4.7: The capacitance versus air-filled defect depth, *z*

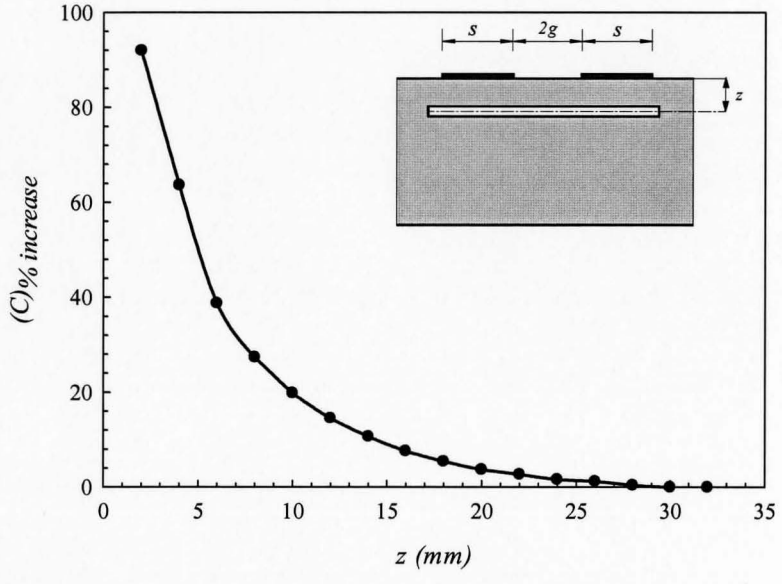

Figure 4.8: The capacitance versus water-filled defect depth, *z*

4.4.2 Effect of Defect Height

The same sensor configuration that discussed in section (4.4.1) is chosen to study the effect of the defect height on the output signals. The defect (air-filled or water-filled defect) is located at a distance, $t = 2\ mm$, measured from the upper surface of the substrate to the defect's upper edge. The distance, h, is measured from the upper surface of the substrate to the lower edge of the defect, as shown in Figure 4.9. The relationship between the defect depth, z, and the distances (h and t) is given by the following equation:

$$z = \frac{h+t}{2} \tag{4.5}$$

Figures 4.10 and 4.11 show the changes in the capacitance as a result of changes in air-filled and water-filled defect height respectively. Normalized plots are also created by normalizing each value of C (pF/m) by the minimum value of C.

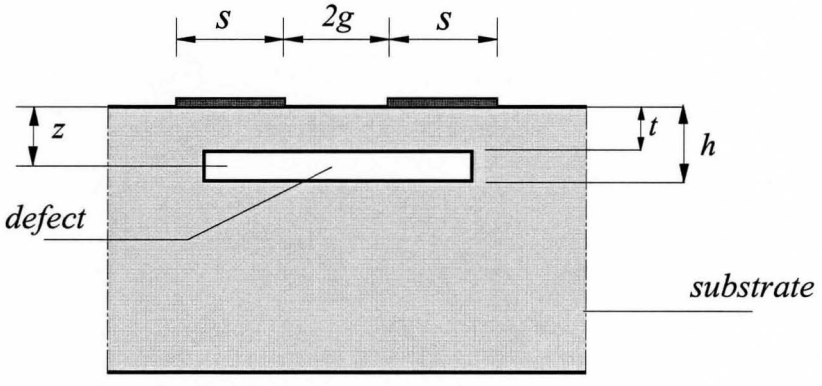

Figure 4.9: The effect of defect height

Figure 4.10 shows that the capacitance decreases with the increase of air-filled defect height, *h*. Again, the capacitance has a constant value for the height, *h*, more than the maximum penetration depth, ($T = 26.5\ mm$). Figure 4.11 shows that the height of the water-filled defect has a strong influence on the capacitance. It can be noticed that the capacitance increases as the height, *h*, increases. In addition, Figure 4.11 shows that the capacitance sensor has a high sensitivity to the height of water-filled defect, as it increases by *350 %* as a result of *27 mm* water-filled defect height, while the capacitance decreases by *90%* for the same air-filled defect height.

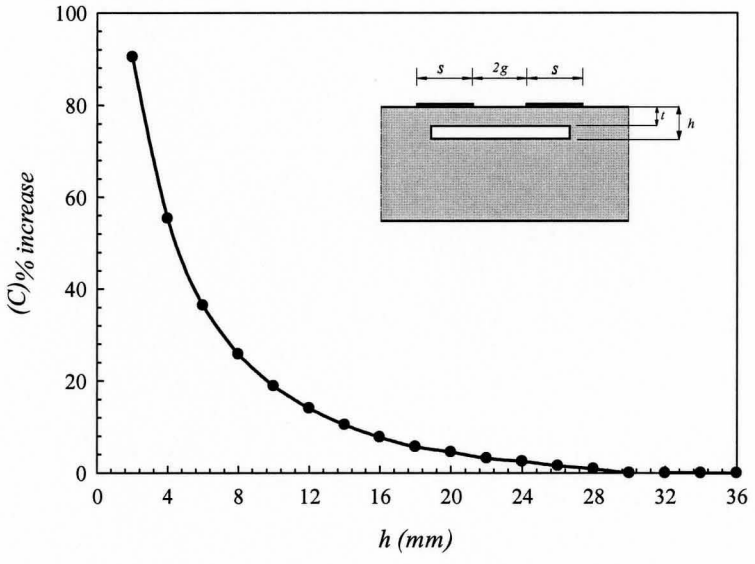

Figure 4.10: The capacitance versus air-filled defect height, *h*

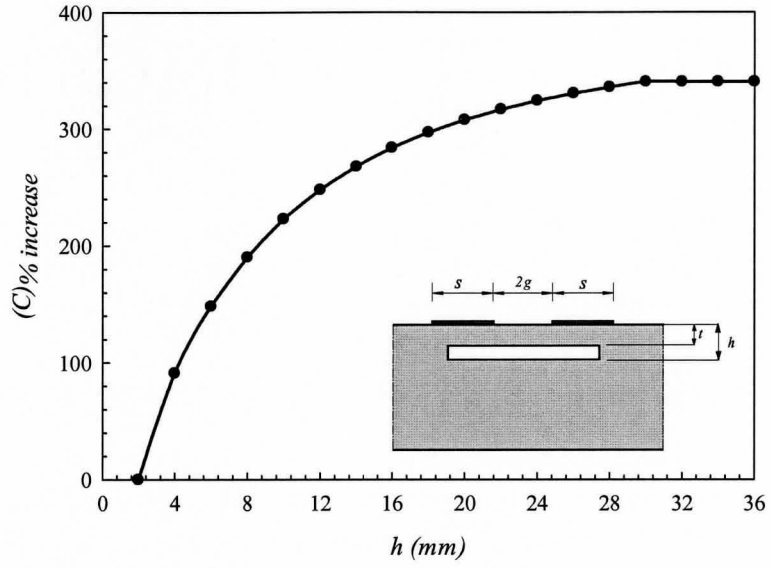

Figure 4.11: The capacitance versus water-filled defect height, *h*

4.5 Determination of Defect depth

Determining the defect depth is the one of the main goals for using the capacitance sensors. The location of the defect can be estimated by using different sensor configurations with the same (*s/g*) ratio. Sensors with the same (*s/g*) have equal measured capacitance values, as discussed in section (4.2.1), but with different maximum penetration depths, *T*, as shown in Figure 4.12. Supposing that the defect, air gap, with a dielectric permittivity of $\varepsilon_a = 1.0$, is in a certain depth, $z = 6.0\ mm$, in a substrate of dielectric permittivity, $\varepsilon_s = 4.8$. A set of sensors of $s/g = 2.0$ is chosen to determine the defect location.

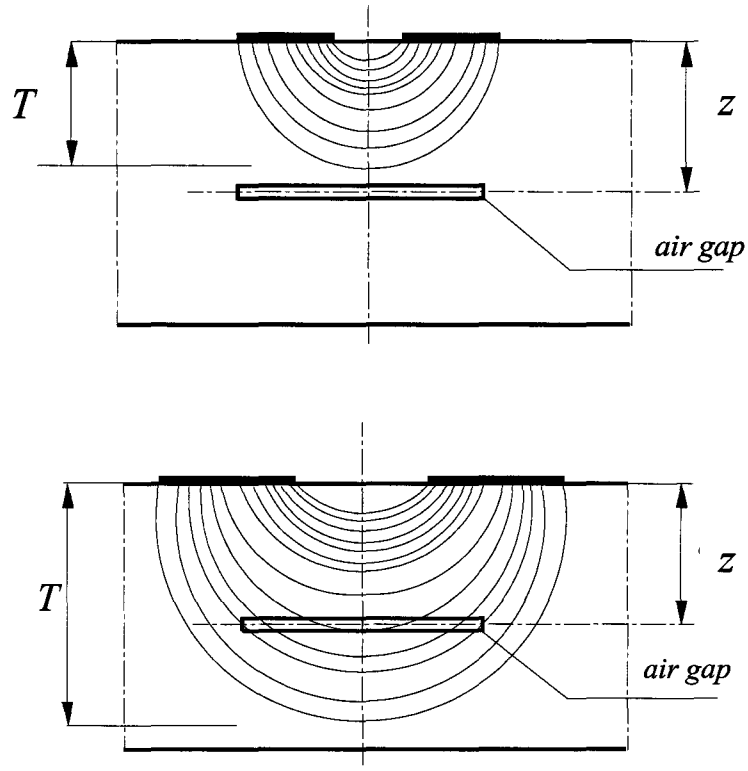

Figure 4.12: Capacitance sensors with same (*s/g*) and different *T*

Figure 4.13 shows that the capacitance has a constant value for sensors with penetration depth less than *z* (air gap location). The capacitance has lower values for sensors with penetration depths more than *z*, after *T =6 mm*. Therefore, the defect depth is the same as the sensor penetration depth when the measured capacitance starts to change for a set of coplanar electrodes with the same (*s/g*) ratio.

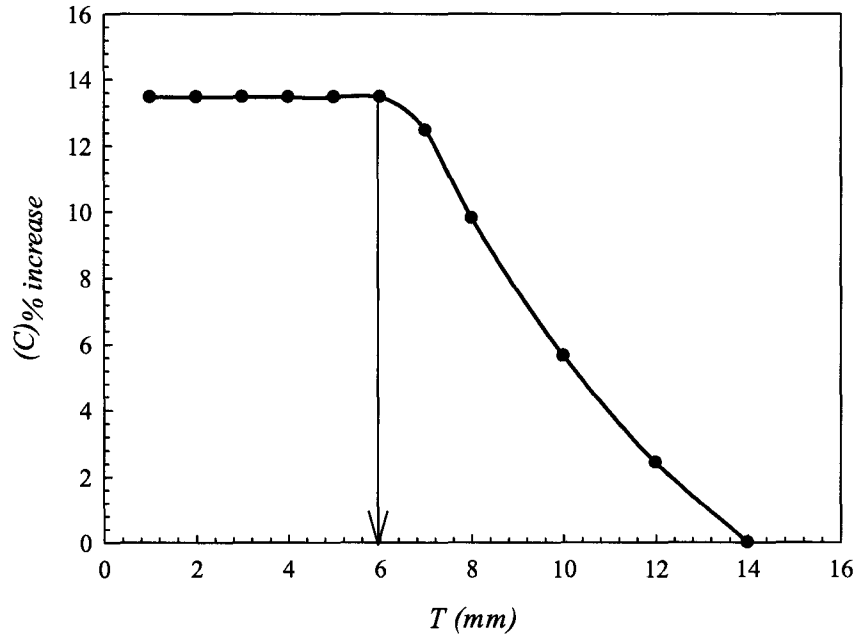

Figure 4.13: Defect depth determination

4.6 Conclusions

This chapter presents the principles of the capacitance senor design and optimization. The analytical modelling and FEM were used to study the effect of the sensor geometry parameters on the output signal and to optimize the sensor designs. The influence of the electrode width and electrode spacing on the signal strength and the penetration depth of the electric field through the material layers were evaluated. The effect of the defects on the sensor responses was theoretically presented by changing the defect depth, height and type. In addition, the determination of the defect location was demonstrated using a set of coplanar electrodes with equal (*s/g*) ratio.

The sensor geometry has the largest influence on signal strength, and sensor penetration depth. It was found that the increase of gap spacing between the electrodes increased the penetration depth of the electric field through the material layers but reduced the signal strength, while the increase of the electrode width increased both the penetration depth and signal strength. The major goals of sensor design are to achieve high signal strength, and sufficient penetration depth. The sensor design charts were developed to facilitate the selection of these parameters in order to obtain on the optimal designs of capacitance sensors. The capacitance sensor had good sensitivity to the defect depth, height and type. This study clearly demonstrated that dielectric signatures of different materials could be used for damage detection using capacitance sensors.

Chapter 5: Experimental Verifications

5.1 Introduction

This chapter will present the experimental results obtained from different capacitance sensor configurations to detect damages in different composite specimens. The specimens will include concrete and wood wrapped with FRP, and pultruded composite sections. The experimental procedures will include the preparation of the specimens and introducing several artificial defects that may occur in composite structures in the field. In addition, the dielectric properties of various materials, involved in composite systems, will be experimentally evaluated. These properties will then be used as inputs for FEM simulations to verify the experimental results. Although outside the original scope of the thesis, the capacitance sensors will also be used to detect the poorly grouted zones and ungrouted cells in concrete masonry walls. Different capacitance sensors will be fabricated and used for the inspection and their performances will be compared to verify the theoretical findings.

5.2 Measurement of Material Dielectric Properties

The accurate measurements of the dielectric properties of different materials involved in test specimens is of prime importance in order to facilitate correlation of the

experimental data to the predicated FEM simulation results. A simple technique to determine the dielectric permittivity of a material is to sandwich a disc of the material of a known thickness, *d,* between two parallel conductors, each of an area *A*. By applying a potential difference between the parallel conductors, a uniform electric field is created within the material and the capacitance, *C*, can be recorded. The dielectric permittivity, ε_r, of the material inserted inbetween the plates is expressed as:

$$\varepsilon_r = \frac{Cd}{\varepsilon_o A} \tag{5.1}$$

where ε_o (the permittivity of free space = 8.8541×10^{-12} *F/m*).

Two *25 mm* square copper plates, ($A = 625\ mm^2$), were used as the parallel-plate capacitor electrodes. In order to ensure full contact between the material and copper plates, the material specimens were placed between two grips of a non-conductive clamp, as shown in Figure 5.1. Measurements were conducted using a high accuracy LCR meter (*INSTEK 816*).

Although Eq. (5.1) gives the theoretical value of the dielectric permittivity as a function of the measured capacitance and sensor geometrical parameters, dielectric permittivities cannot be determined experimentally by a single capacitance measurement. This is because the capacitance produced by the measuring leads, C_{lead}, cannot be isolated and subtracted from the total measured capacitance. Therefore, several samples with different thicknesses were tested to obtain different data points to establish a relationship between the thickness, *d*, and the measured capacitance, *C*, as follows:

$$C = C_{lead} + A\varepsilon_o\varepsilon_r \frac{1}{d} \tag{5.2}$$

Figure 5.2 shows the capacitance plotted as a function of the reciprocal of the dielectric thickness, *1/d*, for different materials used for the composite specimens and the constructed wall. As a result, a linear relationship for each material was produced and the dielectric permittivity was evaluated from the line slope of these relationships. The dielectric permittivities of different materials are summarized in Table 5.1.

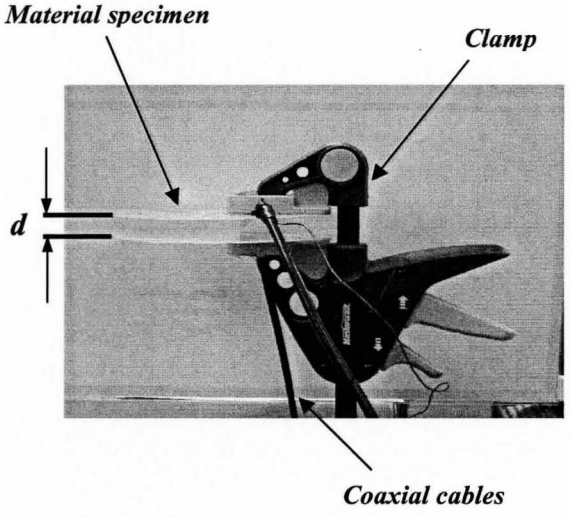

Figure 5.1: Experimental setup for dielectric permittivity evaluation

Table 5.1: Evaluated dielectric permittivities of different materials

Material	Dielectric permittivity, ε_r
Concrete	6.28
GFRP	3.12
Epoxy	3.87
Wood	2.89
Masonry	5.21
Grout	5.14

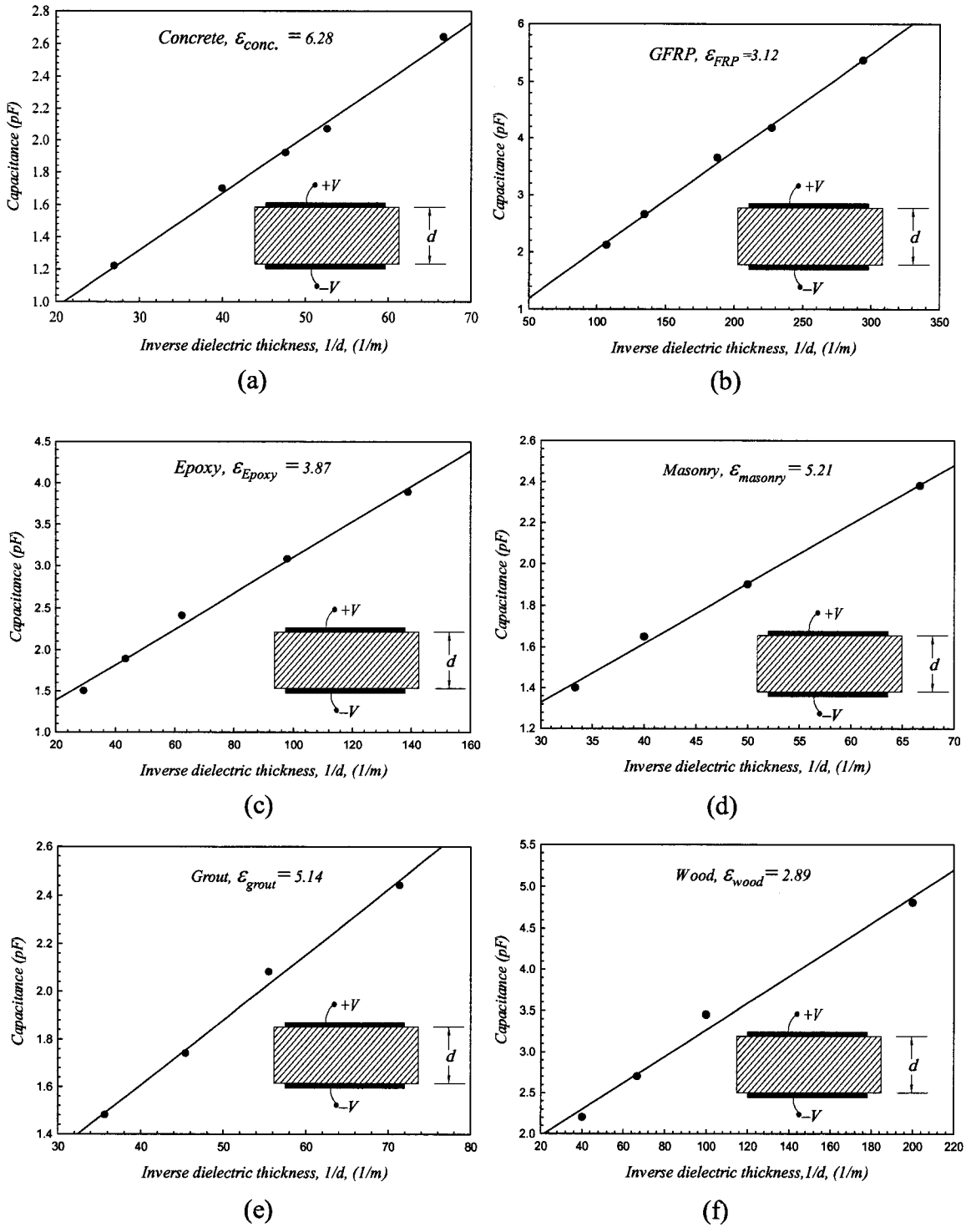

Figure 5.2: Evaluating dielectric permittivities for different materials (a) concrete, (b) GFRP, (c) epoxy, (d) masonry, (e) grout, and (f) wood

5.3 Composite Specimen Constructions

5.3.1 Series *A* (Composite/Concrete)

Two concrete blocks, *A1* and *A2*, with dimensions of *600 mm* (length) × *300 mm* (width) × *80 mm* (depth), were cast using the mix design given in Table 5.2. Each of the two specimens contained a series of pre-fabricated defects at concrete surface. For Specimen *A1*, Figure 5.3-(a), defects were created by inducing a total of *15* holes, five in each row, to a height, *h*, ranging from *2* to *10 mm* with an identical diameter of *40 mm* into the concrete substrate. These holes were created by placing aluminum discs with different thicknesses (*2.0, 4.0, 6.0, 8.0,* and *10 mm*) at the bottom surface of the formwork before the concrete was cast as shown in Figure 5.4-(a). Five of these holes (one row) were filled with epoxy to represent glue infiltration defects. Other five holes were filled with water to represent water intrusion defects. The remaining five holes were left empty to represent air void defects.

For Specimen *A2*, Figure 5.3-(b), a step-pyramid shape defect was created by placing a circular aluminum plate with different thicknesses (*2, 4, 6,* and *8 mm)* as shown in Figure 5.4-(b). This defect was used to simulate both air-filled and water-filled defects with different heights. This specimen was first tested after applying the GFRP layer with the defect volume empty to represent the air-filled defect, and then retested after injecting the defect volume with water which completely filled the defect volume to represent the water-filled defect.

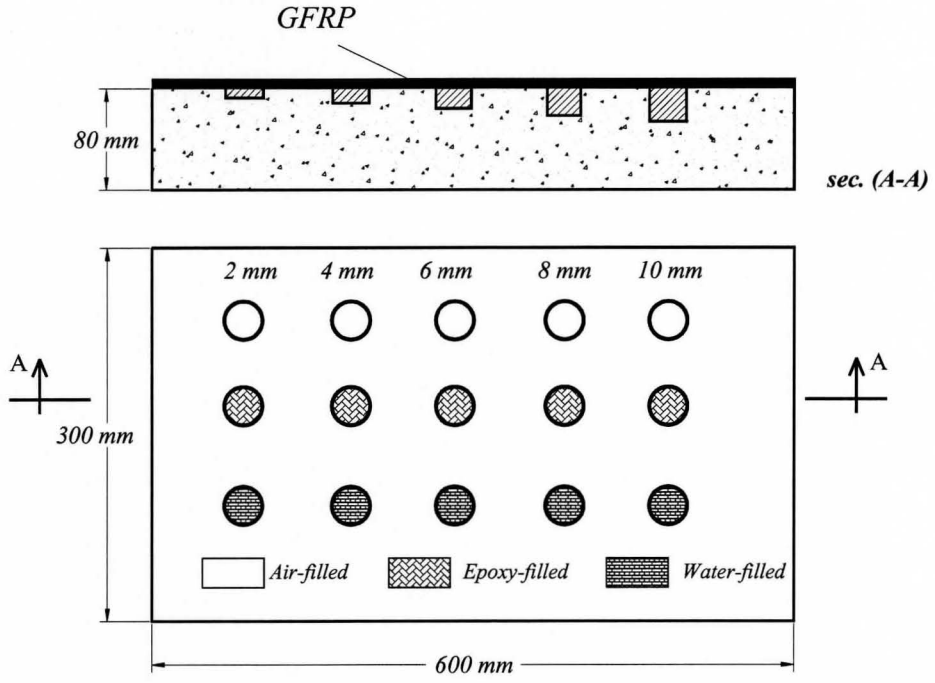

(a) Specimens *A1*

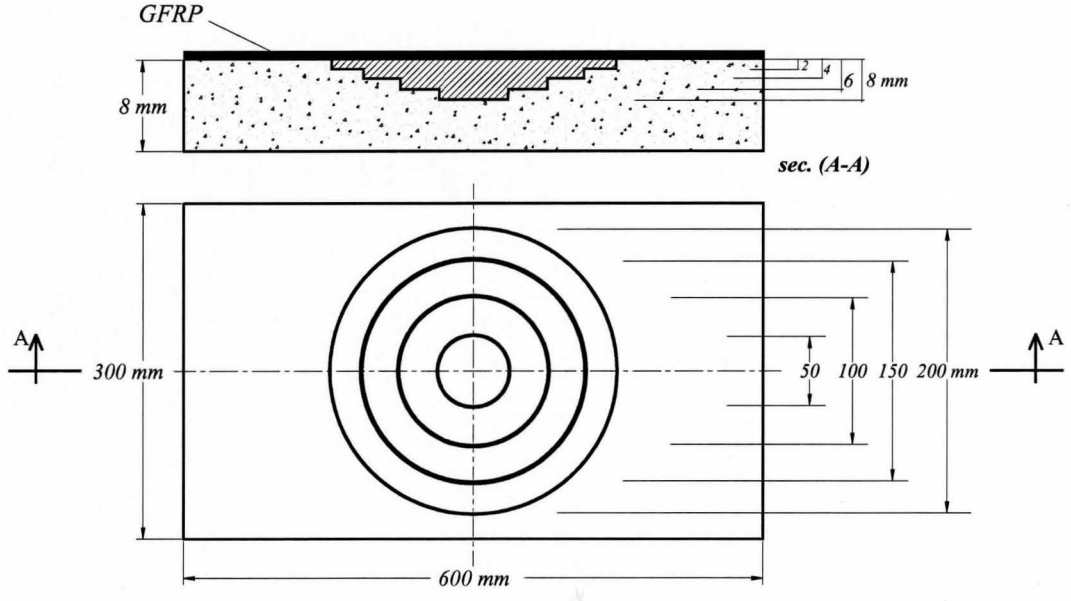

(b) Specimen *A2*

Figure 5.3: Defect configurations of series *A*, (a) Specimen *A1*, (b) Specimen *A2*

Table 5.2: Concrete mixture and composite material properties

Concrete Mixture Proportions	
Water-cement ratio (*w/c*)	0.6
water, (kg/m^3)	260
Cement, (kg/m^3)	481
Fine aggregate, (kg/m^3)	570
Coarse aggregate, (kg/m^3)	1,100
Maximum aggregate size, (mm)	13
Dry Glass composite properties	
Density, (g/m^3)	2.55
Tensile strength, (GPa)	3.24
Epoxy properties	
Elongation percent %	5
Tensile strength, (MPa)	50
Composite gross laminate properties	
Tensile strength, (MPa)	575
Laminate thickness, (mm)	1.3

A thin layer of form-release oil was applied to the form surfaces before the concrete was placed to facilitate aluminum discs removal after the casting and curing of concrete. The concrete was allowed to cure in the forms for *4* days and then the forms were removed.

Figure 5.5 shows the specimens after the formworks were removed. A single layer of GFRP laminate was applied to the surface of the concrete. The unidirectional GFRP laminate used in this study was typical of those commonly used in wet lay-up composites strengthening of concrete structures, Table 5.2. The epoxy used for the composite specimen provided a translucent surface to verify the results by visual inspections. A paint roller was used to saturate the fibres with epoxy before it was applied to the concrete surfaces. Figures 5.6-(a), and 5.6-(b) show the specimen *A1*, and specimen *A2* after applying the GFRP laminates on the top surface of the concrete specimens.

(a) (b)

Figure 5.4: Wood formworks with aluminum discs, (a) Specimen *A1*, (b) specimen *A2*

(a) (b)

Figure 5.5: Concrete blocks after the formworks were removed, (a) Specimen *A1*, (b) Specimen *A2*

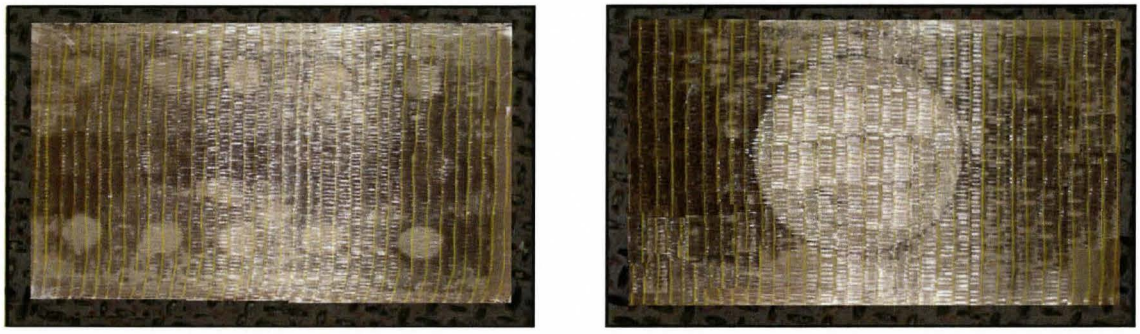

(a) (b)

Figure 5.6: Concrete blocks after applying the GFRP laminate, (a) Specimen *A1*, (b) Specimen *A2*

5.3.2 Series *B* (Composite/Timber)

Externally bonded composite wraps are gaining popularity for construction and rehabilitations of timber structural members such as beams and columns (Gentile et al. 2002). In addition to being subjected to common defects of composite members, such as delaminations and air voids, wood members are susceptible to biodegradation resulting in decay and deterioration of wood by primarily enzymatic activities of microorganisms. The decay usually occurs when the moisture exceed the fibre saturation point (*25-30* %) with the presence of organism such as fungi (Viitanen 1994). The decay affects the wood member's structural performance as it causes a loss of weight and a consequent reduction in the member strength.

The capacitance sensors capabilities were examined to detect the defects that may occur in timber columns wrapped with GFRP. The wrapped column was constructed using a segment of a *6* "*by 6* wood post (*600 mm* long), containing a series of fabricated defects at the GFRP/wood interface. Figure 5.7 shows the defect configurations for Face *A* and Face *B* of the wood specimen. Defects were induced by creating 5.0 holes with an identical diameter of *40 mm* into the wood substrate at Face *A*, as shown in Figure 5.8-(a), and *5* formed grooves at Face *B*, as shown in Figure 5.8-(b). These holes and grooves were of different heights, *h*, ranging from *2.0* to *10.0 mm*. A single layer of GFRP laminate was applied to wrap the wood column, as shown in Figures 5.9-(a) and 5.9-(b). The artificial defects, at Face *A*, were filled with sawdust before the application of GFRP laminate and then injected with water after applying the laminate to simulate wood decay

defects. The grooves at Face *B* were left empty to simulate air gaps and debonding defects.

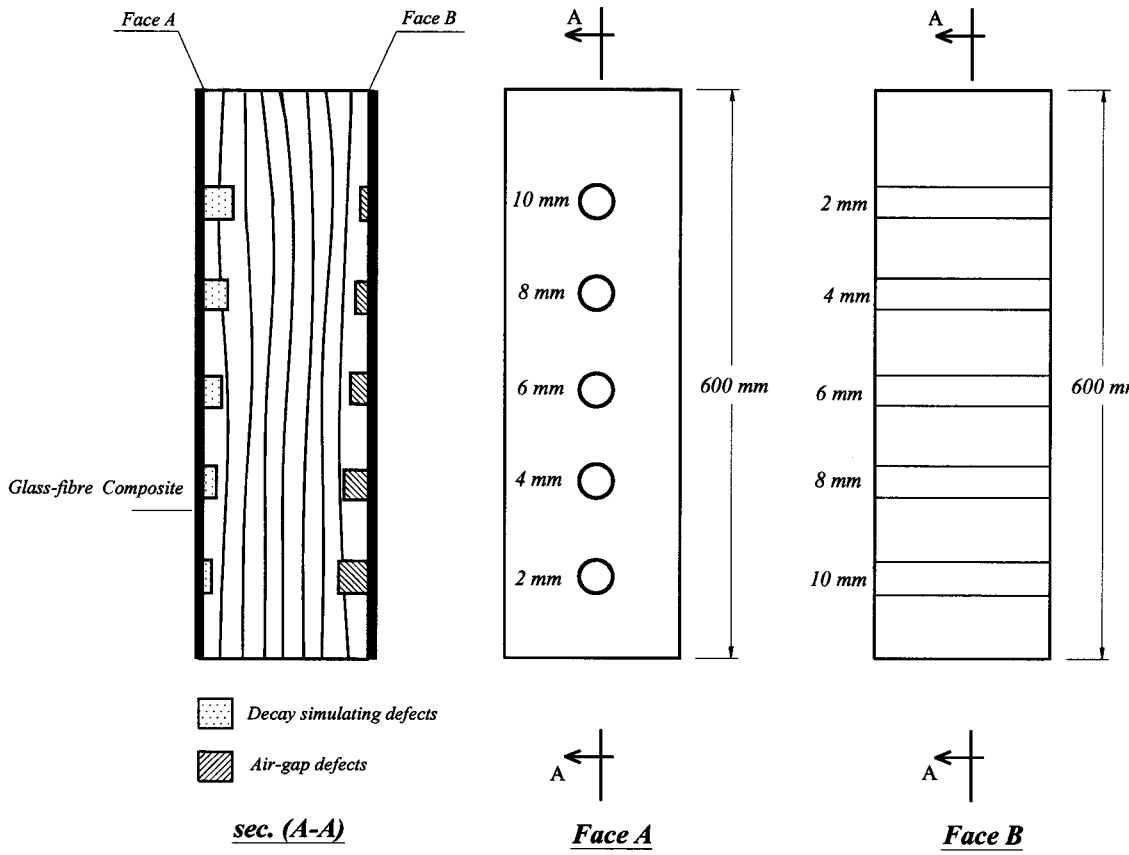

Figure 5.7: Defect configurations of series *B*

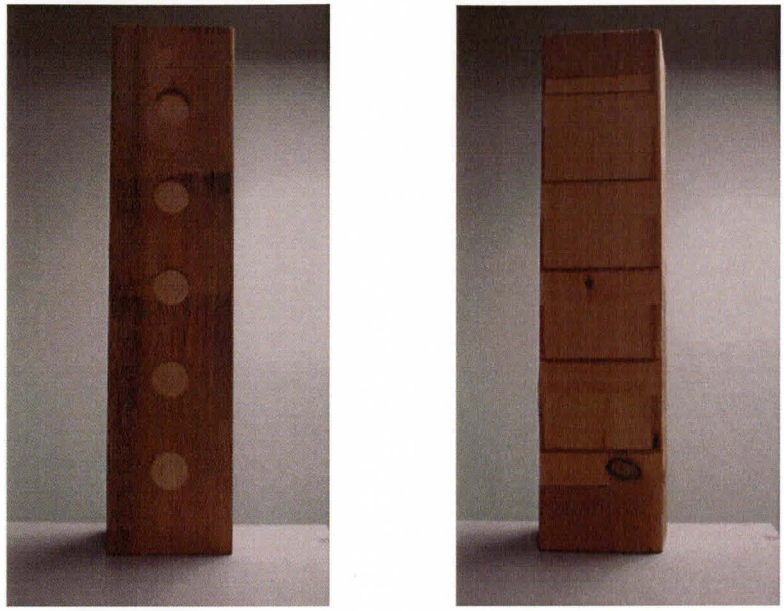

(a) (b)

Figure 5.8: The specimen with the pre-fabricated defects, (a) Face *A*, and (b) Face *B*

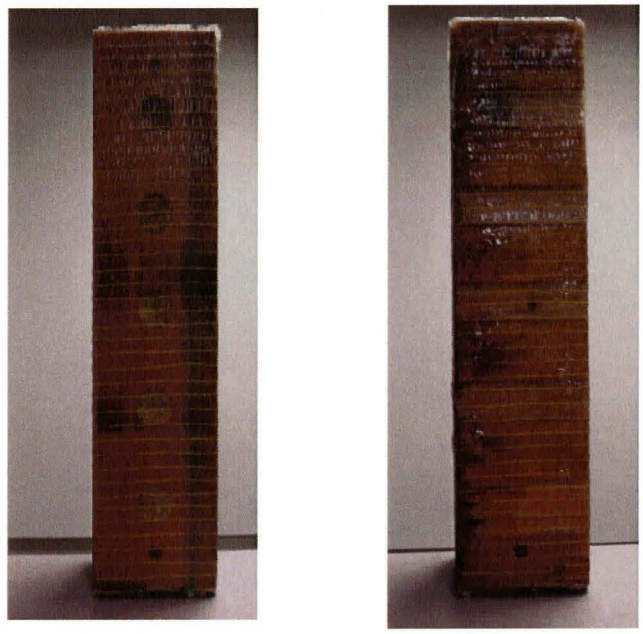

(a) (b)

Figure 5.9: The specimen after applying GFRP laminate, (a) Face *A*, and (b) Face *B*

5.3.3 Series *C* (Composite Pultruded Members)

Composite pultruded members have gained a lot of acceptance as structural members in many of civil engineering applications such as beams, columns, and truss members (Alampalli 2006). The capacitance sensor efficiency was examined to detect the delaminations and water intrusion defects in these members. Two GFRP specimens were used in this study. The Specimen *C1* was I-beam of (*100* × *100* × *6.5 mm*). The I-beam had a deficient in bond between different laminates in one of its flange during manufacturing that resulting in a delamination located around the flange mid thickness area, as shown in Figure 5.10-(a). The delamination was with a width of *55 mm*, and an average height of *1.2 mm* at a depth of *3 mm* from the upper surface of the flange. The Specimen *C2* was GFRP plate of dimensions *200 mm* (width) × *150 mm* (length) × *12.5 mm* (height). The plate had three pre-fabricated slots with rectangular cross sections each of which with the dimensions of *30 mm* (width) × *30 mm* (length) × *3 mm* (height) at different depths, *z*, from the upper surface of the plate, as shown in Figure 5.10-(b). For Face *A* of the plate, the slots were at depths, *z*, (*2*, *4*, and *6 mm*). While for Face *B* of the plate, the slots were at depth, *z*, (*3.5*, *5.5*, and *7.5 mm*). These slots were used to simulate both delaminations and water intrusions at different depths of the composite plate. This specimen was first tested while the slots left empty to represent the delaminations defect, and then was tested after injecting with water that completely filled the slots to represent water intrusion defects. Figures 5.11-(a) and 5.11-(b) shows the *C1*, and *C2* specimens.

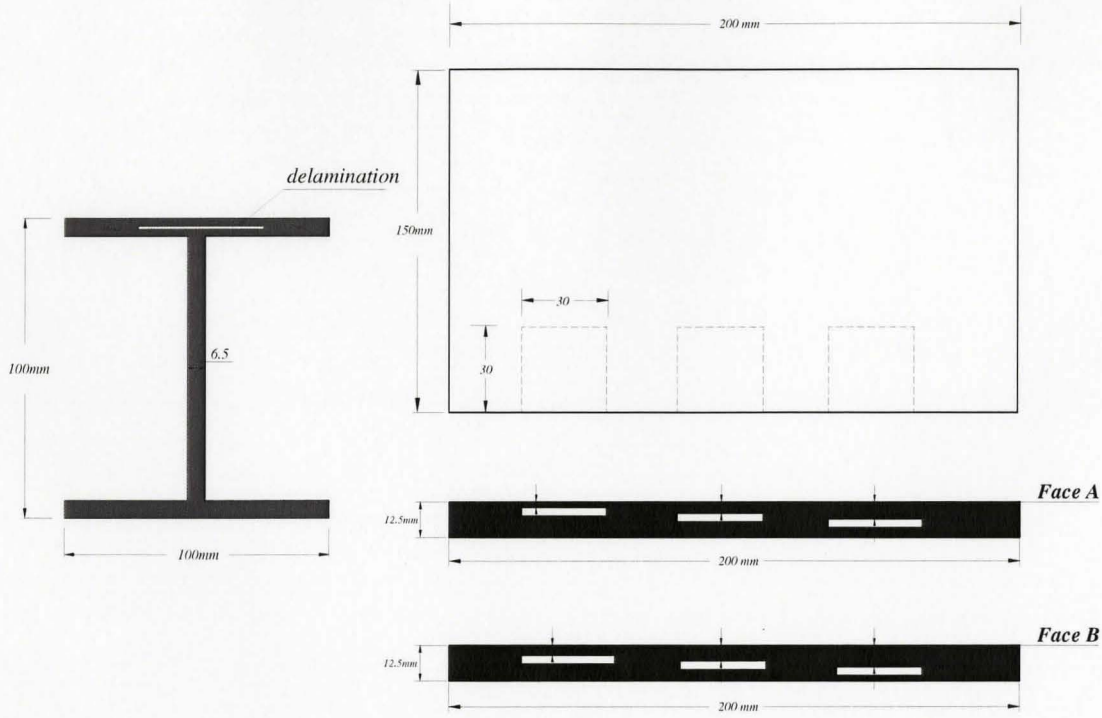

(a) Specimen *C1* (b) Specimen *C2*

Figure 5.10: Defect configurations of series *C*, (a) Specimen *C1*, and (b) Specimen *C2*

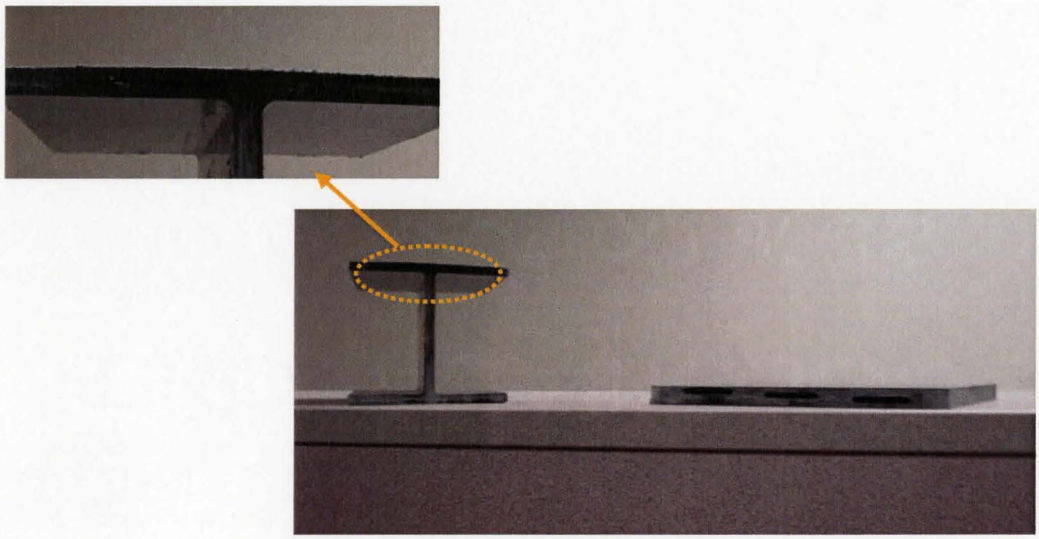

Figure 5.11: Pultruded sections with the defects

5.4 Sensor Fabrication

Three sensor configurations were fabricated and tested. Sensor (*CCS1*) is a coplanar capacitance sensor with electrode width, $s = 12$ *mm,* gap spacing, $2g = 8$ *mm,* and electrode length, $l = 40$ *mm.* The sensor electrodes were made of a copper tape and mounted together on a thin plastic sheet to keep a constant separation distance between the copper electrodes. This design was chosen to provide a sufficient penetration depth to detect all the defect depths for different composite specimens, since the penetration depth of *CCS1*, from Eq. (4.3), $T = 13.2$ *mm*. The other configurations were two IDCS designed by the author and fabricated by Printed Circuit Board (PCB) technology with two different wavelengths. (*IDCS1*) had a wavelength, $\lambda = 24$ *mm*, with a number of fingers, $N = 4.0$, finger width, $s = 6$ *mm,* gap spacing, $2g = 6$ *mm,* and finger length, $l = 40$ *mm*, as shown in Figure 5.12-(a). *IDCS1* had an estimated penetration depth, from Eq. (4.3), $T = 8$ *mm.* While (*IDCS2*) had a wavelength, $\lambda = 12$ *mm*, with number of fingers, $N = 8$, finger width, $s = 3$ *mm*, gap spacing, $2g = 3$ *mm*, and finger length, $l = 40$ *mm*. *IDCS2* had a sensor penetration depth, $T = 4$ *mm*, as shown in Figure 5.12-(b).

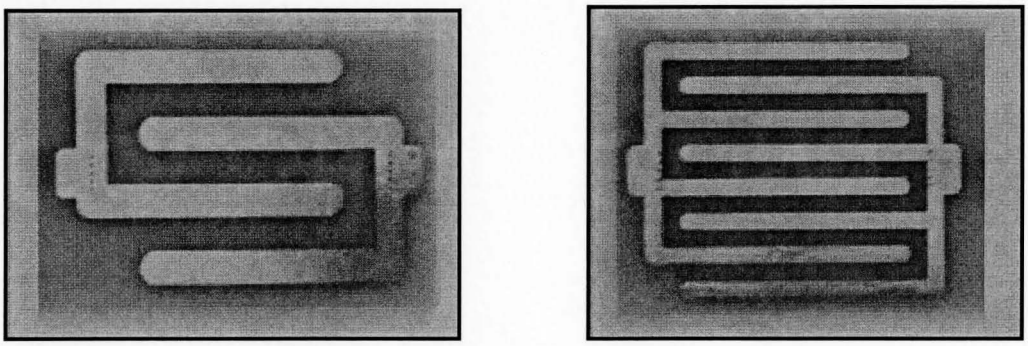

(a) (b)

Figure 5.12: IDCS sensors, (a) *IDCS1*, and (b) *IDCS2*

5.5 Measuring Procedures

Measurements reported here were collected using an *INSTEK 816* LCR meter with a *0.1%* accuracy. The measured capacitances were read off the LCR monitor and recorded. The LCR meter was provided with a test fixture that facilitates the connection of the sensor to the meter by coaxial cables. The performance for different sensors was compared with respect to its measurement variations and sensitivities.

5.6 Disturbance Factors

There are some disturbance factors that can affect the capacitance measurements. If these factors are avoided, more robust and sensitive results can be obtained. These factors are briefly described and discussed in the following sections, (Li 2003):

5.6.1 Sensor-Surface Contact Quality

Surface contact quality is one of the major sources of measurement uncertainties. Any air gap between the electrodes and the test specimen acts as a capacitance in series and result in a low measurement. The planar capacitance sensors are very sensitive to surface contact quality, since most of the field energy concentrates around electrodes. This effect can be reduced by placing the sensors away from the surface of the material. This, however, reduces the signal strength of the measurements. Another solution depends on using flexible substrate for sensors and applying pressure from the top to ensure a maximum contact.

5.6.2 Stray Capacitances

CCS and IDCS are more susceptible to noise since the magnitude of the measured capacitance is usually low. The source of stray capacitance is the sensor leads and the coaxial wires used to connect the sensor with measuring device. These capacitances can be minimized by proper shielding and reducing the length of the leads and the coaxial wires.

5.6.3 Electrode Deformation

Due to continuous use, the capacitance sensing electrodes may be subjected to possible electrode deformation, which may affect their measurement accuracy. Such deformation can lead to poor contact between the sensor surface and the material under test.

5.7 Results and Discussions

5.7.1 Series *A*

Figure 5.13 shows the capacitance measurements obtained from the coplanar sensor, *CCS1,* for different defect types. The measured capacitances were affected by the presence of air gaps as the capacitance decreased exponentially with the increase of air defect heights, *h*. The capacitance measurements of the sounds areas correspond the defect height, *h=0.0*. The decrease of the output signals is attributed to the low value of the dielectric permittivity of air, $\varepsilon_a = 1.0$, compared to that of the concrete, $\varepsilon_{conc.} = 6.28$, as shown in Figure 5.13-(a).

In the case of epoxy-filled defects, the capacitance measurements also decreased with the height, *h*, of defects. However, the decrease had a lower rate than in air defects, as shown in Figure 5.13-(b). This is because of the higher dielectric permittivity value of epoxy, $\varepsilon_{Epoxy} = 3.87$, compared to that of air, $\varepsilon_a = 1.0$. Therefore, the difference between the values of dielectric permittivities of the defect's material and concrete, in the case of epoxy-filled defects, is less than in the case of air-filled defects, which affects the variation of the measured capacitances.

Due to the high value of the dielectric permittivity of water, ε_w=81, compared to that of concrete, $\varepsilon_{conc.} = 6.28$, the capacitance measurements, in the case of water-filled defects, increased with the defect heights, *h*, as shown in Figure 5.13-(c).

The FEM simulations results were also plotted in same figures for different defect types. There were good agreements between the results obtained from the experimental

tests, $C_{Exp.}$ and those of the FEM, C_{FEM}. Figures 5.13-(d), 5.13-(e), and 5.13-(f) show comparisons between these results for different defects. The mean value of the ratio (C_{Exp}/C_{FEM}) for different defect types is approximately *1.10*. The deviation between the experimental and FEM results may be attributed to the fact that the *2D* FEM simulations ignore the fringing end effects as electrodes are assumed to be of infinite length. Moreover, disturbance factors would contribute to these deviations such as the stray capacitance of the test lead wires as well as the surface contact quality.

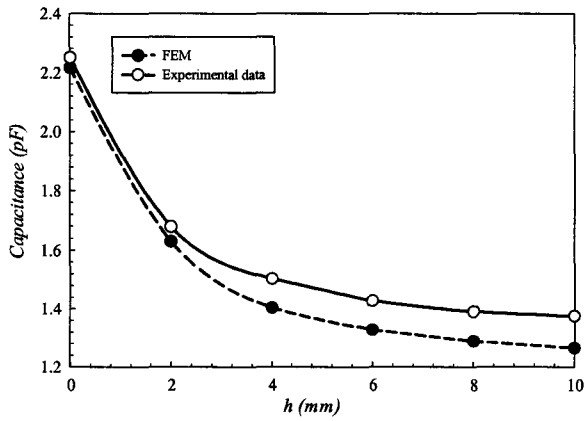

(a) The capacitance versus the air defect heights

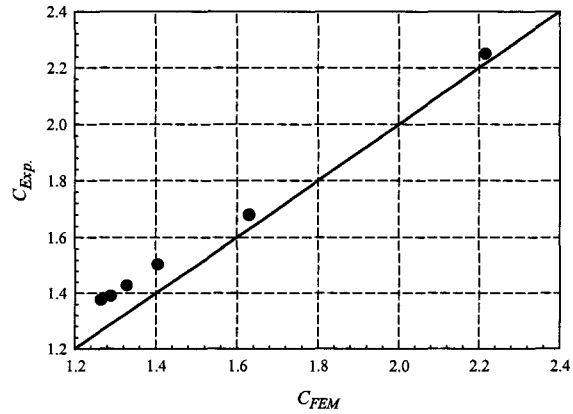

(d) The experimental and FEM results comparison

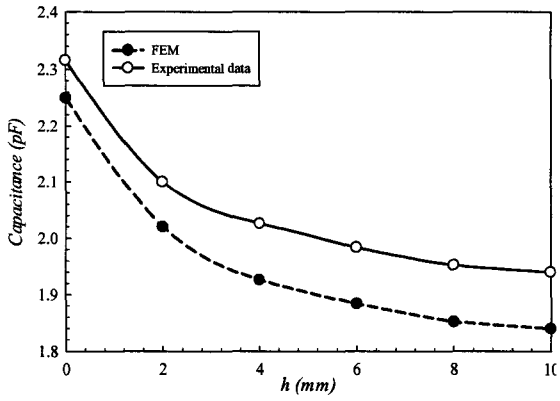

(b) The capacitance versus the epoxy defect heights

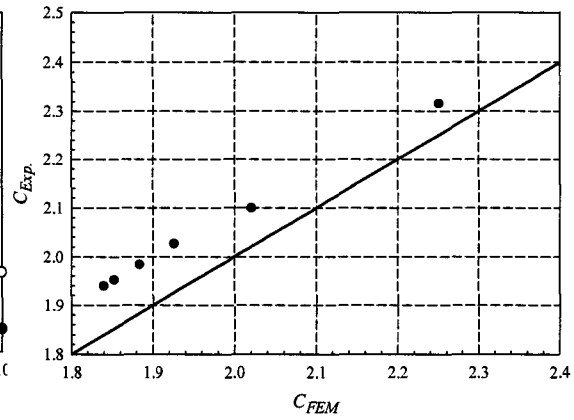

(e) The experimental and FEM results comparison

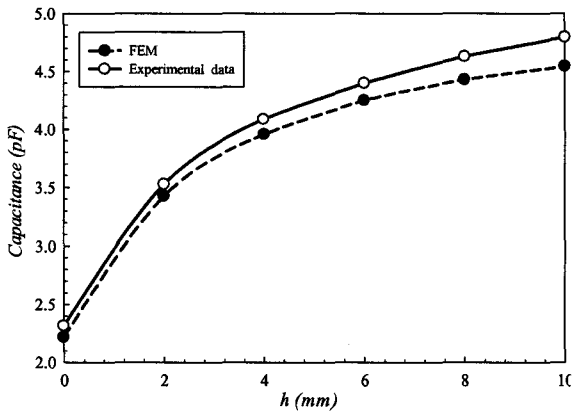

(c) The capacitance versus the water defect heights

Water-filled defects

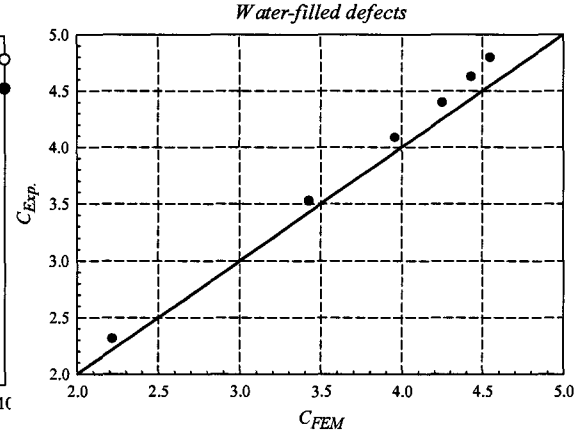

(f) The experimental and FEM results comparison

Figure 5.13: The experimental and FEM results obtained from *CCS1* versus different defect heights, and result comparisons

Figure 5.14 shows the capacitance measurements obtained from *IDCS1* and *IDCS2* for different defects. As expected, the capacitance decreased as the defect height, h, increased in both cases of air and epoxy defects, as shown in Figure 5.14-(a) and Figure 5.14-(b) respectively, while the capacitance increased with the defect heights in the case of water defects, as shown in Figure 5.14-(c). The capacitance variations occurred for defect height, h, less than the penetration depth, T, for the sensors. Consequently, the output responses had the same values for defect heights more than *6 mm* for *IDCS1* and more than *4 mm* for *IDCS2*. It is important to note that *IDCS1* and *IDCS2* had high signal strength over the coplanar capacitance sensor, *CCS1,* which resulted in more accurate and robust measurands. The FEM were also plotted for both IDCS and they had the same general trend for the experimental data. The comparisons between the experimental and FEM results for IDCS for different defect types are shown in Figures 5.14-(d), 5.14-(e), and 5.14-(f). The mean value of the ratio (C_{Exp}/C_{FEM}) for different defect types is approximately *1.14*.

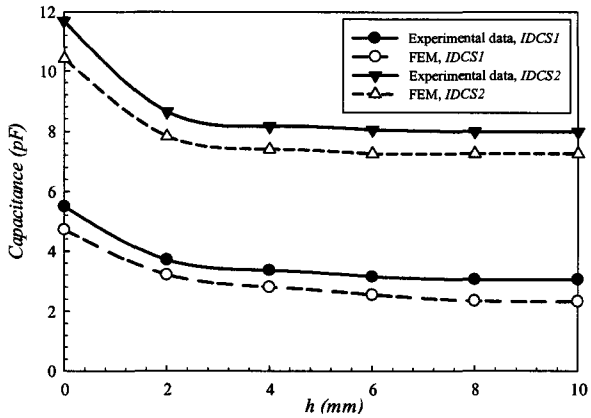

(a) The capacitance versus the air defect heights

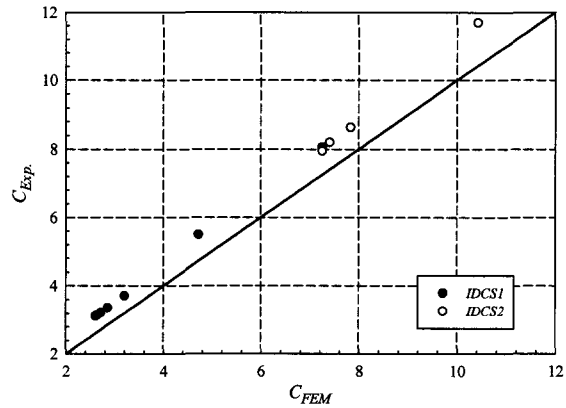

(d) The experimental and FEM results comparison

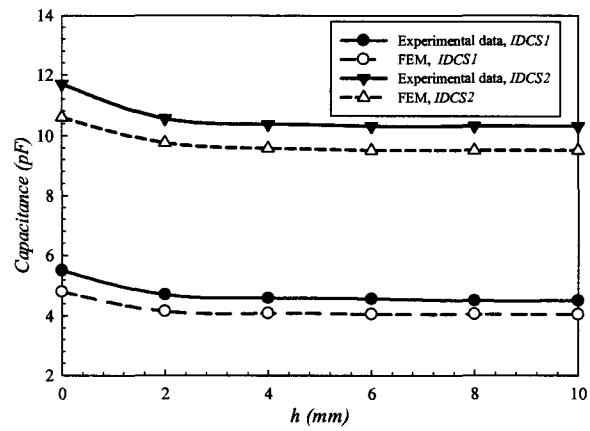

(b) The capacitance versus the epoxy defect heights

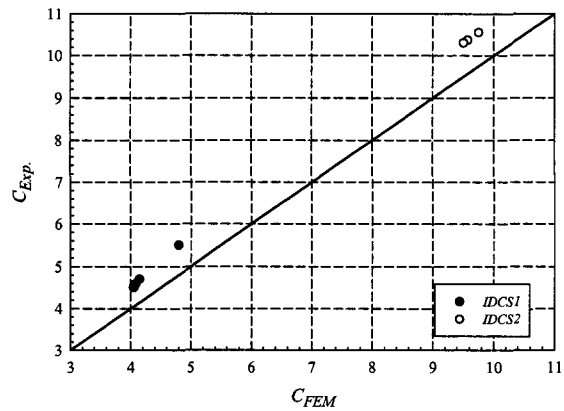

(e) The experimental and FEM results comparison

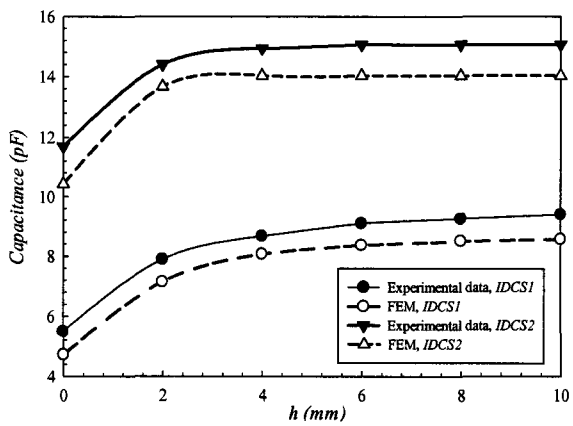

(c) The capacitance versus the water defect heights

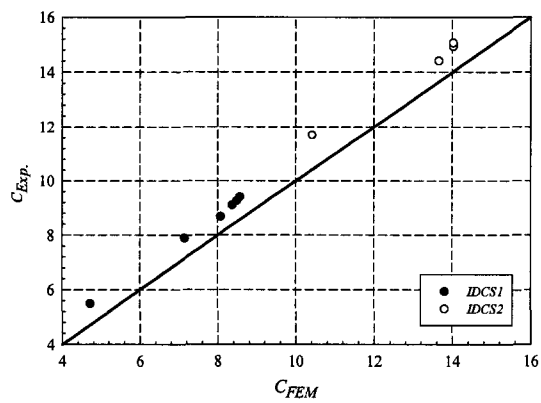

(f) The experimental and FEM results comparison

Figure 5.14: The experimental and FEM results obtained from (*IDCS1* and *IDCS2*), and the result comparisons

Figures 5.15-(a), 5.15-(b), and 5.15-(c) show the capacitance variations versus the defect heights, *h*, for the three different sensors. As can be seen, *IDCS2* gave higher reading variations for small defect heights than *IDCS1* and *CCS1*. This is due to that the electric field distributed over a small volume of the material, basically, the volume, which had a maximum penetration depth of *4 mm*. Therefore, the small change of the material composition close the sensor surface caused a large variation of *IDCS2* responses, while the change in material dielectric signatures far from the sensor had no significant effect on the measured capacitances. The capacitance variation data against the defect height, *h*, was nonlinear. This resulted from the non-uniform electric field distribution of the capacitance sensors since the most of the field energy concentrates around electrodes.

Figures 5.15-(d), 5.15-(e), and 5.15-(f) show the sensitivity of sensors versus the defect heights, *h*. for different defects. The sensor sensitivity indicates how much the signal response is affected in damaged zones with respect to sensor response in sound regions and can be defined as:

$$\%\ Sensor\ Sensitivity = \frac{C_{undamaged} - C_{damaged}}{C_{undamaged}} \times 100 \tag{5.3}$$

where $C_{damaged}$ and $C_{undamaged}$ are the capacitance measurements for damaged and undamaged regions.

These figures show that the sensor sensitivity increased with the defect height, *h*, as long as the height was less than the sensor penetration depth, *T*. *DCS1* had the highest sensor sensitivity for air-filled (*32-45%*) and epoxy-filled defects (*13-18%*) for defect

heights between *2.0-10.0 mm*, while *CCS1* had the highest sensitivity for water defects (52-*107%*) for defect heights between *2.0-10.0 mm*.

Although *CCS1* seems to be an appropriate sensor in terms for its detection depth, reading variations, and sensitivity, it is more susceptible with noise and stray capacitance due to its low signal strength compared to IDCS. *IDCS1* appears to be most effective sensor to detect different type of defects for a range of defect heights of *8 mm*.

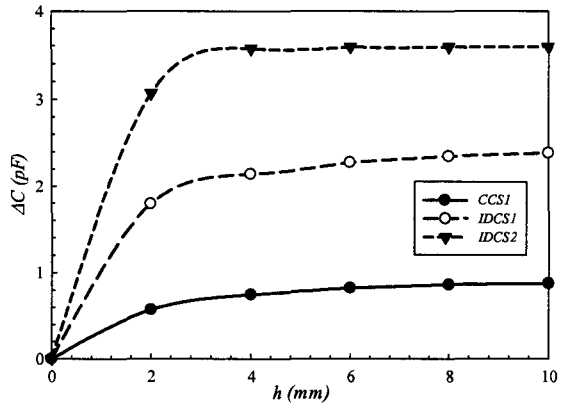

(a) The capacitance variations versus air defects

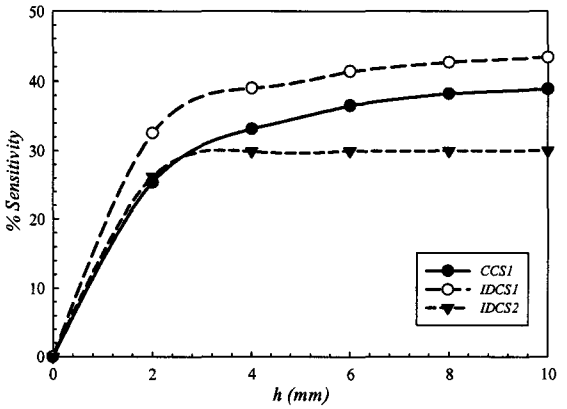

(d) The sensor sensitivity versus air defects

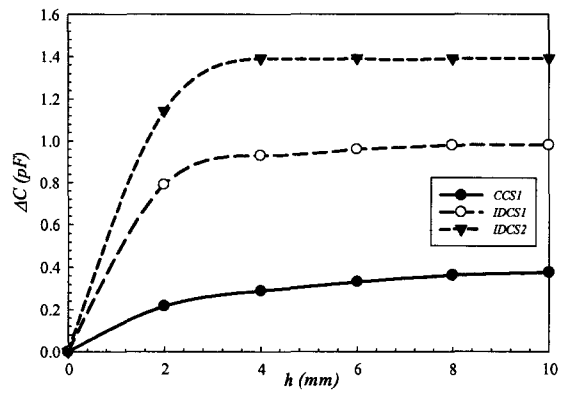

(b) The capacitance variations versus epoxy defects

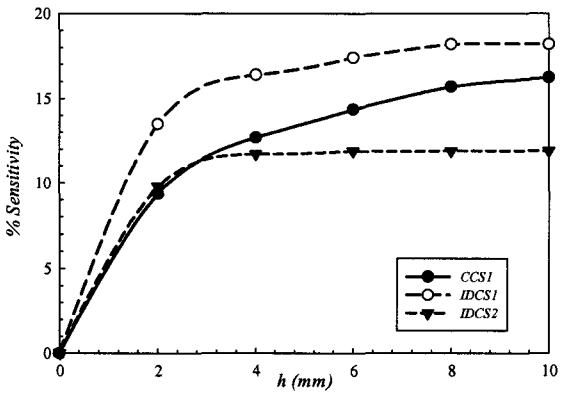

(e) The sensor sensitivity versus epoxy defects

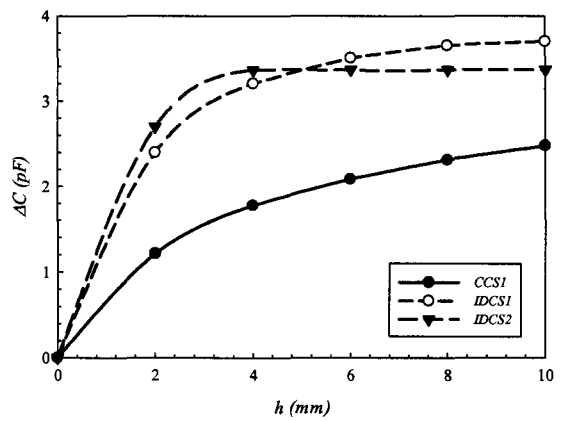

(c) The capacitance variations versus water defects

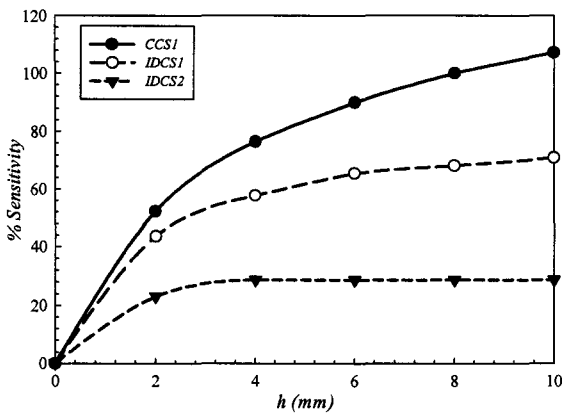

(f) The sensor sensitivity versus water defects

Figure 5.15: Capacitance variations and sensor sensitivities of different sensors for different defect types

The capacitance was measured, for specimen *A2*, each *25 mm* with a grid shown in Figure 5.16, so that the centre of the sensor occurred at the intersections of gridlines. These measurements were recorded for both the air-filled and water-filled defects. The experimental data, then, was fitted using surface regression analysis. Figure 5.17 shows the capacitance profile for the air-filled defects, the capacitance had the lowest values in the defect centre where it had the highest height and increased further away from the centre. Unlike the capacitance profile in air-filled case, the capacitance had the highest level in the centre of water-filled defect, and the larger the distance far from the centre, the lower the value of the measured capacitance, as shown in Figure 5.18.

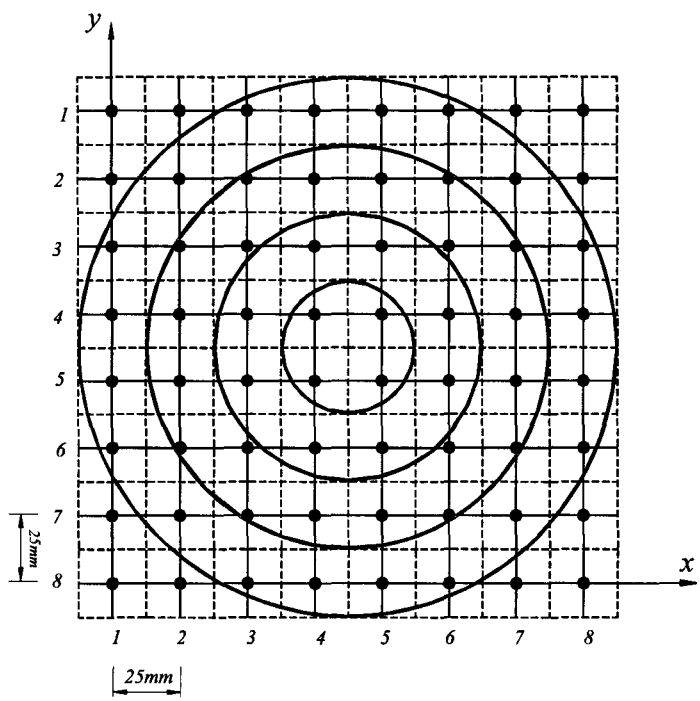

Figure 5.16: The measurement grid of the specimen *A2*

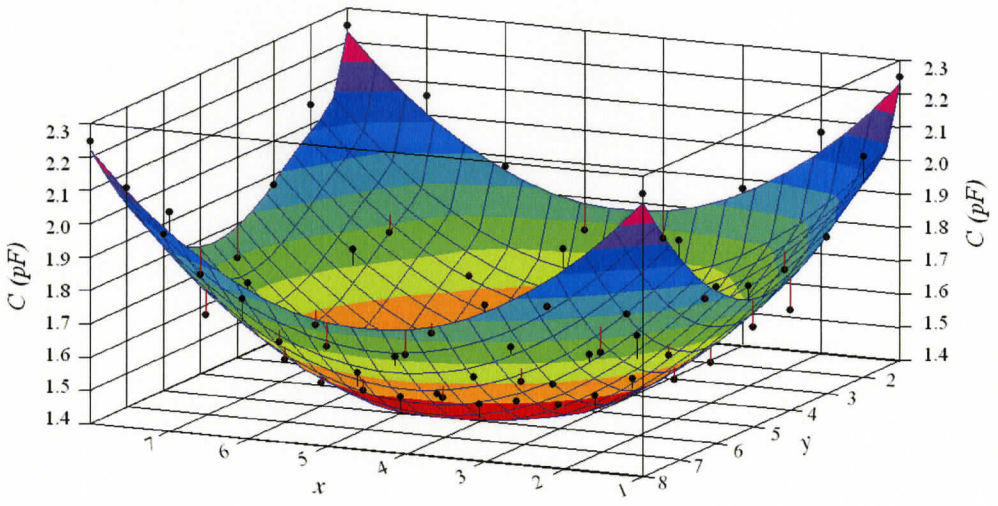

Figure 5.17: Capacitance profile for air-filled defect of the specimen *A2*

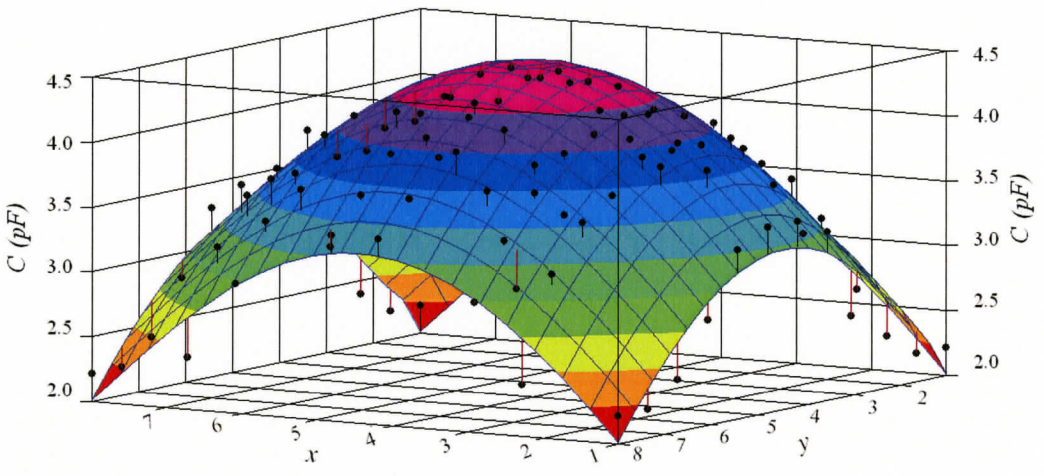

Figure 5.18: Capacitance profile for water-filled defect of the specimen *A2*

5.7.2 Series *B*

Figure 5.19 shows the decrease of the capacitance measurements due to the air defects obtained from *CCS1*, in Figure 5.19-(a) and from IDCS, in Figure 5.19-(b). The decrease in the output signals is attributed to the low value of the dielectric permittivity of air, $\varepsilon_a = 1.0$, compared to that of the wood, $\varepsilon_{wood} = 2.89$. The output responses, however, had almost the same value for defects with heights more than the sensor penetration depth. For *IDCS1*, the capacitance decreased for defects less than *8 mm* height and had a constant value for defects that extended more than *8 mm*, as shown in Figure 5.19-(b). While *IDCS2* had a penetration depth of *4 mm*, the capacitance, therefore, had a constant value for the defect heights more than *4 mm*, as shown in Figure 5.19-(b). The FEM results were plotted against the experimental measurands. In general, both sets of results have the same trend with the mean value of ratio (C_{Exp}/C_{FEM}) of *1.11* as shown in Figure 5.19-(c) and Figure 5.19-(d). The comparison between the variations of the three sensors for air-filled defects was shown in Figure 5.20 and between the sensitivities was shown in Figure 5.21. The *IDCS2* had the highest capacitance variations for air defect less than *4.0 mm*; while it had no noticeable variations for defects more than *4.0 mm*. *IDCS1* gave the highest sensor sensitivity than the two other sensors as the sensitivity was ranging between (*16-26%*) for defect heights between (*2-10 mm*).

The increase of the capacitance signals with the increase of the simulating decay defect heights using *CCS1* is shown and plotted in Figure 5.22-(a) and using IDCS in Figure 5.22-(b). The comparison between different sensors in reading variations is shown

in Figure 5.23 and in sensor sensitivities is shown in Figure 5.24. *CCS1* had as high sensitivity as *65-160%* for simulating decay heights between *2-10 mm*.

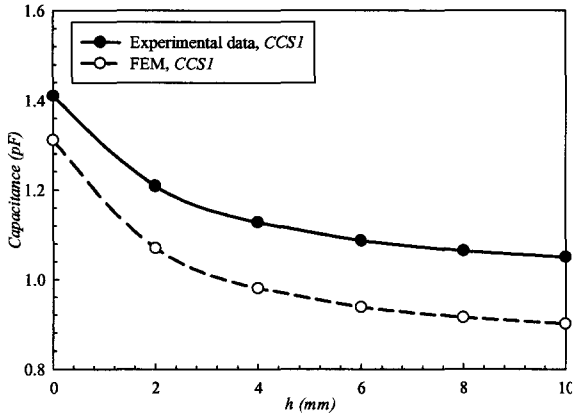

(a) The capacitance of *CCS1* versus the air defect heights

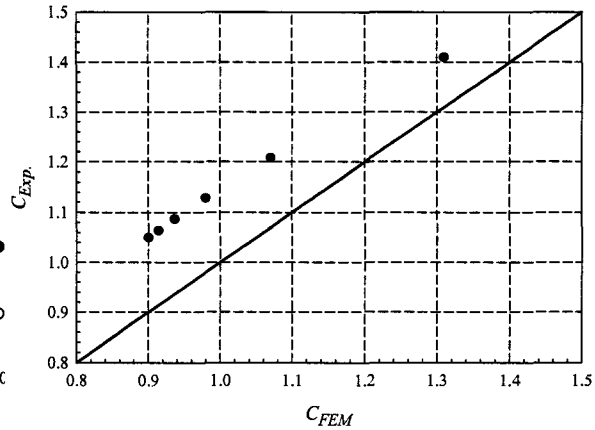

(c) The experimental and FEM results comparison

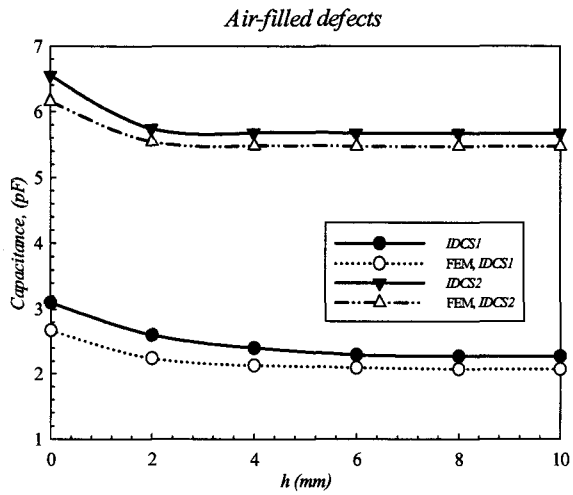

(b) The capacitance of IDCS versus the air defect heights

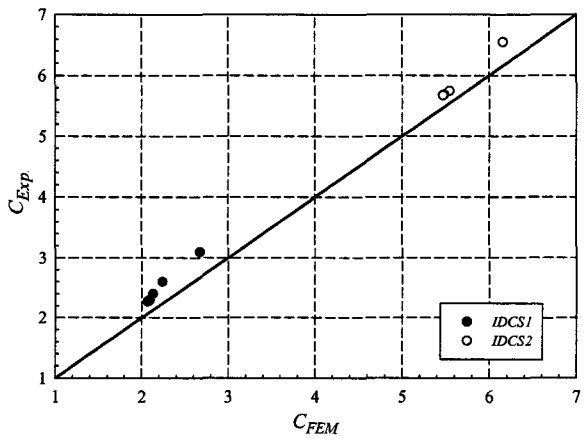

(d) The experimental and FEM results comparison

Figure 5.19: The experimental and FEM results of air defects of GFRP /wood specimen, and the result comparisons

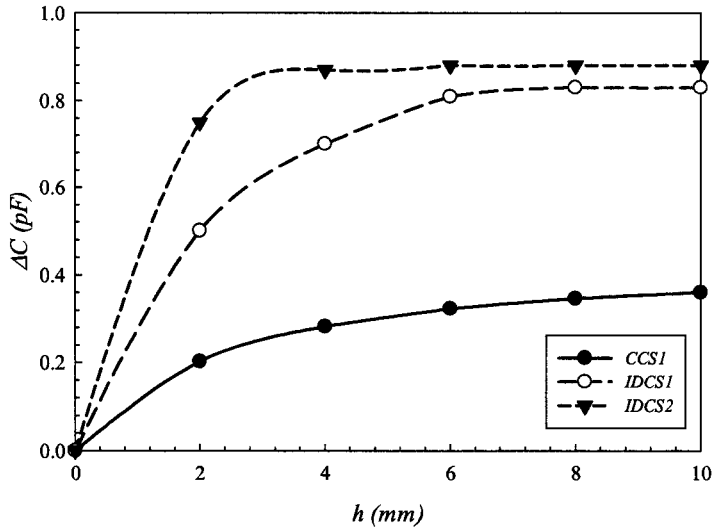

Figure 5.20: Capacitance variations for air defects of the GFRP/wood specimen

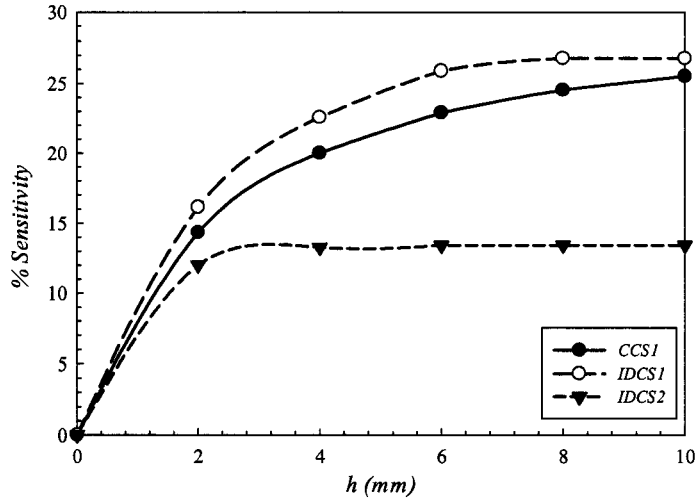

Figure 5.21: Sensor sensitivities for air defect of the GFRP/wood specimen

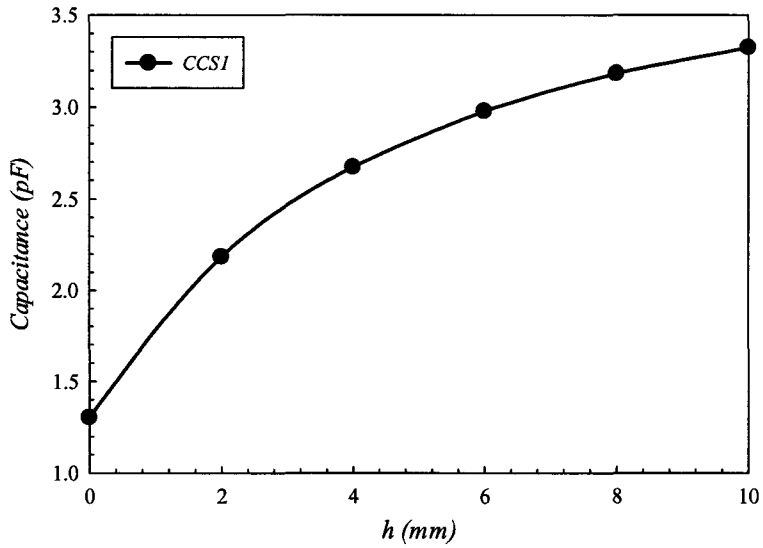

(a) Capacitance measurements from *CCS1*

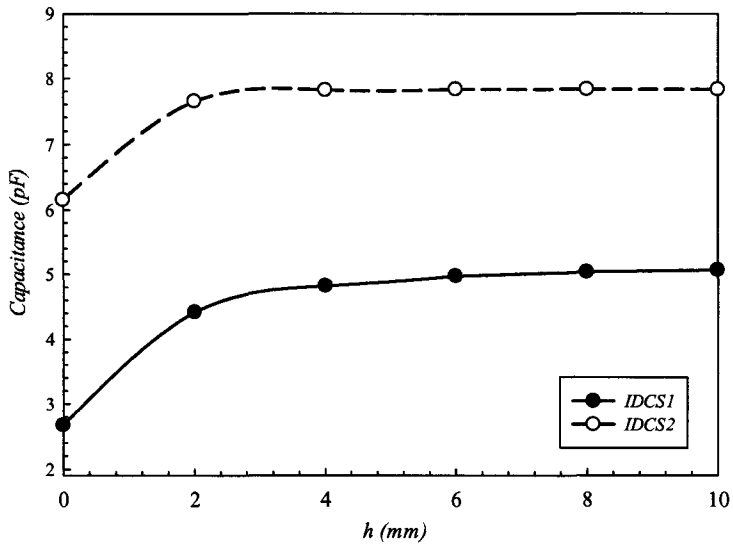

(b) Capacitance measurements from *IDCS1*, and *IDCS2*

Figure 5.22: Experimental results for decay defects of the GFRP/wood specimen

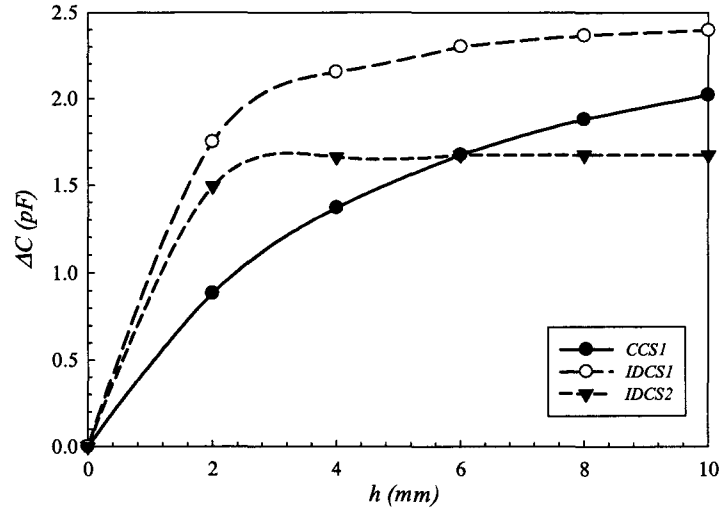

Figure 5.23: Capacitance variations for the simulated decay defects of the GFRP/wood specimen

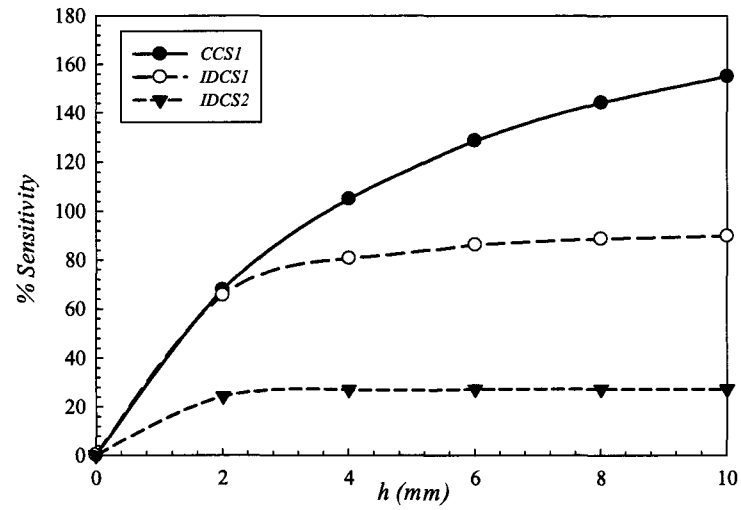

Figure 5.24: Sensor sensitivities for the simulated decay defects of the GFRP/wood specimen

5.7.3 Series *C*

The capacitance measurements were recorded for the specimen *C1* using the *CCS1* for both the delamination. The capacitance decreased in the delamination region by *12.5 %* compared to the sound regions. To test the ability of the sensing system to reproduce the measurements, *10* measurements were performed for the delamination region. In each measurement, the sensing system was reset to its initial condition. The results of these repeatability tests for were shown in Figure 5.25. The maximum variation from the mean was observed to be *0.02 pF* (*1.87%*).

The measurements were also recorded for the GFRP plate for both Face *A* and Face *B* using *CCS1*, *IDCS1*, and *IDCS2*. The capacitance measurements were affected by the presences of the delaminations and water defects. The sensor sensitivity decreased as the delamination and water defects depths, *z*, increased, as shown in Figures 5.26 and 5.27. The sensors had the highest sensitivity for delamination and water intrusion depth, *z =2mm*, as the sensitivity of *CCS1* for delamination and water intrusion was of *14%* and *96%* respectively. Again, the high sensor sensitivity for water intrusion defect detection is attributed to the high dielectric permittivity of water, ε_w=81. The decrease of the sensor senstivity resulted from the non-uniform electric field distribution of the capacitance sensors since the most of the field energy concentrates around electrodes. Therefore, the change in dielectric permittivities nearest to the electrodes have greater influence on the sensor signals compared to dielectric permittivities of materials deep in the test specimen.

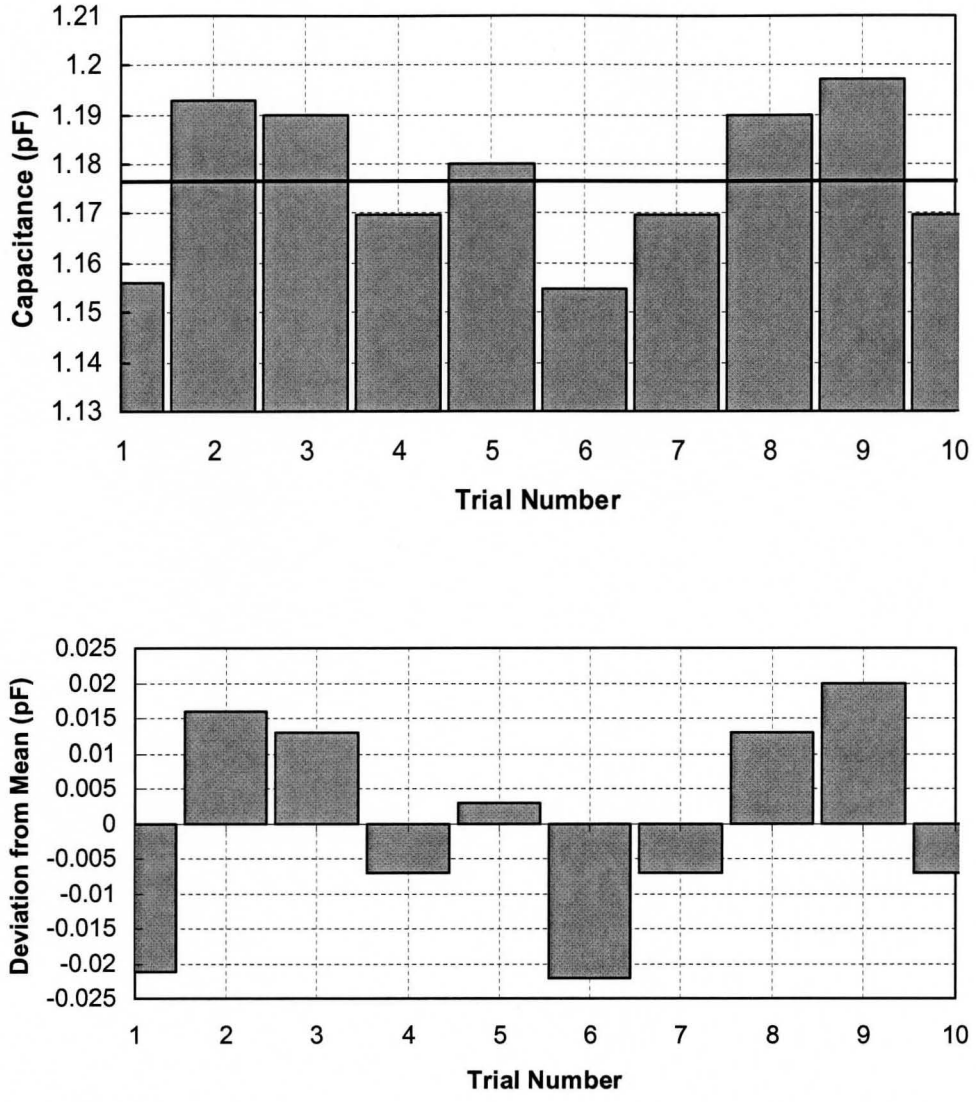

Figure 5.25: Repeatability test of the capacitance measurements for the delamination of I-beam specimen, *C1*

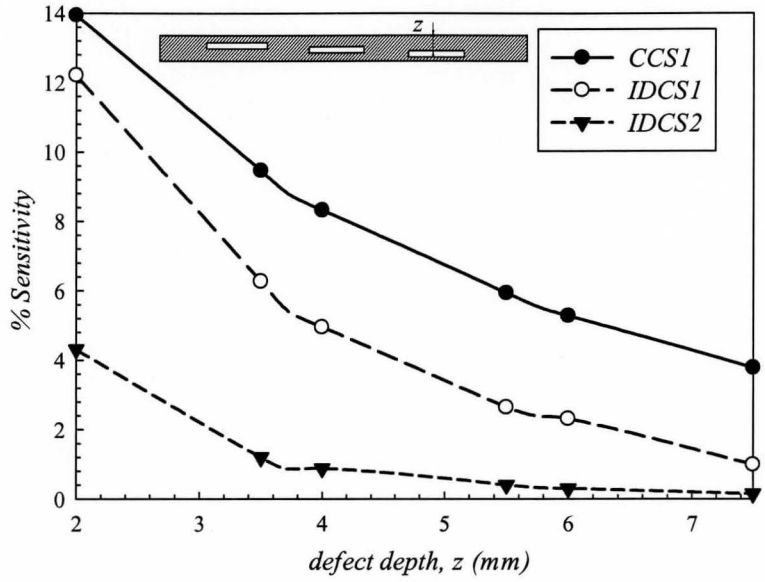

Figure 5.26: Sensor sensitivities for the delamination defects of the Specimen *C2*

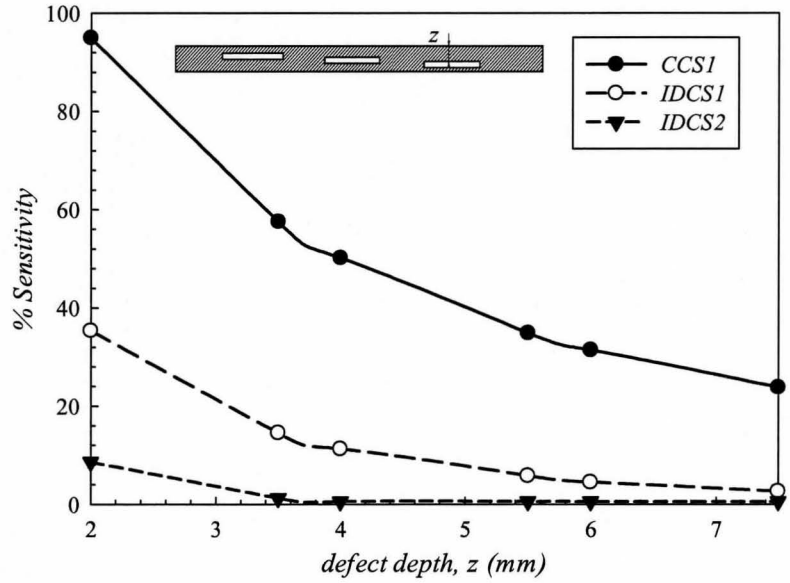

Figure 5.27: Sensor sensitivities for the water intrusion defects of the Specimen *C2*

5.8 Other Applications: Detection of Poorly Grouted/Ungrouted cells in Masonry Concrete Constructions

5.8.1 Background

When reinforcement is introduced in masonry constructions, grouting of the block cells is necessary for bond development between the steel reinforcement and masonry blocks. Problems associated with incomplete grouting, unfilled cells, and unbonded reinforcement can significantly alter the response of masonry walls and result in an unsatisfactory response, lower strength, and may require demolition and reconstruction of a significant portion or complete walls. In an earlier study by (Shedid et al. 2005) showed that incomplete filling of grout cells can significantly effect strength and ductility of the masonry walls.

Figure 5.28 shows the load displacement relationship of a sound wall and a wall with accidentally unfilled lower courses during construction. As can be seen from the figure, the response of the two walls is significantly different. Figure 5.29 shows the ungrouted cells which were later attributed to accumulation of hardened mortar dropping on the wall's horizontal shear reinforcement, which is very common during construction of reinforced masonry block walls (Shedid et al. 2005). Test results and further communication with the masonry construction industry (CMDC, 2007), and masonry design and consulting firms demonstrated that such construction errors are not uncommon in North America (CMDC, 2007). The engineering inspection and detection of possible unfilled walls zones is essential especially in critical zones in shear walls designed to resist seismic forces.

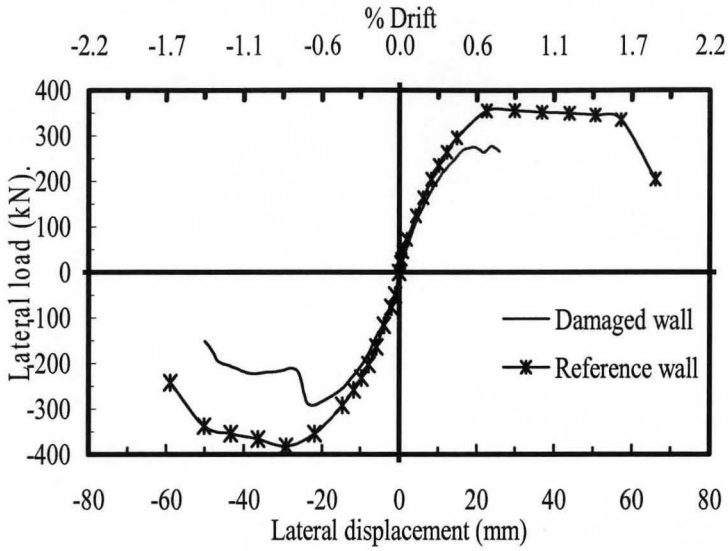

Figure 5.28: Envelope of load-displacement for the test walls (Shedid et al. 2005)

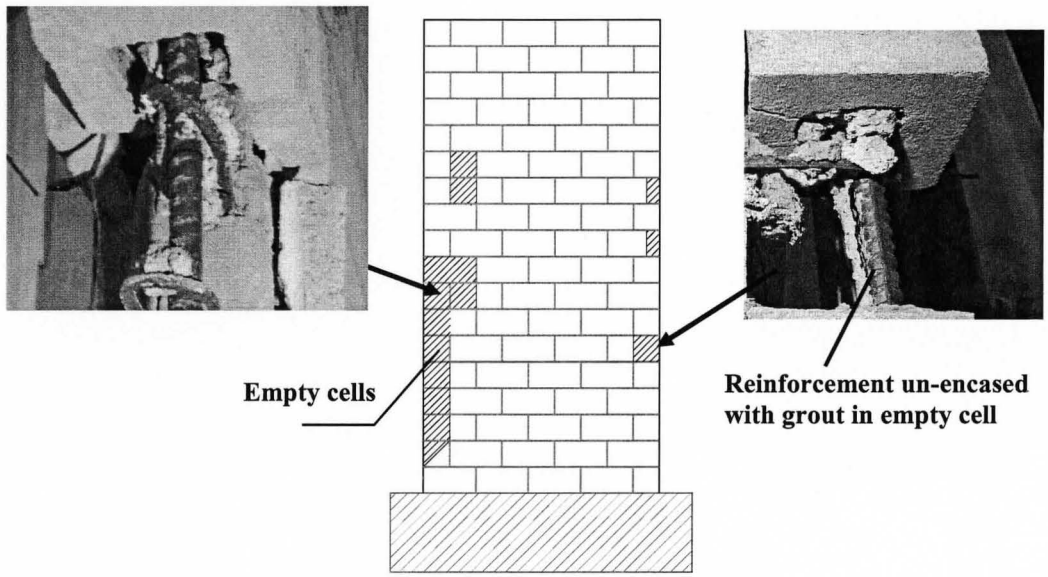

Figure 5.29: Unfilled cell information in the test wall (Shedid et al. 2005)

5.8.2 Test Specimen

A square masonry wallet, *4* block wide by *8* block high, was constructed with two fully grouted columns, *C-1*, and *C-7* (see Figure 5.30). Another two columns were grouted expect for one cell in column *C-5*, and two cells in column *C-3*, which were filled with Styrofoam during the grouting process to simulate air (the Styrofoam's dielectric permittivity is equal to that of air). The rest of the cells were kept ungrouted, as shown in Figure 5.30.

Three coplanar capacitance sensors were designed and fabricated for wall inspection. The three designs were of ($s \times g$) as following: *(25 ×8)* for *S1, (20 ×10)* for *S2*, and *(15 ×12)* for *S3*, where s and g are in *mm*. The length, l, of both electrodes was kept constant and equal to *50 mm*. These designs, based on Eq. (4.3), were chosen to provide a penetration depth not less than *25 mm* into the inspected wall. The sensor electrodes were made of a copper tape and mounted together on a thin plastic sheet to maintain a constant separation gap between the copper electrodes. Using the three sensors, the *29* grouted and the *35* ungrouted cells were scanned along the surface of the wall. The performance for these sensors was compared with respect to coefficient of variation, sensitivity, and the signal-to-noise ratio (SNR) for the measured results.

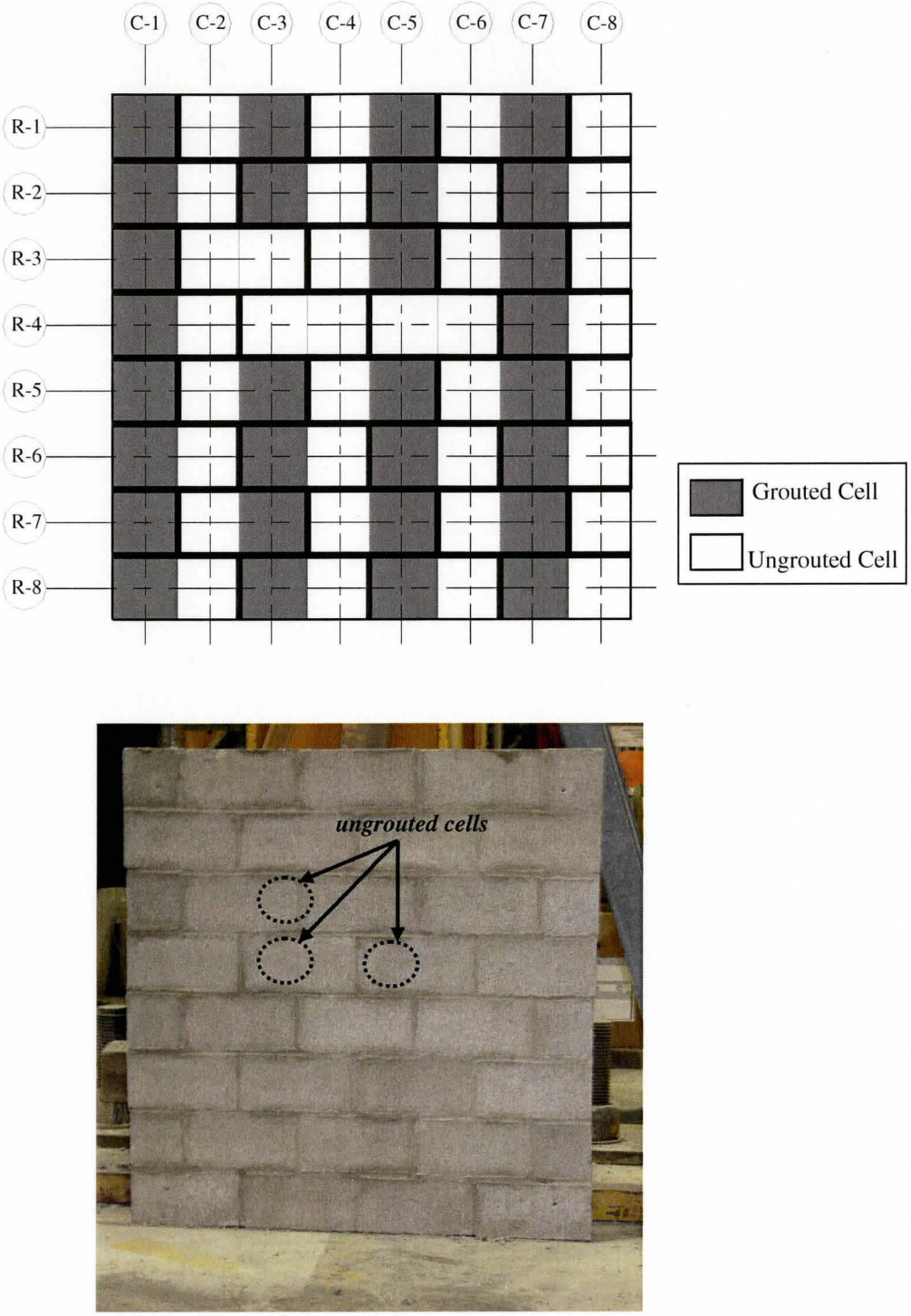

Figure 5.30: The half scale wall containing grouted and ungrouted cells

5.8.3 FEM of Concrete Masonry Block

Figure 5.31 shows a sample output of the FEM with the electric field distribution and equipotential lines for a coplanar sensor over a grouted cell of a masonry block. Figure 5.32-(a) shows the capacitance variations obtained from the finite element simulations along the side of a masonry block containing grouted and ungrouted cells. The actual positions of the cells and web are superimposed on the figure to facilitate interpretation of the results. There is a significant difference between the capacitance values obtained in the centre of the grouted and ungrouted cells. A linear variation of the capacitance values exists in the web region of the masonry block. Similar FEM simulations were performed along the side of a masonry block having two unfilled cells, Figure 5.32-(b). Since there is no grout in either cell, the capacitance is nearly symmetrical about the web. The capacitance has a higher value in the web region.

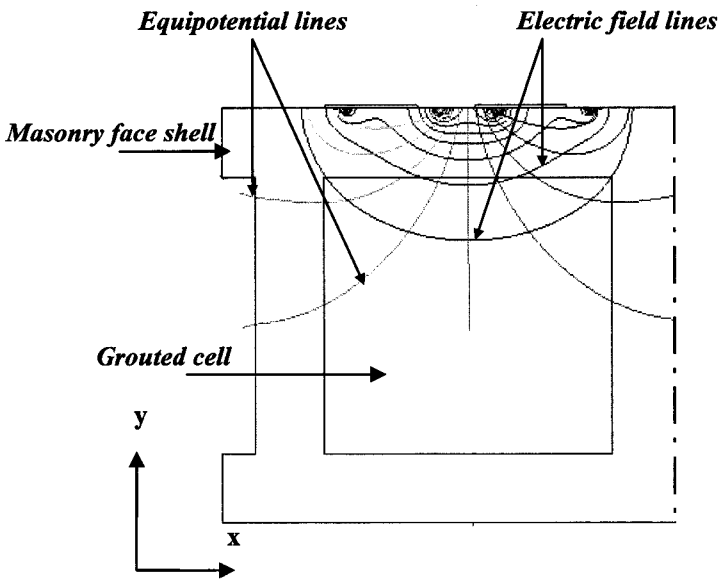

Figure 5.31: The electric field and equipotential lines obtained from FEM for a grouted cell

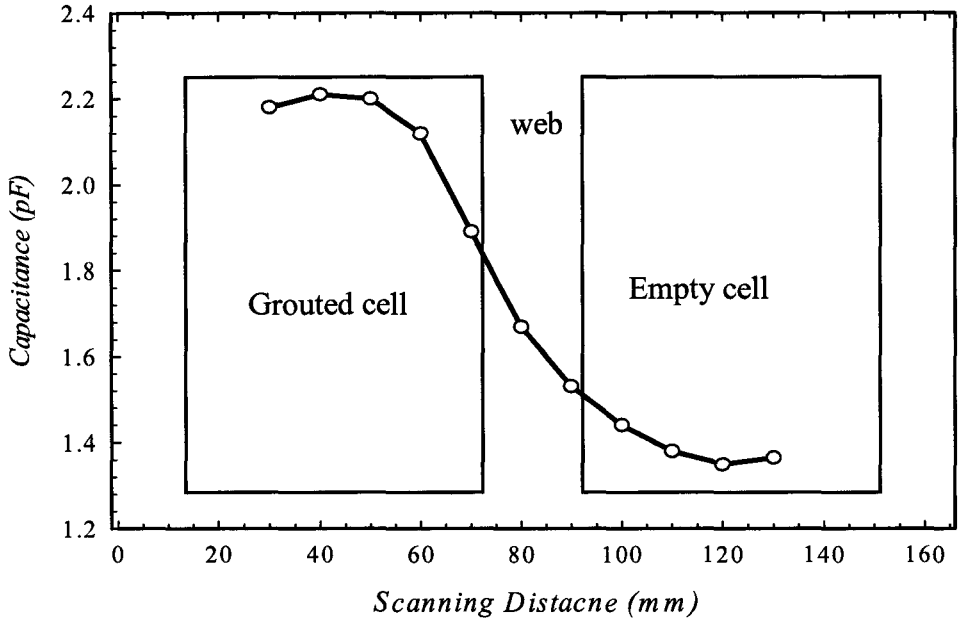

(a)

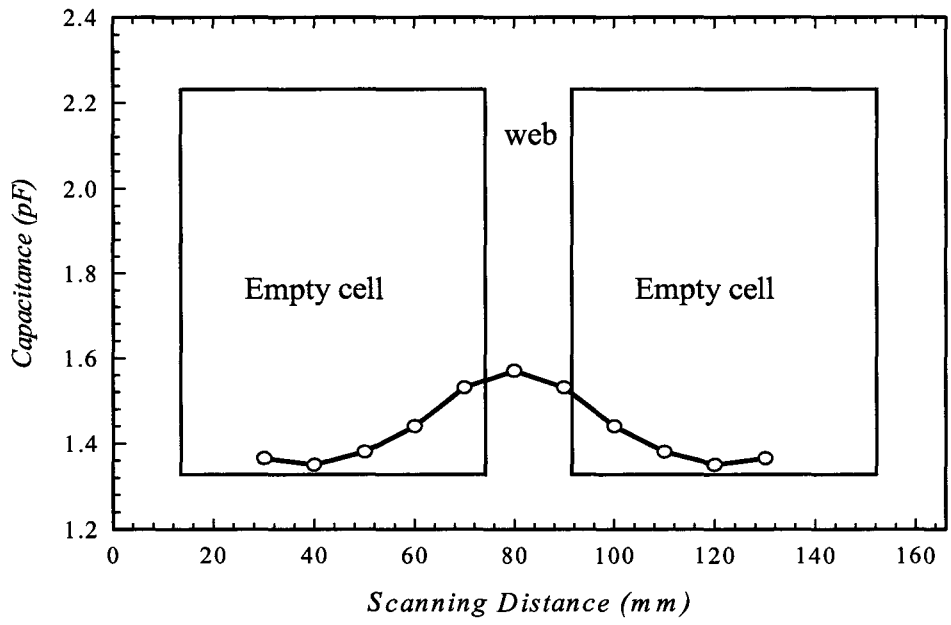

(b)

Figure 5.32: Magnitude of the capacitance values obtained from FEM a long the side of masonry blocks, (a) a block containing an empty and grouted cell, (b) a block containing two empty cells

5.8.4 Test Results

Figure 5.33 shows the capacitance measurements for different cells of the inspected wall. The measured capacitances were affected by the presence of voids and unfilled cells as the capacitance decreased in these defected regions. The decrease of the output signals is attributed to the low value of the dielectric permittivity of air, $\varepsilon_{air} = 1.0$, compared to that of the grout, $\varepsilon_{grout} = 5.14$. Sensor, *S1* [Figure 5.33-(a)] gave more stable and robust results over *S2* and *S3* [both are shown in Figure 5.33-(b) and Figure 5.33-(c) respectively]. The mean values for the measurements of grouted and ungrouted cells were *2.61 pF* and *1.52 pF* respectively with average coefficient of variation (*COV*) for both grouted and ungrouted cells of *2.56 %*, while the mean values of *S2* measurements were *2.21 pF* and *1.38 pF* for grouted and ungrouted cells with *COV* of *4.03%*. Sensor *S3* had the lowest signals with grouted and ungrouted measurement of *2.03 pF* and *1.28 pF* with *COV* of *5.53%*. The results obtained from each sensor were also listed in Table 5.3, 5.4, and 5.5 for *S1*, *S2*, and *S3* respectively. The capacitance profiles from the measurements were extrapolated from the measured capacitance obtained from the three sensor configurations and presented in Figure 5.34. The voids and ungrouted zones can be identified by the dark regions while the grouted cells appear as light regions. These regions can be clearly recognized for the profile obtained from *S1* measurements, as shown in Figure 5.34-(a). Although the *COV* of the measurements are high, good differentiations still exist between the ungrouted and grouted regions of measurements obtained from *S2* and *S3* as shown in Figure 5.34-(b) and Figure 5.34-(c) respectively.

The analytical and FEM simulations results were also obtained to verify the experimental results. Comparison between the results obtained from the experimental data, analytical model, and FEM simulations is shown in Figure 5.35. The theoretical results over-predicted the experimental values by *10 %* on average.

Sensor sensitivity was used to compare between different sensor configurations. Sensor sensitivity is an indication of how much sensor signals change for ungrouted cells compared with grouted cells. The sensor sensitivity is defined as:

$$\%\ Sensor\ Sensitivity = \frac{C_{grouted} - C_{ungrouted}}{C_{grouted}} \times 100 \tag{5.4}$$

where $C_{grouted}, C_{ungrouted}$ are the average capacitance measurements for grouted and ungrouted cells. The sensitivity of *S1* (*42.27%*) was found to be higher than that of *S2* (*37.45%*) and *S3* (*36.72%*).

The Signal-to-Noise Ratio (*SNR)* is another factor that was used to compare between the three sensors. The *SNR* can be estimated as follows, (Meola 2007):

$$SNR = \frac{C_{grouted} - C_{ungrouted}}{\sigma_g} \tag{5.5}$$

where σ_g is the standard deviation of sensor measurements for the grouted cells. The *SNR* was higher for *S1* (*21.73*) than that of *S2* (*10.89*) and *S3* (*8.91*).

Table 5.6 shows a comparison between the three sensors with respect to *COV*, *SNR* and sensor sensitivity. The results show that the sensor with narrowest gap, *S1*, is

more sensitive for ungrouted locations and less affected by noise and produces less variation of the measured readings.

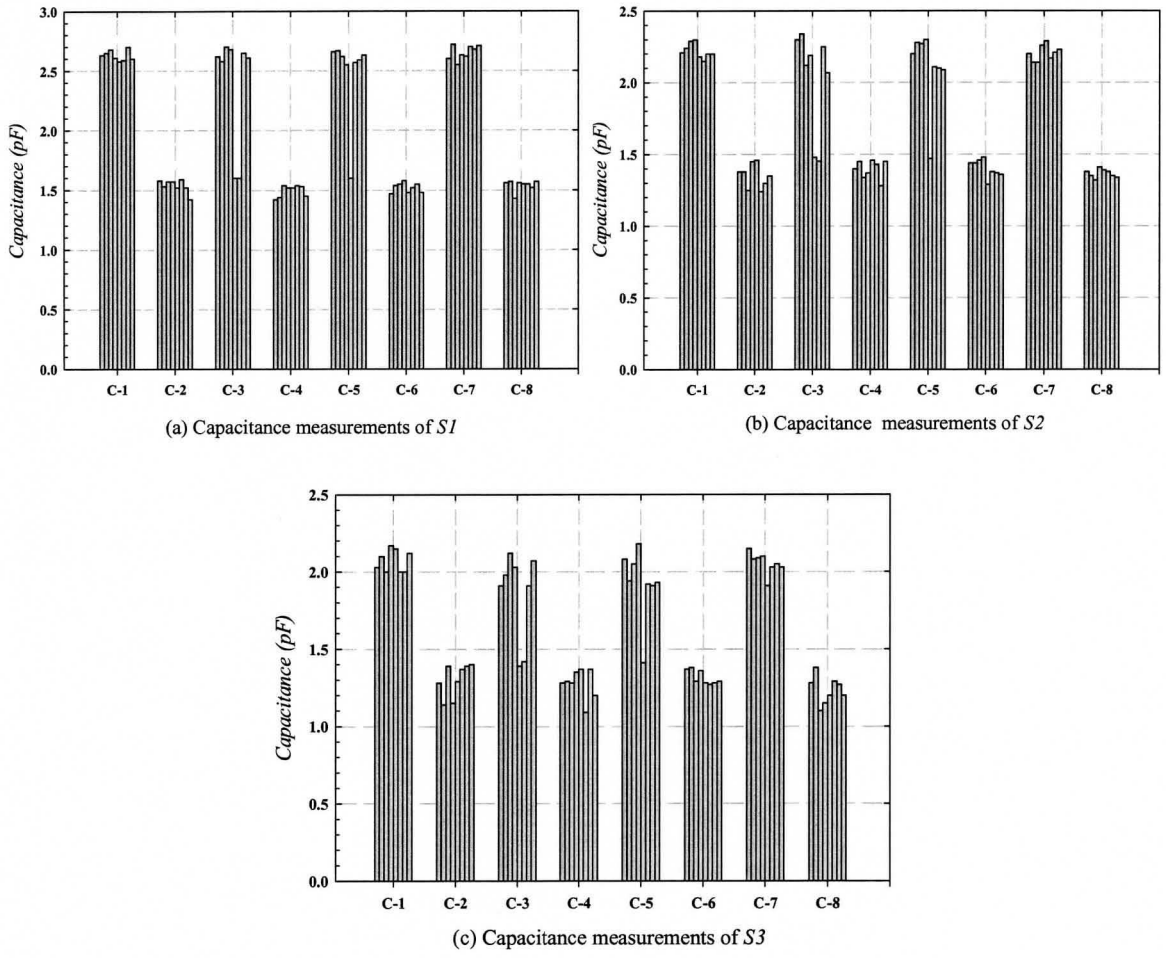

Figure 5.33: Capacitance measurements for columns of tested wall, (a) measurements of *S1*, (b) measurements of *S2* and (c) measurements of *S3*

Table 5.3: The capacitance measurements in (*pF*) for different wall cells obtained from *S1*

	Columns							
Rows	C-1	C-2	C-3	C-4	C-5	C-6	C-7	C-8
R-1	2.63	**1.58**	2.60	**1.42**	2.66	**1.47**	2.62	**1.56**
R-2	2.65	**1.53**	2.72	**1.44**	2.67	**1.54**	2.58	**1.57**
R-3	2.68	**1.57**	**1.60**	**1.54**	2.62	**1.55**	2.70	**1.43**
R-4	2.61	**1.57**	**1.60**	**1.52**	**1.61**	**1.58**	2.68	**1.56**
R-5	2.58	**1.52**	2.55	**1.52**	2.59	**1.48**	2.69	**1.55**
R-6	2.59	**1.59**	2.75	**1.54**	2.57	**1.52**	2.63	**1.55**
R-7	2.70	**1.52**	2.68	**1.53**	2.59	**1.55**	2.65	**1.52**
R-8	2.60	**1.42**	2.71	**1.45**	2.63	**1.48**	2.61	**1.57**

Note: Numbers in bold and represent the measurements obtained from ungrouted cells

Table 5.4: The capacitance measurements in (*pF*) for different wall cells obtained from *S2*

	Columns							
Rows	C-1	C-2	C-3	C-4	C-5	C-6	C-7	C-8
R-1	2.21	**1.38**	2.30	**1.40**	2.20	**1.44**	2.20	**1.38**
R-2	2.24	**1.38**	2.34	**1.45**	2.28	**1.44**	2.14	**1.35**
R-3	2.29	**1.25**	**1.48**	**1.34**	2.27	**1.46**	2.14	**1.32**
R-4	2.30	**1.45**	**1.45**	**1.37**	**1.47**	**1.48**	2.26	**1.41**
R-5	2.18	**1.46**	2.06	**1.46**	2.29	**1.29**	2.29	**1.39**
R-6	2.15	**1.24**	2.30	**1.43**	2.11	**1.38**	2.17	**1.38**
R-7	2.20	**1.30**	2.25	**1.28**	2.10	**1.37**	2.21	**1.35**
R-8	2.20	**1.35**	2.07	**1.45**	2.09	**1.36**	2.23	**1.34**

Note: Numbers in bold represent the measurements obtained from ungrouted cells

Table 5.5: The capacitance measurements in (*pF*) for different wall cells obtained from *S3*

	Columns							
Rows	C-1	C-2	C-3	C-4	C-5	C-6	C-7	C-8
R-1	2.03	**1.28**	1.91	**1.28**	2.08	**1.37**	2.15	**1.28**
R-2	2.10	**1.14**	1.98	**1.29**	1.94	**1.38**	2.08	**1.38**
R-3	2.00	**1.39**	**1.39**	**1.28**	2.05	**1.29**	2.09	**1.10**
R-4	2.17	**1.15**	**1.42**	**1.35**	**1.41**	**1.36**	2.10	**1.15**
R-5	2.15	**1.29**	2.02	**1.37**	1.90	**1.28**	1.91	**1.20**
R-6	2.00	**1.37**	2.01	**1.09**	1.92	**1.27**	2.03	**1.29**
R-7	2.00	**1.39**	1.91	**1.37**	1.91	**1.28**	2.05	**1.27**
R-8	2.12	**1.40**	2.07	**1.20**	1.93	**1.29**	2.03	**1.20**

Note: Numbers in bold represent the measurements obtained from ungrouted cells

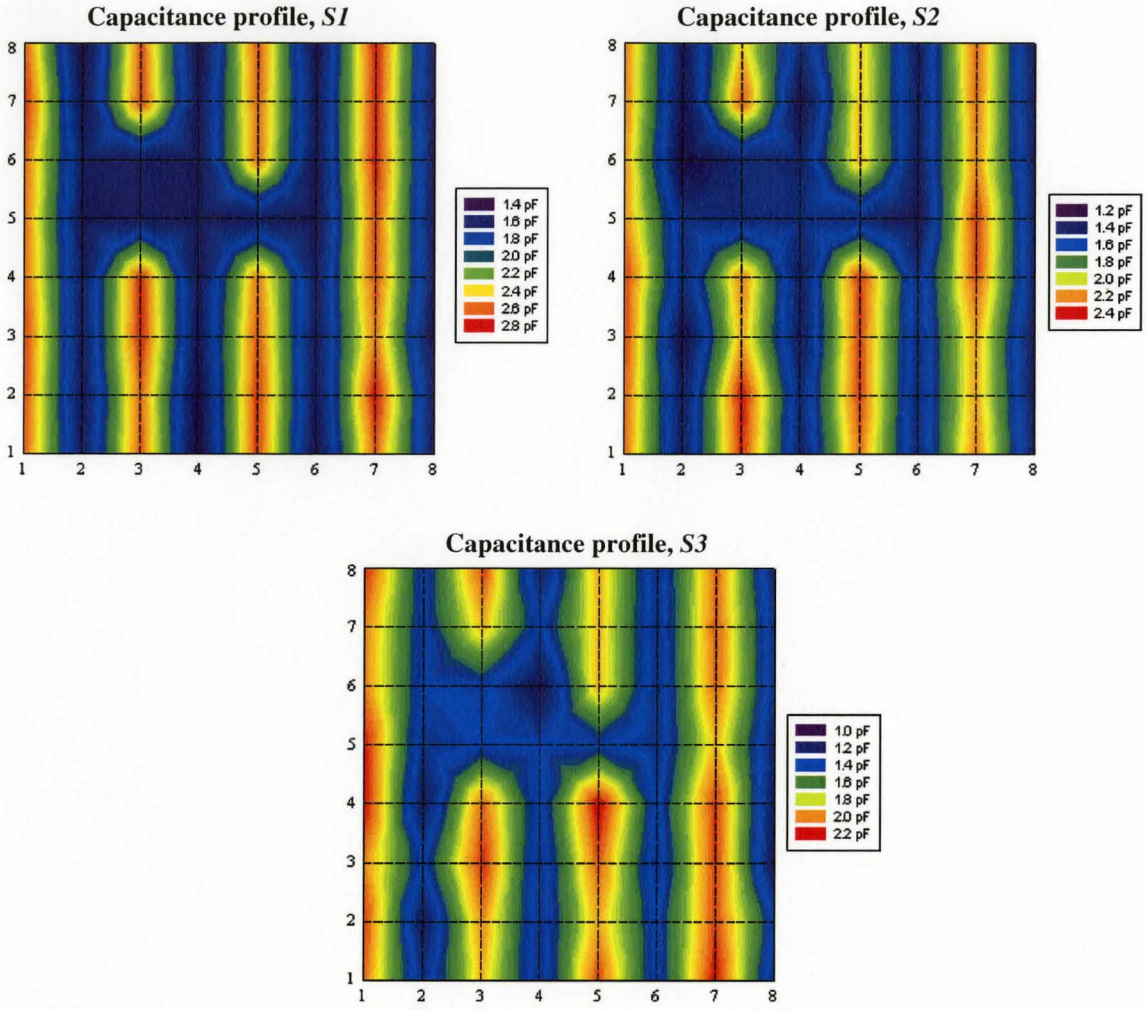

Figure 5.34: Capacitance profile for the inspected wall obtained from different CCS

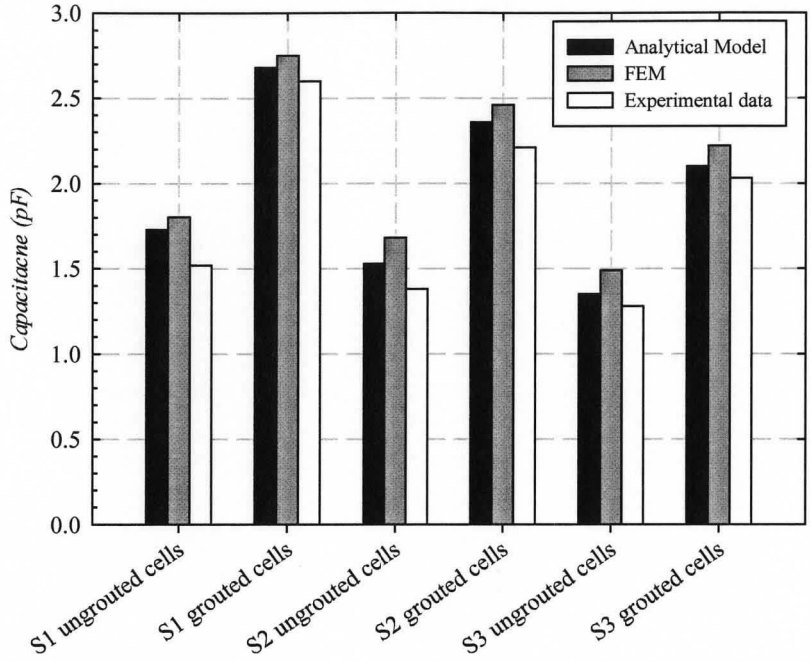

Figure 5.35: Comparison between the experimental, analytical, and FEM results

Table 5.6: Comparison between the three different sensor configurations

Sensor	*% COV*	*SNR*	*% Sensitivity*
S1 (25 × 8)	*2.56%*	*21.73*	*42.27%*
S2 (20 × 10)	*4.03%*	*10.89*	*37.45%*
S3 (15 × 12)	*5.53%*	*8.92*	*36.72%*

5.9 Conclusions

The experimental results obtained from different capacitance sensors to detect damages in different specimens were presented. Three composite specimens containing pre-induced defects were constructed and inspected. The composite specimens were as following: (1) Concrete specimens strengthened with GFRP contained a series of pre-induced defects to simulate air voids, water intrusions, and glue infiltrations, (2) Wood column wrapped with FRP contained pre-induced defects to represent air voids and decay simulating defects, and (3) FRP pultruded members contained pre-fabricated defects that simulated delaminations and water intrusions in these members. The principles behind the sensor operation were also applied to locate ungrouted cells and poorly grouted zones in a concrete masonry wall. Different capacitance sensors including CCS and IDCS were fabricated and used to detect the defects, and their performances were compared with respect to their measurement variations and sensitivities.

The dielectric permittivities of various materials involved in the composite specimens and the constructed wall were experimentally evaluated. FEM simulations were performed to predict the sensor responses for different type of defects using the evaluated dielectric permittivities. Good agreements were found between the measured capacitance and those predicted by FEM with errors attributed to fringing end effects, and stray capacitance.

The test results of GFRP/concrete specimen showed that *CCS1* had the highest measurement variation and sensitivity for water intrusion defects as the sensitivity varied between *52-107%* for water intrusion heights between *2.0 -10.0 mm*. *IDCS1* had the

highest sensor sensitivity for air-filled (*32-45%*) and epoxy-filled defects (*12-18%*) for defect heights ranging between *2.0-10.0 mm*.

For GFRP/wood specimen, *IDCS1* gave higher sensor sensitivity than the two other sensors, *CCS1* and *IDCS2*, as the sensitivity was ranging between (*16-26%*) for defect heights between *2.0-10 mm*. *CCS1* gave as high sensitivity as *65-160%* for decay simulating defects heights between *2.0-10.0 mm*.

For GFRP pultruded members, *CCS1* were capable of detecting a delamination, of width of *55 mm*, and an average height of *1.2 mm* at a depth of *3 mm* from the upper surface of the flange, with a mean variation in capacitance reading of *12.5%*. In addition, *CCS1* had the highest sensitivity for detecting delaminations and water intrusions in GFRP plate with a maximum sensitivity of *14%* and *96%* for delamination and water intrusion respectively for defect depth of $z = 2$ *mm*.

By comparing the performances of the three CCS with same penetration depth, it was found that the CCS was capable of identifying the ungrouted cells in concrete masonry walls. In addition, the sensor with narrowest gap spacing and widest electrode width proved to be more sensitive and less affected by noise with sensor sensitivity reached to *42%* to detect such construction defects.

Chapter 6: Summary, Conclusions, and Future Recommendations

6.1 Summary

This thesis focused on damage detection in composite structures using the capacitance measurements of materials with different dielectric signatures. The scope of this work involved capacitance sensor design, experiments, and data analysis. The electrostatic principles behind the development of the coplanar sensors were highlighted. The effect of dielectric material properties on the resulting capacitance and the electric field generated between the capacitor plates was discussed. This was followed by presenting an analytical model to predict the capacitance output of the proposed CCS and IDCS over a layered media. The analytical model was based on the conformal mapping transformation that allows transforming the field of the planar structures into the electric field of the parallel-plate capacitor.

A *2D* FEM was also presented using FEM package, *Ansoft Maxwell 2D*. FEM code estimated the expected response of the sensor given all information about the material under test and the sensor parameters. FEM code was used to calculate the capacitance and to plot the electric field distribution across the sensor electrodes. The proper modelling using FEM code included several steps such as building the geometrical

model, assigning the materials, defining the boundary conditions, choosing the model mesh, and solving the FEM.

The analytical modelling and FEM were used to study the effect of the sensor geometry parameters on the output signal and to optimize the sensor designs. The influence of the electrode width and electrode spacing on the signal strength and the penetration depth of the electric field through the material layers were evaluated. The sensor design charts were developed to facilitate the selection of these parameters in order to obtain on the optimal designs of the capacitance sensors.

The effect of the defects on the sensor responses was theoretically presented by changing the defect depth, height and type. In addition, the determination of the defect location was demonstrated using a set of coplanar sensors with equal (s/g) ratio.

The capacitance sensor capabilities were examined with different type of defects in three composite specimens: (1) Concrete slabs strengthened with GFRP contained a series of pre-induced defects to simulate air voids, water intrusions, and glue infiltrations, (2) Wood column wrapped with FRP contained pre-induced defects to represent air voids and decay simulating defects, and (3) FRP pultruded members contained pre-fabricated defects that simulated delaminations and water intrusions in these members. The principles behind the sensor operation were also applied to locate ungrouted cells and poorly grouted zones in a concrete masonry wall.

Different capacitance sensors including CCS and IDCS were fabricated and used to detect the defects, and their performances were compared with respect their measurements variations and sensitivities.

6.2 Conclusions

A rapid cost-effective technique for the detection of damages/defects that may occur in composite structures was developed in this thesis. The proposed technique was based on detecting the local dielectric permittivity variations in composite materials using capacitance sensors. The sensor geometry has the largest influence on signal strength, and sensor penetration depth. It was found that the increase of gap spacing between the electrodes increased the penetration depth of the electric field through the material layers but reduced the signal strength, while the increase of the electrode width increased both the penetration depth and signal strength. The optimal design, therefore, is achieved by the proper selection of the sensor geometrical dimensions in order to get a sufficient field penetration depth with the highest signal strength. This, in turn, depends on the specific application and desired detection depth.

The experimental results on the composite specimens that contained pre-induced defects showed that the composite defects could be detected and identified if they lie within the penetration depth of the sensor and if it is sufficiently different in its dielectric nature from the legitimate composite materials.

The test results of GFRP/concrete specimen showed that *CCS1* had the highest measurement variations and sensitivity for water intrusion defects as the sensitivity varied between *52-107%* for water intrusion heights between *2-10 mm*. *IDCS1* had the highest sensor sensitivity for air-filled (*32-45%*) and epoxy-filled defects (*12-18%*) for defect heights ranging between *2-10 mm*.

For GFRP/wood specimen, *IDCS1* gave higher sensor sensitivity than the two other sensors, *CCS1* and *IDCS2*, as the sensitivity was ranging between (*16-26%*) for defect heights between *2.0-10 mm*. *CCS1* gave as high sensitivity as *65-160%* for decay simulating defects heights between *2-10 mm*.

For GFRP pultruded members, *CCS1* were capable of detecting a delamination, of width of *55 mm*, and an average height of *1.2 mm* at a depth of *3 mm* from the upper surface of the I-beam flange, with a mean variation in capacitance reading of *12.5%*. In addition, *CCS1* had the highest sensitivity for detecting delaminations and water intrusions in GFRP plate with a maximum sensitivity of *14%* and *96%* for delamination and water intrusion respectively for defect depth of $z = 2$ *mm*.

By comparing the performances of the three CCS with same penetration depth, it was found that the CCS was capable of identifying the ungrouted cells in concrete masonry walls. In addition, the sensor with narrowest gap spacing and widest electrode width proved to be more sensitive and less affected by noise with sensor sensitivity reached to *42%* to detect such construction defects.

Good agreements were found between the measured capacitance and those predicted by FEM with errors attributed to fringing end effects, and stray capacitance.

.

6.3 Directions and Suggestions for Future Research

In this thesis, the feasibility of a technique for damage detection in composite using capacitance sensors has been established through theoretical and experimental investigations. However, additional theoretical and experimental work is still required to

quantify the sensitivity of this technique to detect the defects/damages of other composite materials, which have different material's properties such as carbon fibre reinforced polymer (CFRP) and steel members wrapped with fibre composites. Dealing with these materials should take into account the conductivity coefficients. Therefore, other measured parameters could be useful in the inspection rather than the electric capacitance such as the electric conductivity and the impedance of the inspected materials.

Some mechanical parts could improve the sensing system such as an adjustable sensor, which enables the control of the electrode width and electrode spacing. Such sensor would be very beneficial for determining the defect location, and for its different applications in the field.

Moreover, the development of a portable scanner system in which the capacitance sensor is coupled with the capacitance meter would facilitate the implementation of the capacitance technique and provide hand-held scanning system for the nondestructive inspection of composite materials in the field.

The capacitance sensor technique could be used to develop structural health monitoring (SHM) systems that can accurately monitor large-scale civil infrastructures such as bridges, vital pipeline, aircraft, and sensitive storage tanks. Structural health monitoring (SHM) has been introduced as a global approach of damage detection for these structures. SHM may defined as measurement of the operating and loading environment and the critical response of a structure to track and evaluate the symptoms of operational incidents, deterioration or damage indicators that may impact structure's

serviceability and safety. Such system may include sensor network systems. The design of such systems includes the optimization of sensor numbers, and location.

Bibliography

Adams, R. D., Walton, D., Flitcroft, J. E., and Short, D. (1975). "Vibration testing as a nondestructive test tool for composite materials." *Composite Reliability, ASTM STP*, 580, 159–175.

Ahmed, H. (2006). "Capacitance sensors for void-fraction measurements and flow-pattern identification in air-oil two-phase flow." *Sensors Journal, IEEE*, 6(5), 1153-1163.

Alampalli, S. (2006). "Field performance of an FRP slab bridge." *Composite Structures*, 72(4), 494-502.

Aymerich, F., and Meili, S. (2000). "Ultrasonic evaluation of matrix damage in impacted composite laminates." *Composites Part B: Engineering*, 31(1), 1-6.

Bogetti, T. A., Gillespie, J. W. J. R., and Lamontia, M. A. (1992). "Influence of ply waviness on the stiffness and strength reduction on composite laminates." *Journal of Thermoplastic Composite Materials*, 5(4), 344-369.

Bord, I., Tardy, P., and Menil, F. (2006). "Influence of the electrodes configuration on a differential capacitive rain sensor performances." *Sensors and Actuators B: Chemical*, 114(2), 640-645.

Caiazzo, A., Orlet, M., McShane, H., Strait, L., and Rachau, C. (1999). "The effects of marcel defects on composite structural properties." *Composite structures- Theory and practice*, 158-187.

Cantwell, W., and Morton, J. (1992). "The significance of damage and defects and their detection in composite materials: A review." *The Journal of Strain Analysis for Engineering Design*, 27(1), 29-42.

Carlsson, E., and Gevorgian, S. (1999). "Conformal mapping of the field and charge distributions in multilayered substrate CPWs." *IEEE Transactions on Microwave Theory and Techniques*, 47(8), 1544-1552.

Cawley, P., and Adams, R. D. (1979). "A vibration technique for non-destructive testing of fibre composite structures." *Journal of Composite Materials*, 13(2), 161-175.

CMDC (2007) Canada Masonry Design Centre, Personal communication with Mr. D. Stubbs, Technical Advisor, CMDC, Mississauga, Ontario, Canada May, 2007.

Chang, F. H., Couchman, J. C., Eisenmann, J. R., and Yee, B. G. W. (1975). "Application of a special X-ray nondestructive testing technique for monitoring damage zone growth in composite laminates." *ASTM special technical publication*, 176-190.

Dattoma, V., Marcuccio, R., Pappalettere, C., and Smith, G. M. (2001). "Thermographic investigation of sandwich structure made of composite material." *NDT & E International*, 34(8), 515-520.

Dempsey, D. D., and Scott, D. W. (2006). "Wood members strengthened with mechanically fastened FRP strips." *Journal of Composites for Construction*, 10(5), 392-398.

Dunn, W. L., and Yacout, A. M. (2000). "Corrosion detection in aircraft by X-ray backscatter methods." *Applied Radiation and Isotopes*, 53(4-5), 625-632.

El-Dakhakhni, W. W., Hamid, A. A., and Elgaaly, M. (2004). "Seismic retrofit of concrete masonry infilled steel frames with glass fiber-reinforced polymer laminates." *Journal of Structural Engineering*, 130(9), 1343-1352.

Elkow, K. J., and Rezkallah, K. S. (1996). "Void fraction measurements in gas-liquid flows using capacitance sensors." *Measurement Science and Technology*, 7(8), 1153-1163.

Gentile, C., Svecova, D., and Rizkalla, S. H. (2002). "Timber Beams Strengthened with GFRP Bars: Development and Applications." *Journal of Composites for Construction*, 6(1), 11-20.

Gevorgian, S., and Berg, H. "Line capacitance and impedance of coplanar-strip waveguides on substrates with multiple dielectric layers." *Proceedings of European Microwave Conference*, London, UK, 153-156.

Gower, M. R. L., and Sims, G. D. (2004). "Characterisation of defects in composite material systems." *Project MMS13 Task 4 - Report 1, NPL Report MATC(A)158, January 2004*

Halabe, U. B., Bangalore, G., GangaRao, H. V. S., and Klinkhachorn, P. (2002). "Infrared scanning of FRP composite members." Review of progress in quantitative nondestructive evaluation: Volume 22, AIP, Bellingham, Washington (USA), 1003-1010.

Hayt, W. H., and Buck, J. A. (2001). *Engineering Electromagnetics*, McGraw-Hill, Boston.

Hillger, W., Ahrholdt, M., Rohling, H., and Henrich, R. (2004). "Non-contact ultrasonic imging techniques for composite components." 16th World Conference on Nondestructive Testing, Montreal, Canada.

Imielinska, K., Castaings, M., Wojtyra, R., Haras, J., Clezio, E. L., and Hosten, B. (2004). "Air-coupled ultrasonic C-scan technique in impact response testing of carbon fibre and hybrid: glass, carbon and Kevlar/epoxy composites." *Journal of Materials Processing Technology*, 157-158, 513-522.

Jama, H. A., Hussein, E. M. A., and Lee-Sullivan, P. (1998). "Detection of debonding in composite-aluminum joints using gamma-ray Compton scattering." *NDT & E International*, 31(2), 99-103.

Jaworski, A. J., Dyakowski, T., and Davies, G. A. (1999). "A capacitance probe for interface detection in oil and gas extraction plant." *Meas. Sci. Technol.* , 10(3), L15-L20.

Kang, K., Choi, M., Kim, K., Cha, Y., Kang, Y., Hong, D., and Yang, S. (2006). "Inspection of impact damage in honeycomb composite plate by ESPI, ultrasonic, testing, and thermography." 12th A-PCNDT 2006 – Asia-Pacific Conference on NDT, Nov. 5 -10 , Auckland, New Zealand.

Kessler, S. S., Spearing, S. M., Atalla, M. J., Cesnik, C. E. S., and Soutis, C. (2002). "Damage detection in composite materials using frequency response methods." *Composites Part B: Engineering*, 33(1), 87-95.

Khan, M. M. U. (1999). "Non-destructive testing applications in commercial aircraft maintenance." *Journal of Nondestructive Testing & Ultrasonics (Germany)*, 4(6).

Krishnapillai, M., Jones, R., Marshall, I. H., Bannister, M., and Rajic, N. (2005). "Thermography as a tool for damage assessment." *Composite Structures*, 67(2), 149-155.

Kurtz, S., Balaguru, P., and Helm, J. (2008). "Experimental study of interfacial shear stresses in FRP-strengthened RC beams." *Journal of Composites for Construction*, 12(3), 312-322.

Lane, S. S., Moore, R. H., Groger, H. P., Gandhe, G. V., and Griffin, O. H. (1991). "Eddy current inspection of graphite/epoxy laminates." *Journal of Reinforced Plastics and Composites*, 10(2), 158-166.

Lee, B. T., Sun, C. T., and Liu, D. (1987). "An assessment of damping measurement in the evaluation of integrity of composite beams." *Journal of Reinforced Plastics and Composites*, 6(2), 114-125.

Levar, J. M., and Hamilton, H. R. T. (2003). "Nondestructive evaluation of carbon fiber-reinforced polymer-concrete bond using infrared thermography." *ACI Materials Journal*, 100(1), 63-72.

Li, X. (2003). "Impedance spectroscopy for manufacturing control of material physical properties," Master's Thesis, University of Washington.

Li, X., Lei, T., Wang, W., Xu, Q., and Zhao, J. (2005). "Capacitance sensors for measuring suspended sediment concentration." *CATENA*, 60(3), 227-237.

Li, X., Zyuzin, A. S., and Mamishev, A. V. "Measuring moisture content in cookies using dielectric spectroscopy." *Annual Report. Conference on Electrical Insulation and Dielectric Phenomena, 2003.*, 459-462.

Li, X. B., Larson, S. D., Zyuzin, A. S., and Mamishev, A. V. "Design of multichannel fringing electric field sensors for imaging. Part I. General design principles." *IEEE International Symposium on Electrical Insulation, 2004*, 406-409.

Lowe, D. C., and Rezkallah, K. S. (1999). "Flow regime identification in microgravity two-phase flows using void fraction signals." *International Journal of Multiphase Flow*, 25(3), 433-457.

Mamishev, A. V., Sundara-Rajan, K., Fumin, Y., Yanqing, D., and Zahn, M. (2004). "Interdigital sensors and transducers." *Proceedings of the IEEE*, 92(5), 808-845.

Maxwell 2D. (2003). Ansoft Corporation , Pittsburgh, PA.

Maxwell 2D simulator manual (2003). Ansoft Corporation , Pittsburgh, PA.

Meng, G., Jaworski, A. J., and Kimber, J. C. S. (2006). "A multi-electrode capacitance probe for phase detection in oil–water separation processes: design, modelling and validation." *Meas. Sci. Technol.*, 17, 881–94.

Meola, C. (2007). "Infrared thermography of masonry structures." *Infrared Physics & Technology*, 49(3), 228-233.

Mix, P. E. (1987). *Introduction to nondestructive testing : a training guide*, Wiley, New York.

Mook, G., Lange, R., and Koeser, O. (2001). "Non-destructive characterisation of carbon-fibre-reinforced plastics by means of eddy-currents." *Composites Science and Technology*, 61(6), 865-873.

Mouritz, A. P., Townsend, C., and Shah Khan, M. Z. (2000). "Non-destructive detection of fatigue damage in thick composites by pulse-echo ultrasonics." *Composites Science and Technology*, 60(1), 23-32.

Ozgu, M. R., Chen, J. C., and Eberhardt, N. (1973). "A capacitance method for measurement of film thickness in two-phase flow." *Review of Scientific Instruments*, 44(12), 1714-1716.

Paolozzi, A., and Peroni, I. (1990). "Detection of debonding damage in a composite plate through natural frequency variations." *Journal of Reinforced Plastics and Composites*, 9(4), 369-389.

Parlapalli, M., and Shu, D. (2004). "Buckling analysis of two-layer beams with an asymmetric delamination." *Engineering Structures*, 26(5), 651-658.

Sadler, D. J., and Ahn, C. H. (2001). "On-chip eddy current sensor for proximity sensing and crack detection." *Sensors and Actuators A: Physical*, 91(3), 340-345.

Schinzinger, R., and Laura, P. (1991). *Conformal mapping: methods and applications*, Elsevier, New York, NY, U.S.A.

Shedid, M., Hamid, A., and Drysdale, R. (2005). "Ductility of reinforced masonry shear walls and impact of incomplete grouting." 10th Canadian Masonry Symposium, University of Calgary, Banff, Alberta, Canada.

Shen, M. H. H., and Grady, J. E. (1991). "Free vibrations of delaminated beams." *AIAA Journal*, 30(5), 1361-1370.

Starnes, M. A., Carino, N. J., and Kausel, E. A. (2003). "Preliminary thermography studies for quality control of concrete structures strengthened with fiber-reinforced polymer composites." *Journal of Materials in Civil Engineering*, 15(3), 266-273.

Strizzolo, C. N., and Converti, J. (1993). "Capacitance sensors for measurement of phase volume fraction in two-phase pipelines." *Instrumentation and Measurement, IEEE Transactions on*, 42(3), 726-729.

Sundara-Rajan, K., Byrd, L., II, and Mamishev, A. V. (2004). "Moisture content estimation in paper pulp using fringing field impedance spectroscopy." *Sensors Journal, IEEE*, 4(3), 378-383.

Tenek, L. H., Henneke, E. G., and Gunzburger, M. D. (1993). "Vibration of delaminated composite plates and some applications to non-destructive testing." *Composite Structures*, 23(3), 253-262.

Thong-un, N., Sriratana, W., and Tanachaikhan, L. "Design of capacitive sensor for concentration measurement." *SICE-ICASE International Joint Conference* Busan, South Korea, 1959-1962.

Toyama, N., Kikushima, Y., and Takatsubo, J. (2002). "Effect of delamination on Lamb wave velocity in cross-ply laminates." *Journal of Materials Science Letters*, 21(24), 1891-1893.

Tracy, J. J., and Pardoen, G. C. (1989). "Effect of delamination on the natural frequencies of composite laminates." 23(12), 1200-1215.

Tsamis, E. D., and Avaritsiotis, J. N. (2005). "Design of planar capacitive type sensor for "water content" monitoring in a production line." *Sensors and Actuators A: Physical*, 118(2), 202-211.

Ulaby, F. T. (2005). *Electromagnetics for Engineers*, Pearson/Prentice Hall, Upper Saddle River, NJ.

Vendik, O. G., Zubko, S. P., and Nikol'skii, M. A. (1999). "Modeling and calculation of the capacitance of a planar capacitor containing a ferroelectric thin film." *Technical Physics*, 44(4), 349-355.

Viitanen, H. (1994). "Factors affecting the development of biodeterioration in wooden constructions." *Materials and Structures*, 27(8), 483-493.

Wang, Y., Chong, N., Cheng, Y. L., Chan, H. L. W., and Choy, C. L. (2003). "Dependence of capacitance on electrode configuration for ferroelectric films with interdigital electrodes." *Microelectronic Engineering*, 66(1-4), 880-886.

Zak, A., Krawczuk, M., and Ostachowicz, W. (2001). "Vibration of a laminated composite plate with closing delamination." *Journal of Intelligent Material Systems and Structures*, 12(8), 545-551.

Zhao, X.-L., and Zhang, L. (2007). "State-of-the-art review on FRP strengthened steel structures." *Engineering Structures*, 29(8), 1808-1823.

Zhou, G. G., Kowel, S. T., and Srinivasan, M. P. (1988). "A capacitance sensor for on-line monitoring of ultrathin polymeric film growth." *IEEE Transactions on Components, Hybrids, and Manufacturing Technology* 11(2), 184-190.

Zou, Y., Tong, L., and Steven, G. P. (2000). "Vibration-based model-dependent damage (delamination) identification and health monitoring for composite structures - a review " *Journal of Sound and Vibration*, 230(2), 357-378.